SURFACE CHARGE FEATURES OF KAOLINITE PARTICLES AND THEIR INTERACTIONS

by

Vishal Gupta

A dissertation submitted to the faculty of
The University of Utah
in partial fulfillment of the requirements for the degree of

Doctor of Philosophy

Department of Metallurgical Engineering

The University of Utah

May 2011

The University of Utah Graduate School

STATEMENT OF DISSERTATION APPROVAL

The dissertation of **Vishal Gupta**

has been approved by the following supervisory committee members:

Jan D. Miller	, Chair	**11/23/2010** Date Approved
Vladimir Hlady	, Member	**11/23/2010** Date Approved
Sivaraman Guruswamy	, Member	**11/23/2010** Date Approved
Michael L. Free	, Member	**11/23/2010** Date Approved
Xuming Wang	, Member	**11/23/2010** Date Approved

and by **Jan D. Miller** , Chair of

the Department of **Metallurgical Engineering**

and by Charles A. Wight, Dean of The Graduate School.

ABSTRACT

Kaolinite is both a blessing and a curse. As an important industrial mineral commodity, kaolinite clays are extensively used in the paper, ceramic, paint, plastic and rubber industries. In all these applications the wettability, aggregation, dispersion, flotation and thickening of kaolinite particles are affected by its crystal structure and surface properties. It is therefore the objective of this research to investigate selected physical and surface chemical properties of kaolinite, specifically the surface charge of kaolinite particles.

A pool of advanced analytical techniques such as XRD, XRF, SEM, AFM, FTIR and ISS were utilized to investigate the morphological and surface chemistry features of kaolinite. Surface force measurements revealed that the silica tetrahedral face of kaolinite is negatively charged at pH > 4, whereas the alumina octahedral face of kaolinite is positively charged at pH < 6, and negatively charged at pH > 8.

Based on electrophoresis measurements, the apparent iso-electric point for kaolinite particles was determined to be less than pH 3. In contrast, the point of zero charge was determined to be pH 4.5 by titration techniques, which corresponds to the iso-electric point of between pH 4 and 5 as determined by surface force measurements.

Results from kaolinite particle interactions indicate that the silica face–alumina face interaction is dominant for kaolinite particle aggregation at low and intermediate pH values, which explains the maximum shear yield stress at pH 5-5.5.

Lattice resolution images reveal the hexagonal lattice structure of these two face surfaces of kaolinite. Analysis of the silica face of kaolinite showed that the center of the hexagonal ring of oxygen atoms is vacant, whereas the alumina face showed that the hexagonal surface lattice ring of hydroxyls surround another hydroxyl in the center of the ring.

High resolution transmission electron microscopy investigation of kaolinite has indicated that kaolinite is indeed composed of silica/alumina bilayers with a c-spacing of 7.2 Å.

The surface charge densities of the silica face, the alumina face and the edge surface of kaolinite all influence particle interactions, and thereby affect the mechanical properties of kaolinite suspensions. The improved knowledge of kaolinite surface chemistry from this dissertation research provides a foundation for the development of improved process strategies for both the use and disposal of clay particles such as kaolinite.

To my family and my wife Priyanka

CONTENTS

LIST OF TABLES

LIST OF FIGURES

ACKNOWLEDGMENTS

I would like to express my sincere appreciation to Professor Jan D. Miller, advisor and chair of my supervisory committee, for all his help, support, guidance and encouragement during the course of this dissertation research. Professor Miller has been a great mentor with a beautiful vision for the research. I have always learned from him, enjoyed discussion with him and I salute him for his endless knowledge in mineral processing and surface chemistry. I am always touched by his beautiful quotations written on his office wall, "Fear God" and "Work Hard," to mention a few. It is my hope to mimic Professor Miller all my life, carry on his teachings and apply them in the real world.

Thanks are also extended to Dr. V. Hlady, Dr. S. Guruswamy, Dr. M. Free and Dr. X. Wang for their positive disposition to be members of the supervisory committee and their valuable advice and comments on some aspects of this work. I have especially learned a great deal in surface chemistry from Prof. Hlady's course in "Physical Nature of Surfaces."

Thanks are also extended to Dr. Anh V. Nguyen at University of Queensland, Brisbane, Australia for giving me a chance to work on different areas of surface chemistry. A great deal of work in this dissertation was completed under his guidance, and support from his research group, particularly from Drs. J. Stokes, M. Hampton and O. Ozdemir, was wonderful in completing different tasks.

Thanks are also due to Dr. S. K. Biswal, Scientist, Institute of Minerals and Materials Technology, Bhubaneswar, India for motivating me towards a Ph.D. in the area of mineral processing and surface chemistry. Without his encouragement, it would have been impossible for me to come to Utah and relish this beautiful sea of minerals surface chemistry.

I would also like to thank Dr. Jakub Nalaskowski, Dr. Shoeleh Assemi and all my colleagues and friends for their continuous support, particularly in the bad times, and for providing motivation to finish this dissertation.

Finally, I would thank the Department of Metallurgical Engineering at the University of Utah for providing me this wonderful opportunity to work with researchers all around the world. I have learned so much from them, whether about research or everyday discussions, which I will treasure for my life.

Last, but not least, the successful completion of this dissertation research would have not been possible without the major contribution of my wife for bringing good luck in my life. I would like to express my deep love and appreciation to my family for their support all these years.

CHAPTER 1

INTRODUCTION

Clays and clay minerals and their properties are important in geology, geo-technology, agriculture and the production of engineered materials. Of particular importance are kaolins. Kaolin is a rock term, a clay mineral group and also an industrial mineral commodity [1]. The kaolin group of minerals includes kaolinite, halloysite, dickite and nacrite. The most important kaolin mineral is kaolinite of which physical and chemical properties will be discussed in this research. Kaolinite is white or near white, soft, fine in particle size, platy in shape, low in surface area and chemically inert. All of these properties distinguish the kaolinite mineral as an important industrial commodity. In fact, the significance of the kaolin industry is revealed from production statistics presented in Table 1.1, which shows the continued demand for this important industrial mineral.

Kaolinite is primarily used in the paper industry where it is used both as filler and as a coating for paper sheet. Another larger user of kaolinite is the ceramic industry, particularly in whiteware, sanitaryware, insulators and refractories. Kaolinite is also calcined to produce special grades. One such grade is produced by thermal treatment of kaolinite to 650^0C (just above the dehydroxylation temperature) to produce metakaolin.

Table 1.1- World kaolin production [2]

Country	2005	2006	2007
Albania	310, 000	300, 000	300, 000
Belgium	300, 000	300, 000	300, 000
Bulgaria	200, 000	240, 000	240, 000
Czech Republic	649, 000	673, 000	682, 000
France	319, 464	300, 000	307, 253
Germany	750, 000	750, 000	750, 000
Italy	183, 804	180, 000	180, 000
Spain	463, 398	476, 327	475, 000
Turkey	615, 271	600, 000	600, 000
Ukraine	216, 600	251, 000	244, 000
United Kingdom	1, 910, 874	1, 762, 328	1, 671, 426
Egypt	415, 400	400, 000	300, 000
Mexico	877, 147	961, 800	970, 598
USA	7, 800, 000	7, 470, 000	7, 330, 000
Brazil	2, 410, 000	2, 455, 000	2, 527, 000
Australia	231, 611	182, 304	213, 905
World Total	25, 500, 000	25, 400, 000	25, 500, 000

This metakaolin product is bulky and has an excellent dielectric property being used as filler in electrical wire coatings. A second grade is produced by further heating kaolinite to about 1050^{o}C, at which point the metakaolin is reorganized to form mullite and cristobalite. These mullite needles have a very high brightness and good opacity, which makes them suitable to be used as an extender for titanium dioxide in many applications in order to reduce formulation costs, particularly in paper coating and filling, and in paints. Kaolinites are also chemically modified using ionic and/or nonionic surfactants to make them hydrophobic or organophilic. Such surface-modified kaolinites are used in paper, paint, plastics, rubber, ink and other more specialized applications. Other applications of kaolinite include use in cracking catalysts, fiberglass, cement, adhesives, pharmaceuticals, insecticides, food additives, fertilizers, plaster, filter aids, cosmetics, polishing compounds etc.

Kaolinite is also found as gangue minerals in ores treated in mineral processing plants. In this case, kaolinite creates problems in making efficient particle separations (concentration) and in sedimentation for waste disposal (tailings), for example, during the flotation separation of valuable minerals such as diaspore from gangue minerals such as kaolinite. The Al_2O_3-to-SiO_2 ratio of most diasporic bauxite deposits in China is between 5 and 8. Thus, it is desired to treat such materials in order to increase the Al_2O_3-to-SiO_2 mass ratio by physical separation such as flotation, so that the Bayer process can be applied. In this regard, reverse flotation to remove silicate ore such as kaolinite from diasporic bauxite is very important for the economic utilization of these resources [3-9].

In another situation, kaolinite poses a problem during recovery of bitumen from oil sand and sedimentation of oil sand tailing ponds. Oil sands from the Athabasca region

of northern Alberta, Canada are composed of bitumen (~12%), sand, silts, clays (mineral content ~85%) and water (3-6%). The clay component is comprised of kaolinite (50-60%) and illite (30-50%) with some montmorillonite [10, 11]. Typical bitumen recoveries range from 88 to 95% depending on oil sands grade and origin. Tailings include a mixture of water, sand, silt, clay and residual bitumen. This tailings slurry is approximately 55% solids (82% sand and 18% fines < 44 μm). Historically, the tailings were pumped into large settling basins where the sand fraction settled out rapidly to form beaches. Some fines were trapped within the sand matrix of the beaches. However, the remaining thin slurry of fines and water (8% solids) flowed into the settling basin where the solids settled gradually to form a densified zone of fine tailings at depth. Released water was recycled back to the extraction plant. After a few years, the fines settle to 30 to 35% by weight and are referred to as mature fine tailings (MFT). Further consolidation of the MFT is expected to take centuries [10, 11]. The wettability, aggregation, dispersion, flotation and thickening of kaolinite are affected by its crystal structure and surface properties [7, 12-15]. It is therefore desired to understand the physical and surface chemical properties of kaolinite.

The physical and chemical properties account for the use of kaolinite in all of the above stated applications. The physical properties such as shape, size and the aspect ratio of kaolinite particles are important in their use in papermaking, as a dispersing agent in paints and inks, and in almost all applications. Analysis of the surface chemistry features, such as electrokinetic phenomena, is complicated by the anisotropic, platy structure of the particles, which manifests itself in the presence of both edge surfaces and face surfaces. Even more so, the mineral structure suggests that there should be two types of surface

faces defined by the 001 and the 00$\underline{1}$ basal planes. In this way, ideally, one face should be described as a silica tetrahedral layer and the other face should be described by an aluminum hydroxide (alumina) octahedral layer, as shown in Figure 1.1.

It is believed that the basal planes of kaolinite carry a permanent negative charge due to isomorphous substitution of Al^{3+} for Si^{4+} in the silica tetrahedral, and Mg^{2+} for Al^{3+} in the alumina octahedral layer, whereas the edge surface carries a positive or negative charge depending on the pH of the system. Therefore, it is commonly assumed that the basal planes do not show a surface charge dependency with variation in pH. However, this assumption has never been verified due to the difficulty in isolating the two faces of kaolinite (silica tetrahedral and alumina octahedral faces), and the lack of instrumentation to investigate the two faces when dealing with nanosized particles.

Electrokinetic measurements of kaolinite particles are particularly important in order to describe its surface charge properties and hence its behavior in suspension. The electrophoresis technique is commonly followed to estimate the surface potential/zeta potential of particles as a function of solution pH. Generally, it has been found that kaolinite particles exhibit a negative zeta potential at all pH values greater than pH 3. This negative surface charge of kaolinite particles is similar to the surface charge of quartz particles, which also have a negative zeta potential at pH values greater than pH 3. Although electrophoretic mobility measurements describe the overall electrokinetic characteristics of the anisotropic kaolinite particles, these measurements do not provide details of the charge at various kaolinite surfaces. The surface potential of the kaolinite particle should be defined by the surface charge of its 001 and 00$\underline{1}$ basal planes and edge faces. The basal plane 001 consists of a silica tetrahedral layer, whereas the basal plane

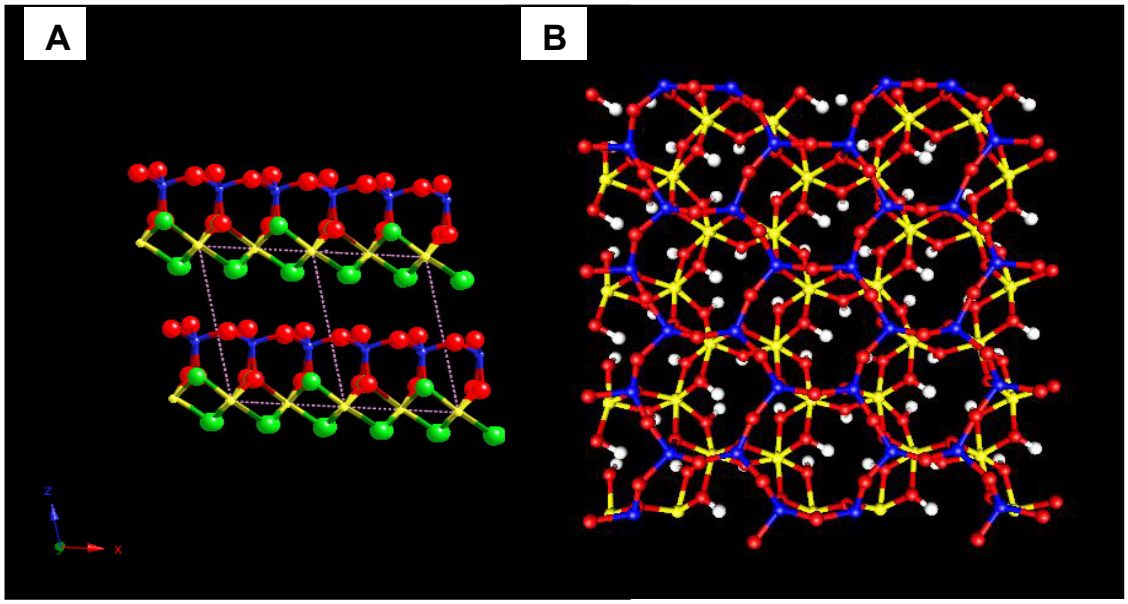

Figure 1.1-Side view (A) and top view (B) of kaolinite (001) surface structure. The silica tetrahedra (red: oxygen, blue: silicon) and the alumina octahedra (yellow: aluminum, green: hydroxyl) bilayers thought to be bound together via hydrogen bonding are illustrated in (A).

00$\underline{1}$ consists of an alumina octahedral layer. The edge faces of broken covalent bonds become hydrated and form silanol and aluminol groups. It is expected, therefore, that the zeta-potential of kaolinite should exhibit the average zeta-potential behavior for pure silica and pure alumina particles. Nevertheless, electrophoresis measurements repeatedly show a negative zeta potential for kaolinite, which reflects the dominance of the silica tetrahedral layer. The reason for this behavior requires clarification. It is realized that the electrophoresis measurements for kaolinite reflect a composite picture of the anisotropic platy shape and the heterogeneous nature of the charge distribution. A complete theory covering arbitrary shape and charge of the particles describing the electrokinetic behavior of the particles is still lacking due to the complexities of particle surface charge and particle shape as well as the motion of such particles in an electric field.

Interactions between particles are important in order to explain the rheology of kaolinite suspensions. The particle interactions are frequently governed by the surface charge properties of kaolinite particles. Traditionally, the basal plane faces (the silica tetrahedral layer and the alumina octahedral layer) were considered similar and thereby, the only interactions considered were those between the face-face, the face-edge and the edge-edge surfaces. It is again emphasized here that in all previous studies, distinction between the basal plane face surfaces (the silica tetrahedral layer and the alumina octahedral layer) had not been made and these face surfaces were assumed to be the same. These different particles interactions are important for they define the aggregation state of the kaolinite particles and the rheology of kaolinite suspensions. The aggregation state will define the network structure of kaolinite particles in suspension whether they form loose aggregates or compact three-dimensional card-house structures. The strength

of these kaolinite aggregates structures is usually characterized by measuring their yield strength and/or viscosity of suspensions. Generally, the yield strength of a particle suspension follows a bell-shaped curve with maximum yield strength at the iso-electric point of the particle. Such behavior has been established for spherical particles with uniform surface charge density. For anisotropic, heterogeneously charged platy-shaped kaolinite particles, the maximum yield strength does not occur at the apparent iso-electric point. This characteristic for maximum yield strength of kaolinite suspensions is not completely understood, and needs to be studied further in order to control suspension properties in many applications such as paper making, composites etc.

1.1 Review of Literature

Clay minerals are abundant in the top soil of the earth's crust. From a practical point of view, they determine the physical and chemical properties of topsoil, farmland and the effectiveness of fertilizers / other chemicals used in agriculture. Technical applications are encountered in the paper industry, in ceramics, in brick production and in the chemical industry. In addition, clays are used for cleaning purposes ("fuller's earth"). Invariably, these applications involve clay minerals as the adsorbent for polymers, monomers and/or ions. The surface chemistry of clay minerals has been studied extensively by colloid scientists and chemists, yet many details have not been established.

The electrical double layers associated with clay particles enter the picture in connection with adsorption phenomenon and in connection with the interaction of clay particles with each other or with other colloidal or suspended materials. Before

discussing the surface properties of clays, we will describe some relevant aspects of clay mineralogy. The readers are advised to refer to the textbooks for detailed study [16-22].

1.2 Clay Mineralogy

The basic structural elements of the clay minerals are *silica tetrahedrons* in which silicon atoms occupy the center and are in tetrahedral coordination with oxygen atoms. Such tetrahedrons are linked by sharing three corners (the basal oxygens) each to form a sheet structure with a hexagonal mesh pattern, as shown in Figure 1.2. The fourth tetrahedral corner (the apical oxygen) points in a direction normal to the sheet and at the same time forms part of an immediately adjacent and parallel *octahedral sheet* in which each octahedron is linked laterally by sharing octahedral edges (see Figure 1.3). The stacking of this bilayer of tetrahedral and octahedral sheets on top of each other forms a kind of "basis kit" from which a variety of clay minerals can be described. The octahedral cations normally are Al, Mg, Fe^{2+} and Fe^{3+}, but other medium sized-cations such as Li, Ti, V, Cr, Mn, Co, Ni, Cu and Zn also occur in some cases [22]. The smallest structure unit contains three octahedra. If all three octahedron are occupied, i.e., have octahedral cations at their centers, the sheet is classified as *trioctahedral*. If only two octahedra are occupied and the third octahedron is vacant, the sheet is classified as *dioctahedral*.

1.2.1 Bilayer Clay Minerals (1:1)

The assemblage formed by linking one tetrahedral sheet with one octahedral sheet is known as bilayer or 1:1 *layer*. In such layers, the uppermost, unshared plane of anions in the octahedral sheet consists entirely of OH groups. For example, kaolinite is a clay

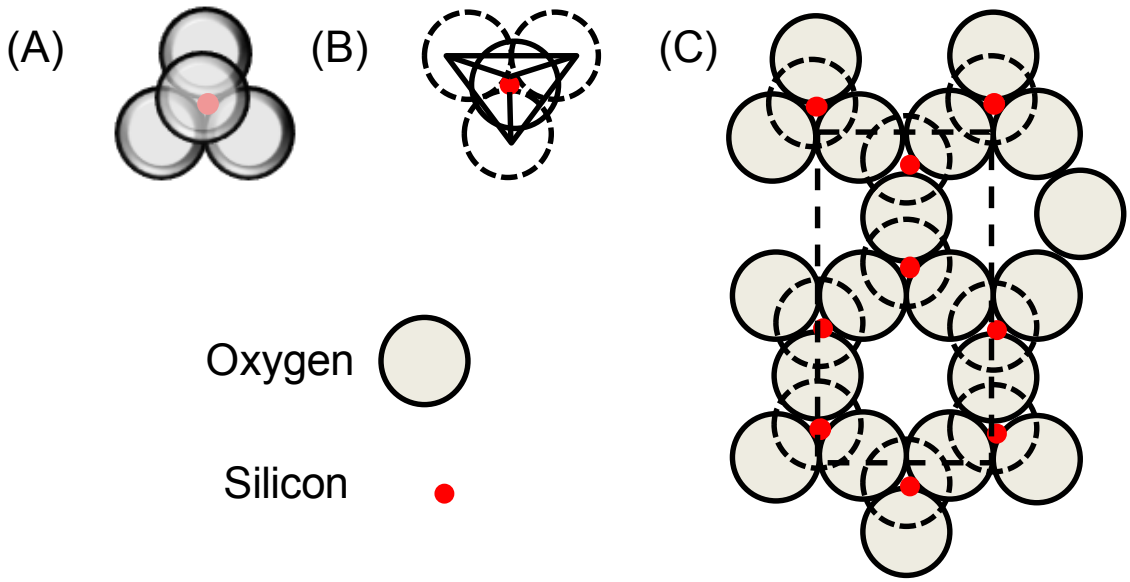

Figure 1.2- Structure of the tetrahedral sheet showing (A) tetrahedral arrangement of Si and O, (B) projection of tetrahedron on plane of sheet, and (C) top view of tetrahedral sheet (dotted line: unit cell area). Large grey circles represent oxygen atoms and the small red circles represent silicon atoms.

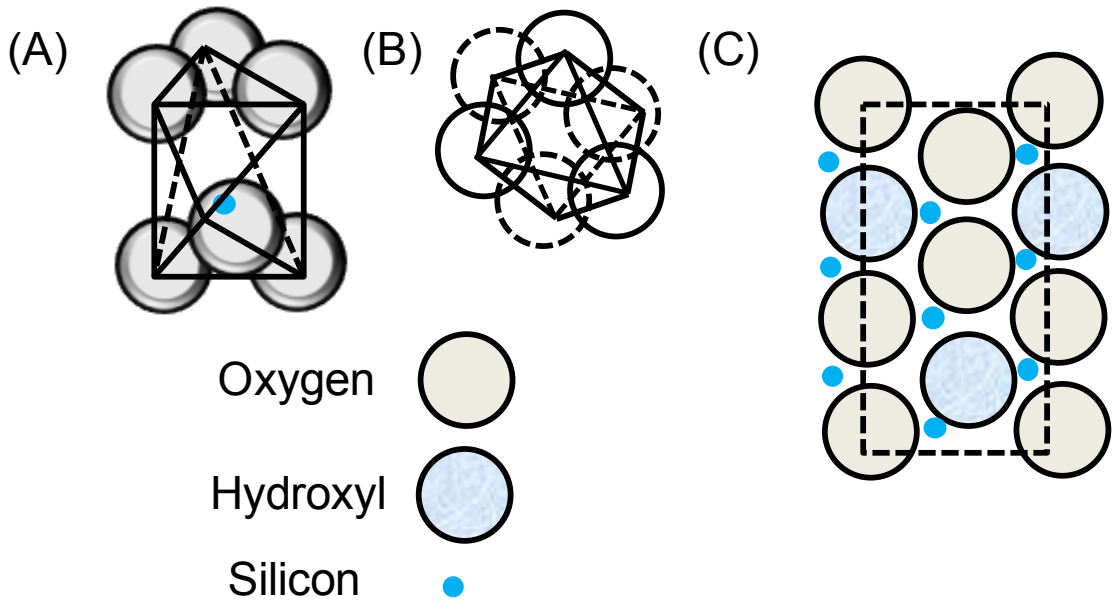

Figure 1.3- Structure of the octahedral sheet showing (A) octahedral arrangement of Al or Mg with O or OH, (B) projection of octahedron in two dimension, and (C) top view of octahedral sheet (dotted line: unit cell area). Large grey circles represent oxygen atoms, large blue circles represent hydroxyl groups and small blue circles represent aluminum atoms.

mineral consisting of a repetition of this bilayer double sheet. The repeating unit has a dimension of 0.72 nm. The double sheets are bonded to each other by hydrogen bonds (involving OH of the octahedral sheet and oxygens of the adjacent silica sheet) and van der Waal forces. The kaolinite has a rigid crystal structure that cannot be swollen by changing pH or solution ionic strength. It is a *nonswelling* clay mineral. In this research work, kaolinite clays will be discussed in greater detail.

1.2.2 Triple Layer Clay Minerals (2:1)

The other category, called 2:1 clay minerals, has a triple layer as the repeating unit. It consists of an alumina or magnesium oxide layer, sandwiched on both sides by silica tetrahedral sheets. The dimension of this trilayer is 1.0 nm thick. The physicochemical behavior of 2:1 clay minerals depends strongly on the degree of substitution of Si^{4+} by Al^{3+} in the tetrahedral layers, and the substitution of Al^{3+} by Mg^{2+} or Fe^{2+} in the octahedral layers. These substitution cause charge imbalance for both 2:1 and also 1:1 clay minerals. The excess layer charge is compensated by various interlayer materials, including individual cations (as in the mica group), hydrated cations (as in smectites), and hydroxide octahedral groups and sheets (as in chlorite minerals). With these basic units, a variety of clay minerals have been identified, depending on the variations in the sequence of the basic building kits or variations in chemical compositions (Mg or Al octahedrons, substitutions of Si^{4+} by Al^{3+} in the tetrahedral layer and Al^{3+} by Mg^{2+} in the octahedral layer, etc.). Clay minerals are classified into eight major groups, on the basis of layer type (1:1 or 2:1), layer charge and type of interlayer, as presented in Table 1.2.

Table 1.2- Classification of layered silicate minerals [22]

Layer Type	Group	Sub-group	Species
1:1	Sepentine – Kaolin	Serpentines	Lizardite, Antigorite, Chrysotile
		Kaolins	Kaolinite, Dickite, Nacrite
2:1	Talc-Pyrophillite	Talcs	Talc, Willemseite
		Pyrophyllites	Pyrophyllite
	Smectite	Saponites	Saponite, Hectorite
		Montmorillonites	Montmorillonite, Beidellite
	Vermicullite	Trioctahedral Vermicullite	Trioctahedral Vermicullite
		Dioctahedral Vermicullite	Dioctahedral Vermicullite
	Mica	Trioctahedral Mica	Phlogopite, Biotite, Lepidolite
		Dioctahedral Mica	Muscovite
	Brittle Mica	Trioctahedral Brittle Mica	Clintonite
		Dioctahedral Brittle Mica	Margarite
	Chlorite	Trioctahedral Chlorites	Clinochlore
		Dioctahedral Chlorites	Donbassite
		Di,trioctahedral Chlorites	Cookeite
2:1 Inverted Ribbons	Sepiolite-Palygorskite	Sepiolites	Sepiolite
		Palygorskites	Palygorskites

1.3 Kaolinite Structure

The kaolinite structure as described above consists of a sheet of $(Si_4O_{10})^{4-}$ formed by the linkage of SiO_4 tetrahedra in a hexagonal array, the vertices all pointing in one direction. The apical oxygens, together with some additional $(OH)^-$ ions located over the center of hexagons, form the base of a gibbsite-type layer or alumina octahedral layer. The structure of kaolinite is shown in Figure 1.4. Kaolinite has triclinic unit cell crystal structure with a = 5.15 Å, b= 8.95 Å, c= 7.39 Å, $\alpha = 91.8°$, $\beta = 104.8°$ and $\gamma = 90°$.

1.4 Kaolinite Chemistry

The chemical formula of kaolinite can be written in terms of oxides as $Al_2O_3.2SiO_2.2H_2O$. The chemical analysis indicates that various ions may substitute in the structure, for example Al^{3+} for Si^{4+} in the silica tetrahedral layer, and Mg^{2+} or Fe^{2+} for Al^{3+} in the alumina octahedral layer [23].

Kaolinite has a low cation exchange capacity of about 5 meq/100 g compared with other 2:1 type clay minerals such as montmorillonite (100 meq/100g) [16, 24]. The anion exchange capacity of kaolinite on the other hand is higher than its cation exchange capacity, and may be attributed to the replaceable $(OH)^-$ ions of the exposed alumina octahedral layer.

Kaolinite contains little or no surface adsorbed water in its structural unit; therefore, most of the dehydration (loss of constitutional OH) takes place between 400℃ and 525℃. When the kaolinite minerals are heated so that all water molecules and $(OH)^-$ ions are driven off at about 800℃, the product is called metakaolinite. When kaolinite minerals are heated beyond 800℃, the layered structure is further disrupted and cannot

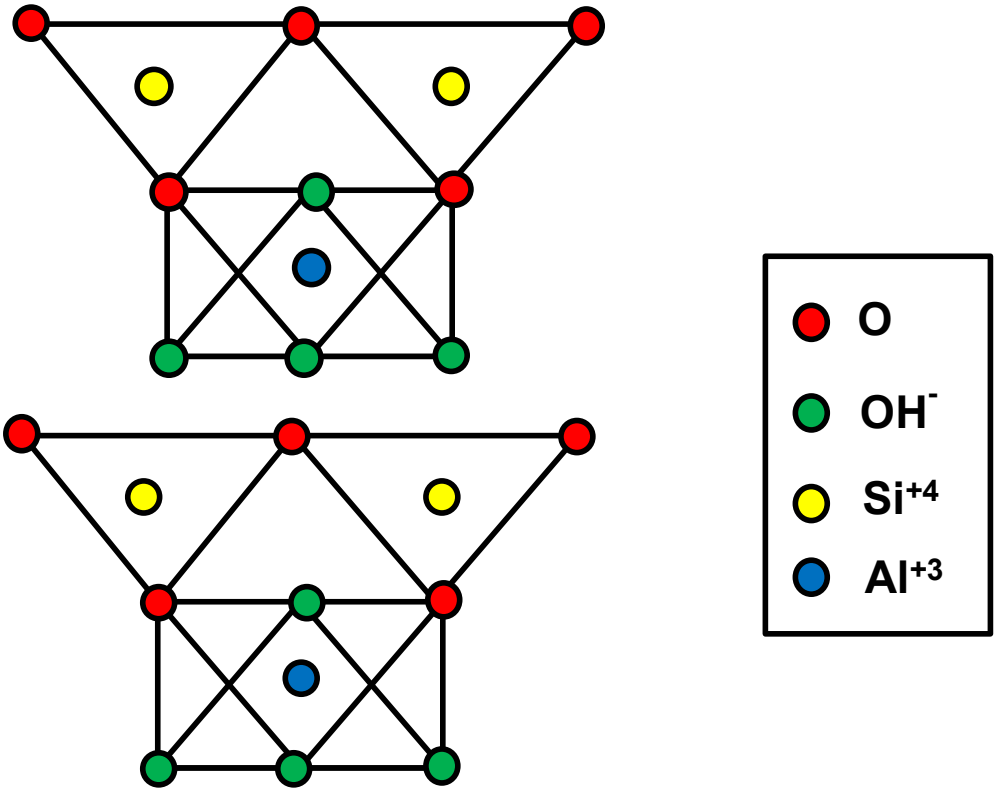

Figure 1.4- The structure of kaolinite clays.

be reconstituted by rehydration. The final products of thermal decomposition are mullite and cristobalite.

1.5 Kaolinite Optical and Physical Properties

The kaolinite may occur in compact massive blocks, in vermin-form or granular aggregates, as radiating platelets, or as piles of platelets or 'books.' Kaolinite shows a perfect cleavage along the 001 plane. The particles are white in color, sometimes with reddish, brownish or bluish tints; and colorless in thin sections. The refractive index values for kaolinite are:

n_α = 1.553 - 1.563, n_β = 1.559 - 1.569, and n_γ = 1.560 - 1.570

1.6 Kaolinite Genesis

Kaolinite occurs in hydrothermal, residual and sedimentary deposits. The hydrothermal and residual occurrences are called primary and the sedimentary occurrences are referred to as secondary deposits. Primary kaolins are those that have formed in situ by the alteration of crystalline rocks such as granites and rhyolites. The alteration results from surface weathering, groundwater movement below the surface or hydrothermal action. Secondary kaolins are sedimentary and were eroded, transported and deposited as beds or lenses associated with sedimentary rocks.

Kaolin minerals form at relatively low temperatures and pressures. The most common parent minerals are feldspar and muscovite, both of which contain desired alumina and silica from which the kaolin minerals are formed. The transformation of

potassium feldspar into kaolinite occurs by intense weathering of the feldspar and leaching of K and SiO_2 according to the equation:

Potassium Feldspar Kaolinite Silica Potash

$$2KAlSi_3O_8 + 3H_2O \rightarrow Al_2Si_2O_5(OH)_4 + 4SiO_2 + 2KOH$$

All of the potassium must be lost in solution because small amounts of unleached potassium favor illite formation rather than kaolinite. Dissolution is essential to chemical weathering and to the formation of kaolinite. A few researchers [14, 25] studied the dissolution reaction of kaolinite, and determined the free energy of formation of kaolinite ranged from -902.5 to -903.8 kcal/mol [25]. Kittrick concluded from the solubility experiments that the ion activities during kaolinite dissolution appears to be controlled by soluble small particles, which may be present as impurities [25].

1.7 Surface Chemistry of Kaolinite

The surface chemistry features of kaolinite reside in its bilayer structure, which is composed of one sheet of silica and a sheet of alumina. The basal planes of kaolinite are thus half siloxane and half hydroxylated alumina. When these anisotropic structural features are considered together with chemical features, further understanding of the electrokinetic behavior can be obtained.

It is well known that kaolinite has a heterogeneous surface charge. The basal planes of kaolinite (silica tetrahedral layer and alumina octahedral layer) are commonly assumed to carry a constant structural charge due to isomorphous substitution of Al^{3+} for

Si^{4+} in the silica tetrahedral layer and Fe^{2+} or Mg^{2+} for Al^{3+} in the alumina octahedral layer. The charge on the edge surfaces is due to the protonation / deprotonation of surface hydroxyl groups, and therefore depends on the solution pH [16, 23, 26-28]. However, this assumption has never been verified due to the difficulty in isolating the two faces of kaolinite (silica tetrahedral and alumina octahedral faces), and the lack of instrumentation to investigate the two faces when dealing with nanosized particles.

The earlier studies were concentrated to determine the cation exchange capacity of kaolinite. Depending on the different counterions and source of kaolinite, different values for cation exchange capacity for kaolinite are reported in the literature in the range of 36-100 μ-mole/g [29-32]. Ferris and Jepson [29] do not agree that kaolinite has definite cation exchange capacity. They concluded that a structural charge does not exist on the basal surface of their kaolinite samples.

The surface charge density for kaolinite particles was also determined by titration [14, 33-37]. Despite these numerous studies, experimental results are still disparate. The pH_{PZNPC} (point of zero net proton charge) for kaolinite varies from pH 4 [33] to pH 7.5 [14]. One reason for these discrepancies could be linked to contrasting experimental methods: some researchers used continuous potentiometric titrations with short equilibration times [14, 37], while others used potentiometric measurements in batch experiments over long equilibration times [33, 34, 38].

The iso-electric point of kaolinite as determined by electrophoresis is quite intriguing, as one would expect that the kaolinite particles should show the iso-electric point at pH of 5.7 as an average of silica (iso-electric point at pH of 2.2) and gibbsite (iso-electric point at pH of 9.2), since the composition of silica to alumina in kaolinite is

nearly 1:1. However, the iso-electric point of kaolinite particles as measured by electrophoresis is consistently less than pH 3, which is more closely related to the iso-electric point of silica [29, 39-45]. However, it was pointed out that the zeta potential of kaolinite inferred from the electrophoretic mobility using the Smoluchowski equation has been criticized because of the heterogeneous nature of the surface charge, and the hexagonal shape of the particles [15, 24, 46]. The calculation of zeta potential and surface charge densities for nonspherical kaolinite assuming an equivaent sphere may result in quite misleading values. The zeta potentials calculated from such mobilities do not reflect the potential at the shear plane because of the screening effect of positive charges on the edges relatives to those of negative charges at faces, resulting in lower negative mobility [47].

The surface charge properties of kaolinite will have an influence on the particle interactions in a suspension and thereby affecting its rheological properties. Several researchers have defined the rheological properties of kaolinite, and have explained the abnormal behavior of a maximum yield stress for kaolinite suspensions at pH 5-5.5 [26, 48-50]. Such a maximum might be expected at kaolinite's iso-electric point of pH < 3 [51, 52]. Johnson *et al.* [49, 50] followed the common assumption the basal planes of kaolinite are permanently negative charged and explained this abnormal rheological behavior based on the aggregation behavior of kaolinite particles, which is described mainly by favorable interactions between negatively charged faces and positively charged edges. On this basis, the maximum shear-yield stress at pH 5.5 was explained. However, the kaolinite particle interactions theory should be considered carefully due to the

underlying assumption of negatively charged faces (silica face and alumina face) of kaolinite.

Limited research has been reported on the experimental characterization of the face surfaces and edge surface of kaolinite [15]. A few studies have reported the average FTIR spectra of both faces of kaolinite [53-55]. Recent development of advanced analytical techniques (XPS - X-ray photoelectron spectroscopy, LEISS - Low energy ion scattering spectroscopy, and ToF-SIMS - Time of flight-secondary ions mass spectroscopy) seem promising to facilitate investigation of the two faces of kaolinite provided that the particles can be oriented, and that the instrumentation is sufficiently surface sensitive to collect signals from just the very first layer. For example, a recent study attempted to use ToF-SIMS to study the talc surface [56]. However, these results were averaged over a few layers of talc. Johnston [57] examined the hydrogen bonding for kaolinite particles using vibrational spectroscopy and concluded that the type and strength of interlayer hydrogen bonds of the structural OH groups govern their size, shape and their surface chemistry. In addition, they also revealed an additional set of 'disorder-indicator' bands of disordered kaolinite using FTIR spectroscopy. Recently, many researchers have used scanning electron microscopy (SEM) [58, 59], transmission electron microscopy (TEM) [60] and atomic force microscopy (AFM) [59, 61, 62] as imaging tools to characterize particle shape and morphology.

1.8 Overall Objective

The overall objective of this dissertation research is to investigate the physical characteristics, structure and surface chemistry features of kaolinite in order to further

explain the electrokinetic behavior of kaolinite particles, their interactions and the rheology of their aqueous suspensions.

1.9 Research Organization

Chapter 2 discusses the literature review of the physical and chemical properties of kaolinite. Different instrumentation techniques are discussed in order to characterize these properties of kaolinite.

Chapter 3 discusses the physical properties (shape and size) and chemical composition of kaolinite. This study focuses on the surface properties of a very high purity kaolinite sample from St. Austell area in Cornwall, UK. A pool of advanced analytical techniques were utilized to investigate the morphological and surface properties of kaolinite, including Brunauer-Emmett-Teller (BET) surface area measurements, X-ray diffraction (XRD), X-ray fluorescence (XRF), scanning electron microscopy (SEM), atomic force microscopy (AFM), Fourier-transform infrared spectroscopy (FTIR) and ion scattering spectroscopy (ISS).

Chapter 4 discusses surface force measurements made by AFM using a silicon nitride tip in order to interrogate the surface charge characteristics of the silica and the alumina faces of 500 nm size kaolinite particles, and their dependence on solution pH. A protocol for surface force measurements was developed. To order kaolinite particles with the silica face exposed, a negatively charged glass-substrate was used so that the alumina face of kaolinite was attracted to the glass-substrate. In contrast, to expose the alumina face of kaolinite particles, a positively charged fused alumina-substrate was used so that the silica face attached to the fused alumina-substrate. The surface force measurements

were analyzed using DLVO theory, and on this basis, the surface charge characteristics of the silica and the alumina faces of kaolinite are established.

Chapter 5 discusses the electrokinetic features of kaolinite particles as investigated using electrophoresis, potentiometric titration techniques (M-R titration and acid-base titration) and surface force measurements. The differences in the results between electrophoresis and potentiometric titration are explained with the limitation of the current electrokinetic theory for the anisotropic and platy nature of the kaolinite particles.

Chapter 6 discusses rheological measurements conducted to study particle interactions in kaolinite suspensions, and to further explain the anomalous behavior of concentrated kaolinite suspensions showing maximum yield strength at pH 5-5.5. The surface charge data of the silica face surface, the alumina face surface and the edge surface were used to describe particle interactions and the rheological behavior of kaolinite suspensions. The interactions between different faces of kaolinite particles – the silica face surface, the alumina face surface and the edge surface are considered and the aggregation state of kaolinite particle suspensions is discussed.

Chapter 7 discusses the identification of the silica face and alumina face of kaolinite by atomic force microscopy. The edge surface is examined by high resolution transmission electron microscopy. The basal plane surfaces and the edge surfaces of kaolinite were further investigated using atomic force microscopy, and high resolution transmission electron microscopy, respectively, in order to verify whether the faces can be distinguished from one another. For example, the mineral structure suggests that there should be two types of surface faces defined by the 001 and the 00$\underline{1}$ basal planes. In this

way, one face should be described as a silica tetrahedral layer and the other face should be described as an aluminum hydroxide (alumina) octahedral layer. For confirmation, the crystal lattice structure of the silica face surface and the alumina face surface were investigated using atomic force microscopy, whereas the lattice fringe pattern of the kaolinite edge faces was investigated using high resolution transmission electron microscopy.

Finally, Chapter 8 discusses the milestones achieved in this dissertation and suggests some new directions for future research on other clay minerals in general and kaolinite in particular.

CHAPTER 2

CHARACTERIZATION OF KAOLINITE PARTICLES

This chapter discusses a pool of advanced analytical techniques utilized to investigate the morphological and surface chemistry features of kaolinite. X-ray fluorescence (XRF) spectrometry was used to determine the chemical composition of kaolinite, and thereby predict the structural formula as $(Si_{3.94}Al_{0.06})^{IV}(Al_{3.99}Fe_{0.01})^{VI}O_{10}(OH)_8Fe_{0.01}Ca_{0.01}Mg_{0.01}K_{0.02}Na_{0.005}$. X-ray diffraction analysis (XRD) showed that kaolinite was the dominant mineral phase with some minor impurities of quartz and anatase. Scanning electron microscopy (SEM) and atomic force microscopy (AFM) confirmed the platy nature and hexagonal to subhedral shape of kaolinite. The median diameter and thickness of kaolinite was determined as 600 nm and 11 nm, respectively.

The surface chemistry features as revealed by Fourier transform infrared spectroscopy (FTIR) determined the OH group vibrations of the kaolinite surface from the inner OH group stretching vibrations at 3620 cm^{-1}, and inner-surface OH group vibrations at 3691 cm^{-1}, 3668 cm^{-1} and 3651 cm^{-1}. Low energy ion scanning spectroscopy (ISS) revealed an overlapping band of Si/Al elements detected from the silica and alumina faces of kaolinite. These surface analytical techniques offer better understanding of the surface chemistry and bonding details of kaolinite and other clay mineral surfaces.

2.1. Introduction

Kaolinite clays are extensively used in the paper, ceramic, paint, plastic, rubber and cracking catalyst industries, yet their surface properties are not completely understood [1, 63-68]. A complete understanding of the surface chemistry features and morphological properties of kaolinite crystallites is desired in order to better control its properties in the above said applications and many new applications such as smart materials and clay-polymer nanocomposites.

The chemical structure of kaolinite is $Al_2Si_2O_5(OH)_4$, which represents two-layer silicates and are known to consist of a silica tetrahedral layer covalently bonded to alumina octahedral layer through an apical oxygen atom, as shown in Figure 2.1. Kaolinite is found as pseudo-hexagonal triclinic crystals. These particles have a maximum dimension less than 2 μm, a thickness of 0.72 nm and a density of 2.6 g/cm^3. The lattice parameters of kaolinite are a = 0.515 nm, b = 0.895 nm, c = 0.740 nm, α = 91.68°, β = 104.87°, γ = 89.9° [17].

The surface chemistry features, particularly the charge properties of kaolinite, have been investigated by many researchers [14, 23, 26, 34, 35, 41, 50, 69-71]. However, the surface charge properties have been explained based on the commonly followed assumption that the basal planes of kaolinite carry a permanent negative charge due to isomorphous substitution of Al^{3+} for Si^{4+} in the silica tetrahedral, and Mg^{2+} for Al^{3+} in the alumina octahedral layer, whereas the edge surface carries a positive or negative charge depending on the pH of the system. This assumption was only recently examined by surface force measurements on the two faces of kaolinite using atomic force microscopy [72].

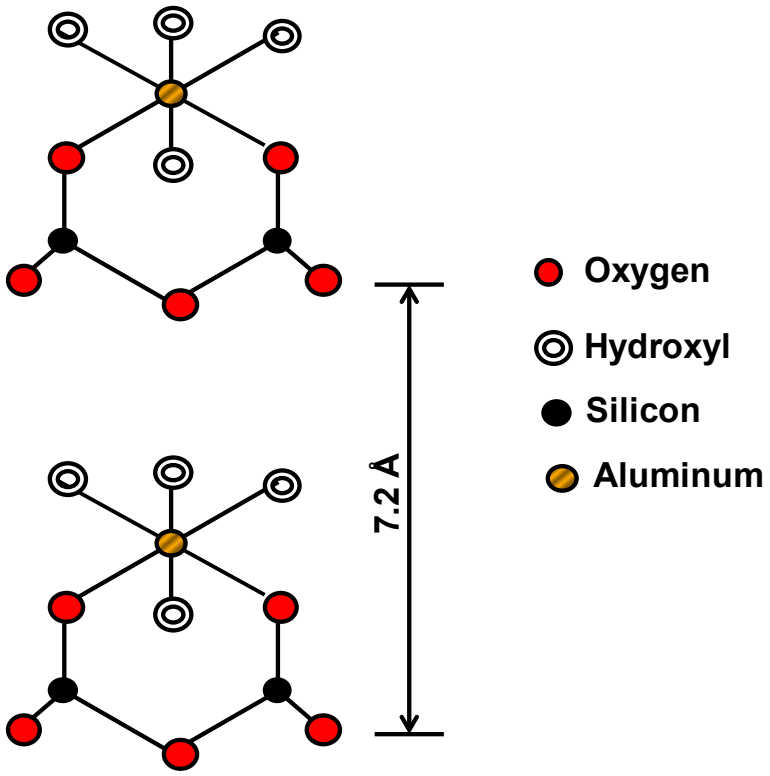

Figure 2.1- Structure of kaolinite showing the relative spacing between the layers.

It was demonstrated that the silica tetrahedral face of kaolinite is negatively charged at pH > 4, whereas the alumina octahedral face of kaolinite is positively charged at pH < 6, and negatively charged at pH > 8.

A few studies have reported the Fourier transform infrared (FTIR) spectra of kaolinite [53-55, 73]. Recent development of advanced analytical techniques such as XPS - X-ray photoelectron spectroscopy, LEISS - Low energy ion scattering spectroscopy, and ToF-SIMS - Time of flight-secondary ions mass spectroscopy seem promising to facilitate investigation of the basal plane surfaces of kaolinite, provided the particles can be oriented and that the instrumentation is sufficiently surface sensitive to collect signals from just the very first surface layer. For example, a recent study attempted ToF-SIMS analysis to study the talc surface [56]. However, these results were averaged over a few layers at the talc surface.

Cases *et al.* [74] used low-temperature adsorption calorimetry, shadowed transmission electron microscopy, adsorption isotherms of alkyldodecylammonium ions and particle size distribution curves to obtain morphological information. Recently, many researchers have used scanning electron microscopy (SEM) [58, 59], transmission electron microscopy (TEM) [60, 75] and atomic force microscopy (AFM) [60, 62, 76] as imaging tools to characterize particle shape and morphology. However, none of the studies, to the knowledge of the author, have used a pool of surface analytical instruments to characterize the surface chemistry features and the morphological properties of kaolinite crystals.

The objective of this chapter is to characterize the morphological and surface chemistry features of the kaolinite surface through a pool of advanced analytical techniques in order to better understand its surface properties.

2.2. Materials and Methods

2.2.1 Sample Preparation

A clean English kaolin (Imerys Inc., UK) was obtained from the St. Austell area in Cornwall, UK. The sample was cleaned with water only using elutriation to achieve classification at a size of less than 2 μm. No other chemical treatment was done. Further details about the kaolinite extraction and preparation are given in the literature [77]. The kaolinite was used as received in this research. All liquid suspensions were prepared in high purity Milli-Q water (Millipore Inc.). The resistivity of the water was above 18 MΩ-cm in all experiments.

2.2.2 Surface Area

The surface area of the particles was determined using the BET method following the monolayer adsorption of N_2 gas on the particle surface. A solid sample is pretreated (degassed) in a special container by applying heat and vacuum to remove adsorbed contaminants acquired from the atmospheric exposure. The container with the sample is then transferred to the analysis port where it is cooled to cryogenic temperatures, then is exposed to N_2 gas at a series of precisely controlled pressures. With each incremental pressure increase, the number of gas molecules adsorbed on the surface increases. The pressure at which adsorption equilibrium occurs is measured and the universal gas law is

applied to determine the quantity of the gas adsorbed, and subsequently the sample surface area.

2.2.3 Chemical Composition

The kaolinite chemical composition was determined using X-ray fluorescence (XRF) spectrometry. The elemental composition was determined using energy dispersive spectrometry (EDS). The kaolinite powder was sprayed on dual side sticky carbon tape which in turn is glued to the standard metal stub for EDS analysis. A brief introduction of both techniques is presented in the following subsections.

2.2.3.1 Energy Dispersive Spectrometry (EDS)

When the electron beam strikes the sample, X-rays are produced from interactions of the beam with the sample. The X-ray produced can be placed into two broad categories, white X-rays and characteristic X-rays. When an electron beam is in-elastically scattered by the nucleus, the electrons lose energy, resulting in the formation of white X-rays. These X-rays do not have energies characteristics of the sample composition, but instead have a variety of energies ranging up to that of the incident beam. However, when the beam electron strikes an inner shell electron, the primary electron beam loses energy equivalent to the binding energies of the K, L or M shells, and the electrons are ejected. The difference in energy results in either the production of characteristic X-rays or the ejection of the Auger electron. Characteristic X-rays are called such because the energy of the X-rays produced can be used to identify the elements present in the sample.

An X-ray spectrum is collected for an area of specimen using an energy dispersive X-ray analyzer (EDS) or multiple X-ray goniometers. These spectra can be used to obtain an estimate of the chemical composition of the selected area. The chemical composition of the area impacted by the electron beam can be estimated using EDS by viewing a graph with the energy of the X-rays produced on the x-axis and the number of X-rays counted at that energy on the y-axis. The regions appearing as peaks are the result of characteristic X-rays production, while the intensity in the regions between peaks in the result of white X-rays. In general, the relative intensity of the EDS peaks is proportional to the relative composition on the molar basis.

2.2.3.2 X-ray Fluorescence Spectroscopy (XRF)

X-ray fluorescence spectroscopy (XRF) is a method of elemental analysis, which assesses the presence and concentration of various elements in the powder sample by measuring the characteristic secondary radiation emitted from a sample that has been excited with an X-ray source. A good review of XRF treatment could be found elsewhere [78-83], and only a brief description is provided here.

When a primary X-ray excitation source from an X-ray tube or a radioactive source strikes a sample, the X-ray can either be absorbed by the atom or scattered through the material. The process in which an X-ray is absorbed by the atom by transferring all of its energy to an innermost electron is called the "photoelectric effect." During this process, if the primary X-ray had sufficient energy, electrons are ejected from the inner shells, creating vacancies. These vacancies present an unstable condition for the atom. As the atom returns to its stable condition, electrons from the outer shells are transferred to

the inner shells and in the process, give off a characteristic X-ray whose energy is the difference between the two binding energies of the corresponding shells. Because each element has a unique set of energy levels, each element produces X-rays at a unique set of energies, allowing one to nondestructively measure the elemental composition of a sample. The process of emissions of characteristic X-rays is called X-ray fluorescence, or XRF. In most cases, the innermost K and L shells are involved in XRF detection.

The difference between EDS and XRF is the type of radiation hitting the sample. EDS uses an electron beam while XRF uses an X-ray beam. Due to the small beam size possible with electrons, elemental analysis can be obtained for volumes as small as 1 μm in diameter.

2.2.4 Mineralogy

X-ray diffraction (XRD) is a technique that provides detailed information about the atomic structure of crystalline substances. It is a powerful tool in the identification of minerals in rocks and soils. XRD has long been a mainstay in the identification of clay-sized minerals in soils.

Many references are available which describe XRD principles in detail [84, 85]. Other useful sources of information about XRD theory and interpretation applied specifically to powder methods are also available [86-88]. The following section provides a brief introduction to some fundamental aspects of XRD.

X-ray diffraction analysis uses monochromatic radiation. Intense X-radiation at a specific wavelength can be produced when electrons from a source (e.g., tube filament) dislodge inner shell electrons from the atoms of a metal target. Instantaneous replacement

of the dislodged electron by an electron from a specific energy shell results in the quantum release of a packet of energy corresponding to a specific wavelength and termed characteristic radiation. The characteristic radiation used in XRD, termed Kα, is produced by replacement of K shell electrons by L shell electrons.

X-ray diffraction occurs when X-rays are scattered by atoms arranged in an orderly array in crystals. The atoms serve as scattering centers reemitting X-rays at the same wavelength as the incident radiation in all directions (coherent scattering) [88]. The orderly arrangement of atoms results in the scattered X-rays within the crystal being (i) in phase in specific directions dictated by symmetry and atomic spacing and (ii) out of phase in all direction. The X-rays that are in phase constructively interface and emerge as intense beams (diffracted beams) from the crystal, while those that are out of phase destructively interface and hence have minimal emergence. The systematic combination of constructive and destructive interference arising from the periodicity of atoms in crystals is X-ray diffraction.

The diffractometer records the intensity of the diffracted beam electronically at precise angles as the specimen is scanned over an angular range. These intensity patterns at specific angles are matched with the intensity of standard samples at precise angular locations. The mineralogical information from the sample is thus obtained.

In this dissertation research, the kaolinite powder was characterized for the identification of different mineral phases using a Siemens D5000 X-ray powder diffractometer (Bruker AXS, Inc., Madison, WI, USA) in the range of $10^0 \leq 2\theta \leq 100^0$ with Cu-Kα radiation monochromated with a curved-graphite monochromators placed after the sample, at 40 KV and 30 mAmps. The kaolinite powder was packed in a

standard flat sample holder without any special treatment. The step scan technique was employed at an interval of 0.02^0/0.8 seconds. X-ray diffraction (XRD) data thus obtained was analyzed using Diffrac Plus v 3 software (Bruker AXS, Inc., Madison, WI, USA).

2.2.5 Kaolinite Particle Size and Thickness

The kaolinite particles shape and thickness was characterized using environmental scanning electron microscopy (ESEM) and atomic force microscopy (AFM). The description of SEM and AFM imaging procedures is discussed below.

2.2.5.1 Scanning Electron Microscopy (SEM)

Scanning electron microscopy (SEM) has diverse uses for the study of clay minerals. The SEM has a large magnification range, allowing examination of solids with almost no magnification to imaging at well over 100,000 times. Another important feature is the large depth of field of SEM images, which have a three-dimensional perspective. In this way, an SEM image provides much more information about a specimen's topography and surface structures than light microscopy at the same magnification.

The first prototype SEM was constructed by Knoll and von Ardenne in Germany. Following several refinements made by Zworykin, as well as improvements made by Mcullan and Oatley, the first commercial SEM became available in 1963. The environmental scanning electron microscope (ESEM) is a recent modification of the traditional SEM. The major difference between ESEM and traditional SEM is the much higher specimen chamber pressures that are allowed in the ESEM. A differential

pumping system allows pressures of several hundred Pa in the specimen chamber while maintaining a pressure of 1.3×10^{-11} MPa near the electron gun. The high vacuum near the electron gun makes it possible to use high intensity filaments such as a LaB_6 filament and get a significant signal despite the higher pressure in the sample chamber.

The SEM can be subdivided into a number of components such as the electron optical system, specimen stage, secondary electron detector and vacuum system. An electron optical system is involved in the focusing and control of the electron beam. A specimen stage is needed so that the specimen may be inserted and situated relative to the beam. A secondary electron detector is used to collect the electrons and to generate a signal that is processed and ultimately displayed on viewing and recording monitors. A vacuum system is necessary to remove air molecules that might impede the passage of the high energy electrons down the column as well as to permit the low energy secondary electrons to travel to the detector. Greater details about SEM principles and operation are available in the literature [89].

2.2.5.2 Atomic Force Microscopy (AFM)

Atomic force microscopy (AFM) was invented in 1986 by Binnig *et al.* [90] and has since become an important instrument for high resolution imaging of the micro-to-nano-morphology of surfaces, a technique to probe fundamental intermolecular forces between substances, and a tool to manipulate atoms and molecules. The technique is particularly important to various aspects of soil science and biogeochemistry because it allows for high resolution imaging of organic, microbial and mineral surfaces and

characterization of surface chemical properties under environments relevant to extreme conditions.

The basic operating principles of AFM have been described previously in the literature [90, 91] and are reviewed in brief here. For most commonly used AFMs, a sample is mounted atop a piezoelectric scanner composed of materials such as lead-zirconium-titanite that permit movement with Angstrom-level precision (see Figure 2.2). The sample is scanned continuously in two dimensions (x-y) beneath a force sensing probe consisting of a tip that is attached to or part of a cantilever. Z-direction (height) movements are also made by the scanner as required to compensate for changes in sample height or forces between the tip and the sample. Attractive and repulsive forces between the tip and the sample cause the cantilever to bend or defect. This deflection can be monitored in a number of ways. Most commonly, laser light reflects off the back of the cantilever into a photodiode detector. This so-called optical-lever detection system is sensitive to Angstrom-level movements of the cantilever [92-94]. For soil microbiologic purposes, some AFMs keep the sample stationary while the scanner rasters the cantilever above it, so that the AFM can be used concurrently with an inverted optical microscope.

The most common mode of AFM imaging is the so-called contact mode. Contact-mode imaging can be conducted in air or immersed in a liquid such as an electrolyte solution. In contact-mode AFM, the tip is brought directly into contact with the sample surface, which is scanned beneath it. The tip-sample interaction is primarily repulsive in nature (e.g., due to the short-range forces associated with the Pauli Exclusion Principle). The interaction force can be as low as 10^{-9} N, which is approximately the interaction force between atoms in solids. Once the tip is brought in contact with the sample surface,

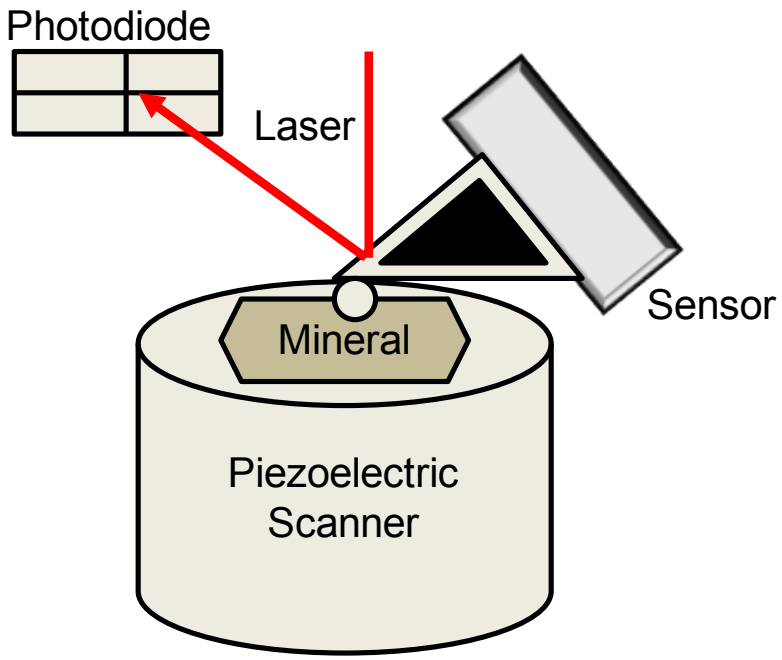

Figure 2.2- Schematic representation of AFM. A mineral sample is positioned on a piezoelectric scanner, which moves the sample in three-dimensions relative to the sensor (cantilever). The cantilever deflects due to attractive or repulsive forces between the tip and the sample. Deflection of cantilever is monitored by a laser reflecting off the top and into a photodiode array.

the piezoelectric scanner drives the sample upward in the z-direction a predefined distance. This causes the cantilever deflect. The predefined cantilever deflection is present by the system software and is known as the “set point.” A feedback loop maintains a constant set-point level throughout the imaging process. When the tip goes over a feature on the sample surface, the computer feedback loop adjusts the z-piezo to keep the cantilever deflection, at the set-point value. The imaging is conducted at a constant force, so that this mode of imaging is often called “constant force” imaging. The greater the cantilever deflection, the higher the imaging force exerted by the tip on the sample. A three-dimensional AFM image is generated as the computer plots the correction to the z-piezo as a function of x-y position throughout the scan.

The kaolinite particles images were obtained with an FEI Quanta 600 FEG environmental SEM (FEI, Oregon, USA) under low voltage of 5 KV to avoid charging. A drop of kaolinite suspension (1000 ppm) in Milli-Q water at pH 9 was placed on a freshly cleaved mica sheet. The mica sheet was heated on a hot plate to immediately dry the suspension. In this way, the kaolinite particles were dispersed on the mica substrate and separated by several microns [62]. The mica sheet was then attached to a sample holder using dual sided sticky tape for ESEM analysis. The images were obtained as received, without any conductive coating. After the images were captured, 150 kaolinite particles were analyzed using Image-J software for area distribution. Only those particles which lie flat on the substrate and which were not aggregated were analyzed. A mask was created on the particle following its profile, and then the area was determined by the pixels area fitted in that mask. The particle diameters were determined from the ESEM images based on the equivalent circular disc area.

The kaolinite particle thickness and diameter (longest dimension) was also determined using AFM. A picoforce AFM with Nanoscope V controller (Veeco Instruments Inc., Santa Barbara, CA) was used with a PF-type scanner designed for picoforce measurements. Triangular beam silicon nitride (Si_3N_4) cantilevers (Veeco Instruments Inc., Santa Barbara, CA) having pyramid-shaped tips with spring constants of about 0.12 N/m were used. The kaolinite samples were prepared in a similar fashion on mica substrate as for the ESEM study. The topography (height) images were obtained with the contact mode in air. The images were analyzed using Nanoscope v 7.2 software (Veeco Instruments Inc., Santa Barbara, CA). The section analysis feature of the software was used to obtain the particle thickness and the longest dimension from the height images.

2.2.6 Surface Spectroscopy of Kaolinite

Surface properties of kaolinite play an important role in the adsorption, dissolution and precipitation of ions in the solution. In recent years, the development of surface sensitive analytical techniques, e.g., X-ray photoelectron spectroscopy (XPS), ion scattering spectroscopy (ISS), auger electron spectroscopy (AES), secondary ion mass spectroscopy (SIMS), Fourier transform infrared spectroscopy (FTIR) etc. have allowed direct probing of surface phenomenon. Of these surface techniques, XPS is widely used to obtain elemental, chemical state and semiquantitative compositional information from clay such as kaolinite and other minerals. ISS has recently gained significant attention to obtain the elemental information from the very first atomic layer of crystalline minerals.

XPS, ISS and FTIR are used in this study for obtaining elemental information from the kaolinite surface, and will be discussed in the subsequent sections.

2.2.6.1 X-ray Photoelectron Spectroscopy (XPS)

X-ray photoelectron spectroscopy (XPS) technique is popular among soil- and geo-chemists because it provides elemental, chemical state and semiquantitative compositional information. XPS is particularly useful in the determination of surface elemental composition [95-97]; site occupancy [97]; oxidation and reduction chemistry [98]; chemical weathering [99, 100]; Lewis and Brønsted acid sites [101]; adsorption of cations and anions, chemical bonding and surface reactivity [102-104] and differentiation of exchangeable and nonexchangeable clay components [97]. These reviews discuss elegant applications of XPS to geo- and soil-chemistry research. The principles of XPS are briefly reviewed below.

When a solid material is bombarded by a photon, the photon's energy is transmitted to an electron. The electron can be ejected from the atom provided the photon is of sufficient energy. This process is called photoemission and is shown in Figure 2.3. When the excitation occurs sufficiently close to the surface, the photoelectron can escape from the material. The photoelectron leaves the atom in an excited state which then must lose the energy gained. The excess energy can be lost through various de-excitation processes including the ejection of a second electron called an Auger electron (see Figure 2.3). All elements have a unique set of core level electrons whose binding energies are spread out over a thousand electron volts (eV) or more. These are the electrons that are of interest for XPS analysis. By determining the binding energies of the photoelectrons, the

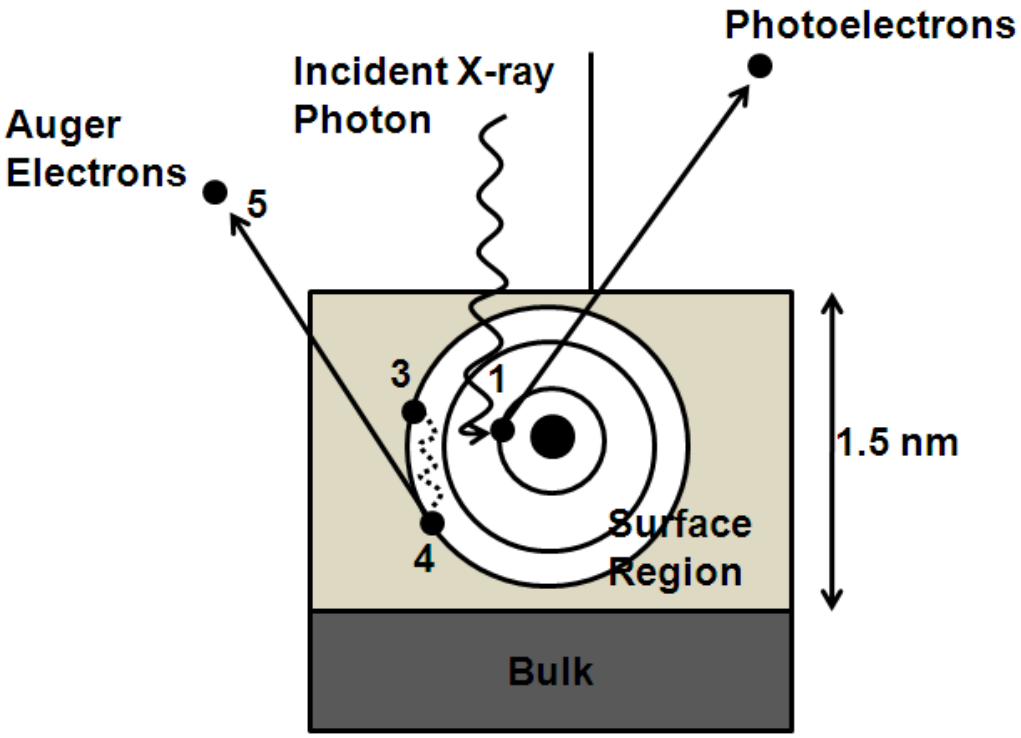

Figure 2.3- Sketch showing production of photoelectrons and auger electrons induced by X-ray bombardment. (1) Incident X-ray Photon, (2) Absorption of X-ray photon by core electron, (3) Ejection of core-level photoelectron, (4) Relaxation of higher shell electron into hole, (5) Internally recombined energy of relaxation, and (6) Ejection of Auger electron.

element of origin can be determined. In fact, small changes (a few eV) in the binding energy reflect differences in the chemical state (such as oxidation state) of the atom of origin and the number of photoelectrons produced reflects the quantity of the originating atoms in the excitation region.

The most commonly used X-ray lines for XPS analysis are the AlKα (1486.6 eV) and the MgKα (1253.6 eV). These X-rays have sufficient energy to excite the core level electrons and to penetrate deep into the bulk sample. Once the photoelectron has escaped from the surface without collision or energy loss, it has certain kinetic energy (*KE*) that can be related to the binding energy for the electron (E_B) which is characteristic for the electronic energy level of origin. By measuring the kinetic energy of the photoelectron, its binding energy can be determined as:

$$E_B = hz - KE - \phi_S \tag{2-1}$$

where *hz* is the energy of the incident X-ray photon and Φ_{SP} is the work function of the sample (the additional amount of energy required to move an electron from the Fermi level to the vacuum level).

2.2.6.2 Ion Scattering Spectroscopy (ISS)

In Ion Scattering Spectroscopy (ISS), a surface is bombarded with a beam of noble gas ions and the energies of the ions scattered under a fixed scattering angle are analyzed [105]. The masses of the collision partners determined the energy of the scattered ions. As shown in Figure 2.4, a monoenergetic, well-collimated beam of ions

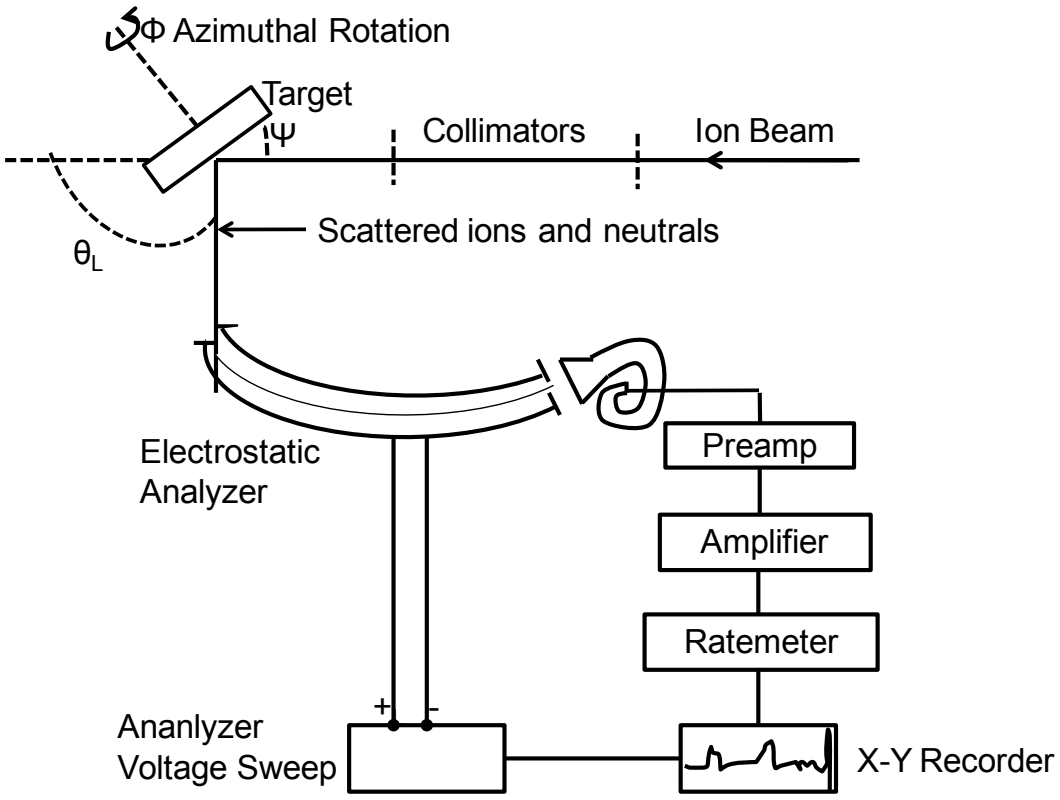

Figure 2.4- Schematic diagram of ion scattering experiment.

with energy of 0.1-10 keV strikes the target surface, and the energy distribution of ions scattered off at some particular angle is measured. The energy spectrum obtained provides information on the mass, or chemical identity and the number of surface atoms through the energy position and magnitude, respectively, of peaks in the spectrum.

These various kinds of information are obtained with varying degrees of accuracy and effort. Mass identification is quite straightforward; peaks for higher masses occur at higher energy in a predictable manner. Quantitative determination of the number of surface atoms is not so simple since the scattered ion yield depends on scattering cross-sections and neutralization efficiencies, neither of which are very well known at present [105]. However, quantitative analysis of foreign atoms at a surface can be achieved by calibration of the system against standards. Structure information, for example about atom locations and defects is derived from "shadowing" effects and multiple scattering. An outstanding feature of low-energy ion scattering is its fine degree of surface selectivity; the detected ions have scattered from only the first layer or two of atoms at the surface.

Low energy ion scattering spectroscopy (LEIS) (Kratos Analytical Inc., New York, USA) in conjunction with an X-ray photoelectron spectroscopy (XPS) Kratos AxisUltraDLD (Kratos Analytical Inc., New York, USA) was used to investigate the silica tetrahedral face and alumina octahedral face of kaolinite. LEIS involves directing a stream of charged particles known as ions ($^4He^+$) on a surface and making observations of the positions, velocities and energies of the ions that have interacted with the surface. The data thus collected could be used to deduce information about the material such as the relative positions of the atoms in a surface lattice and the elemental identity of those

atoms. LEIS spectrum of the silica face and alumina face of kaolinite particles was obtained with $^{4}He^{+}$ at 1000 Volts. XPS involves probing the sample surface with Al-Kα photon energy source. The X-ray photon interacts with the sample surface and ejects the photoelectron from the top few surface layers. The energy of the photoelectrons leaving the sample was determined using a concentric hemispherical analyzer, and this gives a spectrum with a series of photoelectron peaks. The binding energy of the peak areas are analyzed to determine the surface composition.

2.2.6.3 Chemical Bonding – FTIR Spectroscopy

Fourier transform infrared spectroscopy (FTIR) is a technique used to obtain an infrared spectrum of absorption, emission, photoconductivity or Raman scattering, and chemical bonding information of a solid, liquid or gas [106]. Infrared radiation covers the segment of the electromagnetic spectrum that lies between the visible light (about 0.8 μm) and microwave radiation (about 1000 μm).

There are several techniques available for infrared spectroscopic investigations such as diffuse reflectance, internal reflectance and attenuated total reflectance methods etc. bulk properties can be studied as well as the properties of surfaces, and with the use of infrared microscopy, even spectra of microscopic objects or details thereof can be recorded [106-111].

Infrared radiation can be described as electromagnetic wave of the length λ, the frequency ν or as commonly called within the infrared spectroscopy as the wavenumber $\bar{\nu}$. These quantities are related as follows:

$$\bar{\nu} = \frac{\nu}{c} = \frac{1}{\lambda} \tag{2-2}$$

where c is the velocity of light in a vacuum. The energy of infrared electromagnetic waves is directly proportional to the frequency (or wavenumber) as:

$$E = h\nu = \frac{hc}{\lambda} = hc\bar{\nu} \tag{2-3}$$

where *h* is Planck's constant. Most applications of vibrational spectroscopy are in the mid-IR spectral range (400-4000 cm^{-1}); however, soil related applications in the far-IR (10-400 cm^{-1}) and near-IR (4000-10000 cm^{-1}) regions are being reported more frequently.

Molecular vibrations occur at discrete energies in the IR region of the electromagnetic spectrum and are referred to as vibrational modes or as normal modes of vibration. These modes can be divided into two categories, internal vibration modes and phonon modes. Internal vibrational modes correspond to the periodic motion of atoms within a crystal or molecule. They are described by three types of motion:

i. Bond stretching

ii. Bending

iii. Torsional motions

Internal vibrational modes are usually found in the 400 to 4000 cm-1 range. Crystalline materials also have vibrational transitions in the 10 to 400 cm^{-1} region, termed phonon modes, resulting from the movement of one unit-cell or functional unit relative to another.

Fourier transforms infrared spectroscopy (FTIR) (Varian Inc., Palo Alto, CA, USA) was used to investigate the surface hydroxyl group on the alumina face and the inner-hydroxyl group between the silica tetrahedral sheet and alumina octahedral sheet of the kaolinite bilayer. The silica tetrahedral layer of kaolinite is composed of a hexagonal ring network of oxygen atoms on the 001 basal plane, whereas the alumina octahedral layer consist of a hexagonal ring network of hydroxyl atoms (OH) on the 00$\underline{1}$ basal plane. These hydroxyl atoms on the alumina octahedral face will be termed as inner surface hydroxyl atoms, which are hydrogen-bonded with the basal plane of oxygen atoms of the next layer. Other OH groups are located inside the bilayer, between the dioctahedral alumina sheet and tetrahedral silica sheet, pointing horizontally toward the center of the ditrigonal cavity. These OH groups will be called the inner hydroxyl group.

A similar technique as demonstrated by Gupta and Miller [72] was followed [72]to order kaolinite particles exposing the silica tetrahedral face and alumina octahedral face of kaolinite on a glass substrate and a fused alumina substrate, respectively. Briefly, 20 µl of kaolinite suspension (5%) at pH 5.0 prepared in high purity Milli-Q water (Millipore Inc.) was air-dried overnight on two cleaned glass substrates (SC1 cleaned) in a petri-dish cover. In order to achieve good coverage of kaolinite particles on the glass substrate, kaolinite suspension was redeposited two times (20 µl each times) on the previously deposited kaolinite particles on the glass substrate. In this way, a very good film of kaolinite particles was obtained on the glass substrate (visual observation). AFM imaging conducted on one such ordered kaolinite particle substrate showed a root-mean-square roughness of about 5 nm. It should be expected that the kaolinite particles deposited on the glass substrate should expose their silica face. In the second experiment,

a suspension of the kaolinite particles (5% by weight at pH 5.0) was deposited on two cleaned fused alumina substrates (Piranha cleaned). The details of alumina substrate cleaning are described elsewhere [112]. It should be expected that the kaolinite particles deposited on the fused alumina substrate should expose their alumina face.

2.3. Results and Discussion

2.3.1 Mineralogy and Elemental Analysis

Kaolinite was determined as the primary mineral in the powder sample using XRD (see Figure 2.5). Other minerals present in minor amounts are quartz and anatase. The main intensity peak showed c-spacing of 7.15 Å which is indicative of the 001 basal plane of kaolinite. A small peak at 2θ of 25.5^0 with c-spacing of 3.49 Å is indicative of anatase mineral.

As expected, the elemental analysis of the kaolinite particles using EDS showed that silicon, aluminum and oxygen are the main elements of the crystal structure, whereas potassium, calcium and iron are present as interlayer cations (see Figure 2.6). The ratio of silicon to aluminum is nearly 1, which matches well with the theoretical ratio of silicon to aluminum (see Table 2.1). The carbon peak in the EDS spectra originates from the background carbon tape.

2.3.2 Structural Formula

The chemical composition of kaolinite as determined using XRF is shown in Table 2.1. As shown, the experimental and theoretical compositions are in reasonable

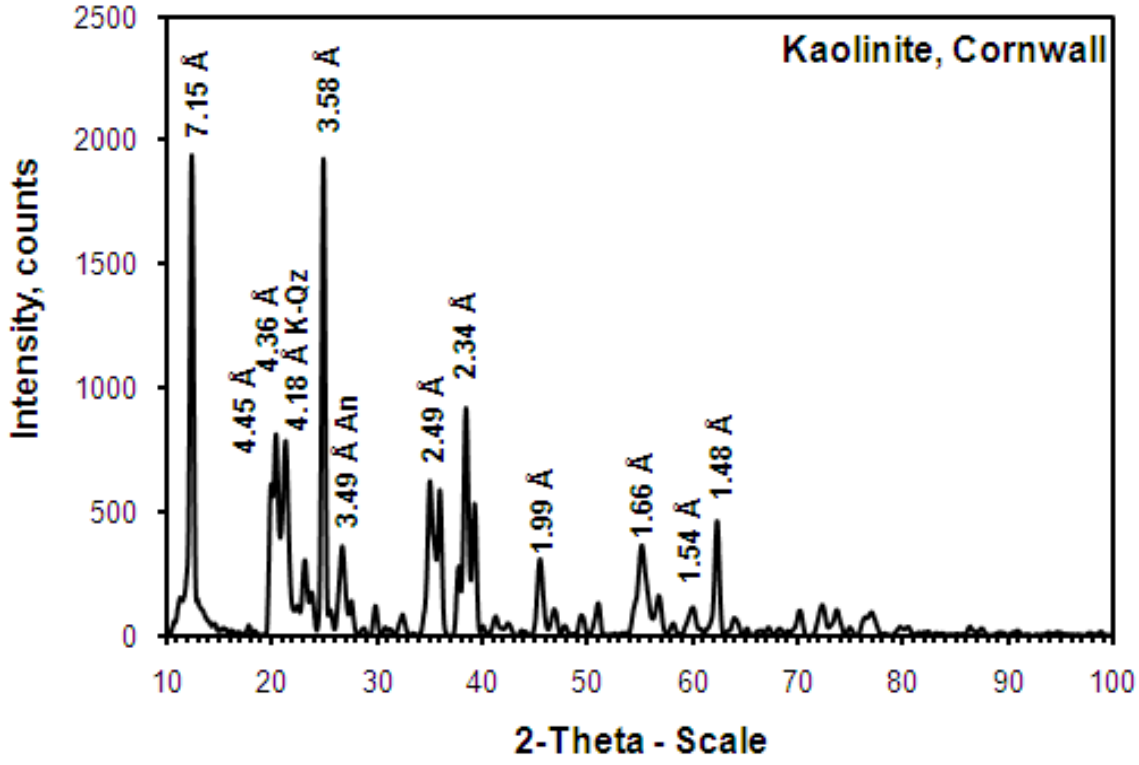

Figure 2.5- XRD spectra of kaolinite showing the mineralogy of kaolinite.

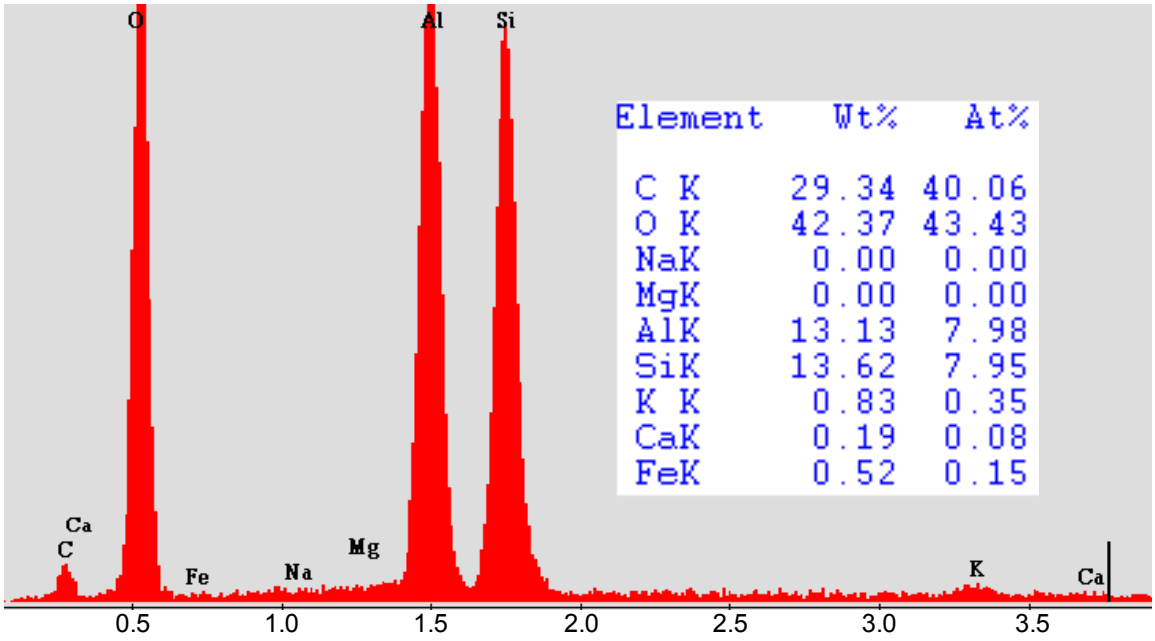

Figure 2.6- EDS spectra of kaolinite showing the elemental composition of kaolinite.

Table 2.1- Chemical composition of kaolinite

Elemental Oxides	Weight (%)	
	Experimental	Theoretical
SiO_2	47.00	46.30
Al_2O_3	41.00	39.80
Fe_2O_3	0.26	
TiO_2	0.14	
CaO	0.06	
MgO	0.08	
K_2O	0.18	
Na_2O	0.03	
H_2O	11.60	13.90
	100.35	

agreement. The kaolinite also contains minor amounts of Fe, Ca, Mg, K and Na in its crystal structure, as well as small inclusions of TiO_2 [113]. The water is present as structural water [113].

Utilizing the chemical composition of kaolinite, the structural formula of kaolinite was calculated based on the ideal hydroxyl composition and a total of 28 negative charges in the crystal structure [113], as shown in Table 2.2. It is restated here that the water is present as structural water, whereas TiO_2 is present as impurities. This amount should be deducted from the total amount, as shown in column 3 of Table 2.2. The structural formula of the kaolinite is then given as:

$$(Si_{3.94}Al_{0.06})^{IV}(Al_{3.99}Fe_{0.01})^{VI}O_{10}(OH)_8.Fe_{0.01}Ca_{0.01}Mg_{0.01}K_{0.02}Na_{0.005}$$

Only 0.06 equivalents of the aluminum from the octahedral layer contribute to the isomorphic substitution of Si^{4+} for Al^{3+} in the silica tetrahedral layer. This is in excellent agreement for kaolinite from Nigata, Japan which also showed 0.06 equivalents of substitution of Si^{4+} for Al^{3+} in the silica tetrahedral layer [17]. The kaolinite from Georgia, USA also showed good agreement which showed 0.05 equivalents of substitution of Si^{4+} by Al^{3+} in the silica tetrahedral layer [113]. The deficiency of charge in the alumina octahedral layer was neutralized using Fe^{2+}/Fe^{3+} ions. All other ions such as Fe, Ca, Mg, K and Na exist as interlayer cations in between kaolinite layers.

This minor amount of substitution of Si^{4+} for Al^{3+} also corresponds well with the experimental cation exchange capacity (CEC) which showed a low CEC of well ordered kaolinite from Pittong ranges (Victoria, Australia) from 0.028 to 0.050 mol/kg, whereas

Table 2.2- Charge calculation of kaolinite based on a total of 28 negative charge in the crystal structure*

Elemental Oxides	Weight %	Normalized Wt. %	Molecular Wt.	No. of Cations in Oxide	Cation Valence	Charge equivalents	Proportionality Factor, R	Atoms per Unit Cell
SiO_2	47	53.04	60.09	1	4	3.5308	4.4608	3.94
Al_2O_3	41	46.27	101.96	2	3	2.7228	4.4608	4.05
Fe_2O_3	0.26	0.29	159.7	2	3	0.0110	4.4608	0.02
TiO_2	0.14							
CaO	0.06	0.07	56.08	1	2	0.0024	4.4608	0.01
MgO	0.08	0.09	40.31	1	2	0.0045	4.4608	0.01
K_2O	0.18	0.20	94.2	2	1	0.0043	4.4608	0.02
Na_2O	0.03	0.03	61.98	2	1	0.0011	4.4608	0.005
H_2O	11.6							
	100.35	100.00				6.2770		

*Column 3 – Normalize the elemental oxide composition of the kaolinite to 100% after deduction the TiO_2 and H_2O amount;
Column 7 – Divide the percentage concentration of each oxide by its molecular weight and multiply by the total number of metal atoms and the normal charge of the metal in the oxide to obtain the charge equivalent;
Column 8 – Calculate the proportionality factor (R) by dividing the number of assumed fixed negative charges in the structure of the mineral with the sum of charge equivalents;
Column 9 – Calculate the occupancy of atoms per unit cell by multiplying each charge equivalent with the proportionality factor (R) and dividing by the valency of the cation

the CEC of poorly ordered kaolinite of secondary origin from Swan Bay ranges (New South Wales, Australia) from 0.16 to 0.34 mol/kg [114].

BET specific surface area of kaolinite was determined as 8.8 m^2/g using N_2 gas adsorption isotherm. Cases *et al.* [74] obtained similar results for the specific surface area of kaolinites from St. Austell, Cornwall, UK and Georgia as 11.4 and 10.9 m^2/g, respectively. Huertas *et al.* [37] also reported a similar specific surface area of 8.16 m^2/g for well crystallized Georgia kaolinite.

2.3.3 Shape, Size and Aspect Ratio

The SEM and AFM image of kaolinite particles on a mica substrate are shown in Figure 2.7, confirming the pseudo-hexagonal shaped plate like particles. The size distribution of the kaolinite particles as obtained from SEM image analysis is shown in Figure 2.8. The aspect ratio (diameter to thickness ratio) obtained from AFM image analysis is also shown in Figure 2.8. The circular diameter of the kaolinite particles lies between 0.03 and 3.54 μm. Only 3.5% (by number) of the particles are greater than 1.0 μm. The median diameter of the kaolinite particles was determined to be 600 nm. This is in good agreement from both SEM and AFM image analysis for at least 150 particles. The kaolinite particles thickness varied from 1.75–215 nm as determined from the AFM image analysis. The median thickness of the particle population was determined to be 11.2 nm. Each bilayer of kaolinite particles is about 0.72 nm and therefore, it is estimated that the average kaolinite particle consist of 15 bilayers. The aspect ratio of the kaolinite particles varied from 9–165 with median value of 45.

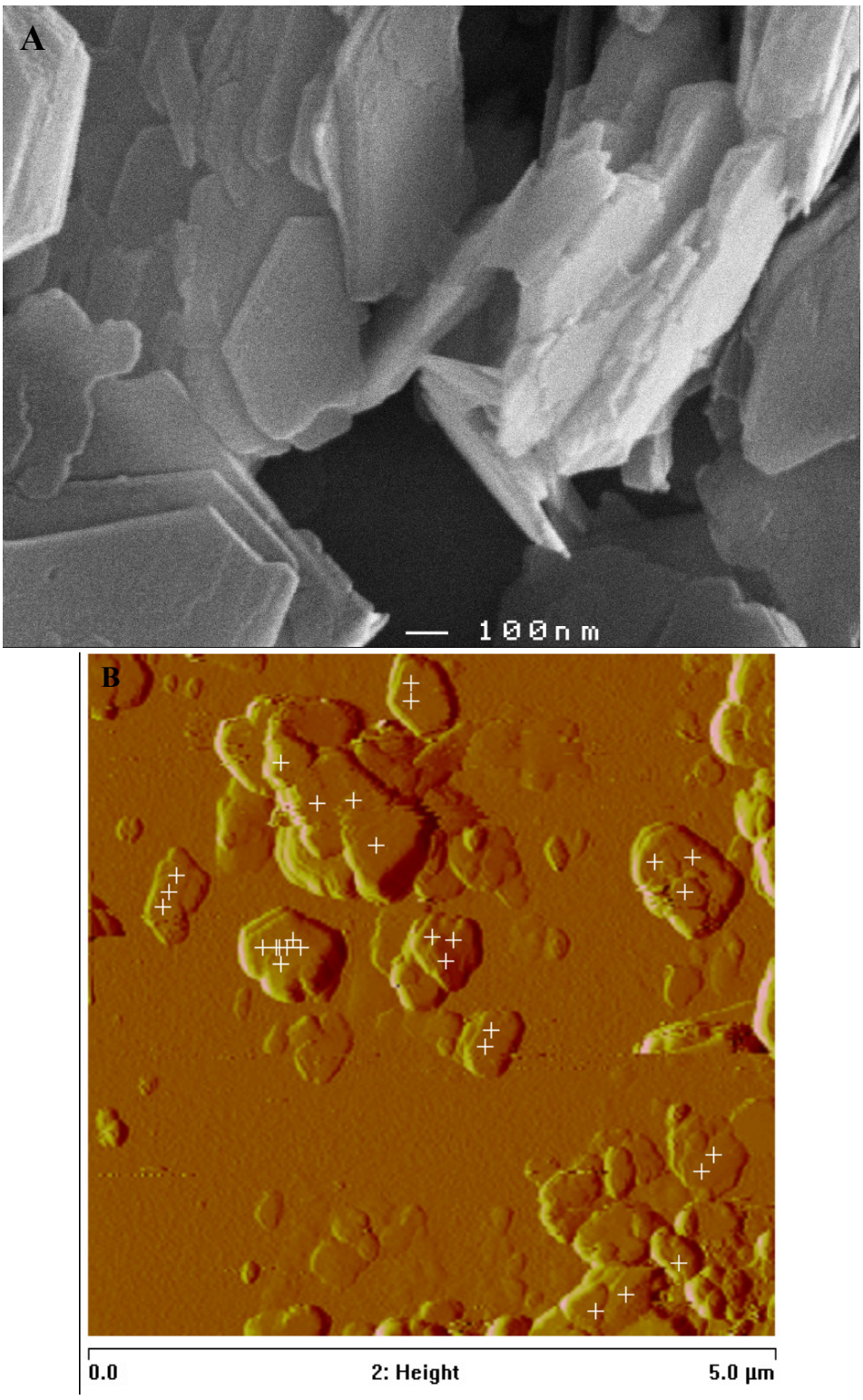

Figure 2.7- (A) SEM (B) AFM images of kaolinite particles showing the pseudo-hexagonal shaped plate-like particles.

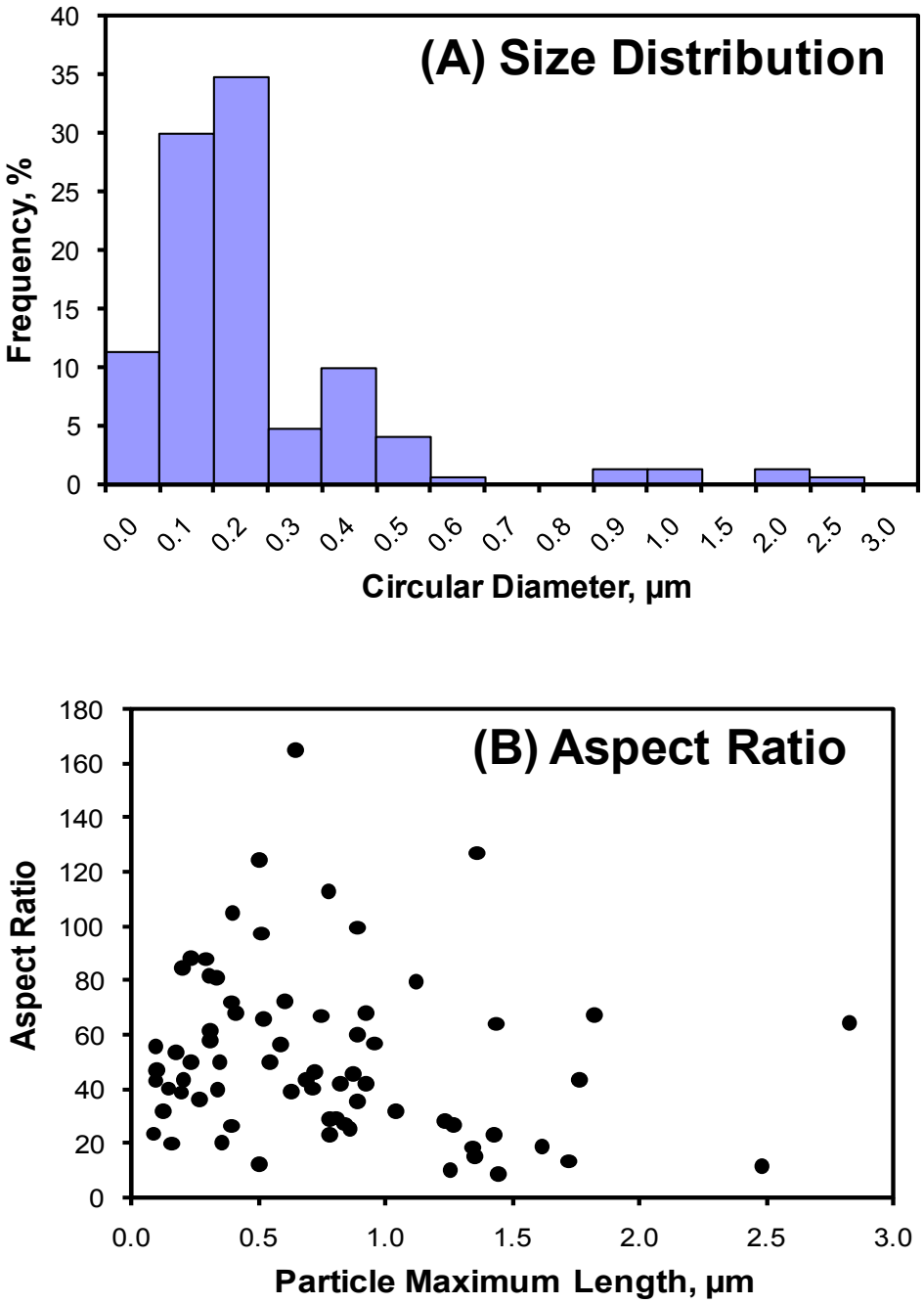

Figure 2.8- (a) Size distribution, and (b) aspect ratio of St. Austell, Cornwall kaolinite particles using equivalent circle diameter based on SEM and AFM image analysis.

In contrast to these results, Zbik and Smart [61] determined median aspect ratio for Georgia kaolinite of 3.4 and 5.3 using SEM and AFM techniques, respectively. For a kaolinite from North Queensland, the median aspect ratio was determined as 3.9 and 6.8 using SEM and AFM techniques, respectively [61]. It should be noted that the Georgia kaolinite is found in naturally thicker booklets and therefore, a lower aspect ratio when compared to the Cornwall kaolinite used in this dissertation research.

2.3.4 Surface Spectroscopy of Kaolinite

Figure 2.9 shows the ISS spectra of the silica face and alumina face of kaolinite. The ISS spectra showed a sharp peak for oxygen, a broad peak for silicon and aluminum, a small peak for potassium and a copper peak. The copper peak originates from the background copper strip used to attach the sample. It should be noted that due to poor signal-to-noise ratio the spot size of the ions on the substrate was increased. Therefore, some signal was collected from the background copper strip.

The broad peak consists of both aluminum and silicon elements as the broad peak coincided with the calculated silicon and aluminum atomic peak positions at kinetic energies of 578 eV and 597 eV, respectively. These peak positions are close to each other due to the similar mass of silicon atoms (28.08 a.m.u.) and the aluminum atoms (26.98 a.m.u.). A deconvolution algorithm was applied to separate the two peaks at kinetic energies of 578 eV and 597 eV representing the aluminum and silicon elements, respectively. The area under the two peaks was integrated following Gaussian distribution, and the ratio of areas representing aluminum and silicon peaks are plotted as function of time, as shown in Figure 2.10.

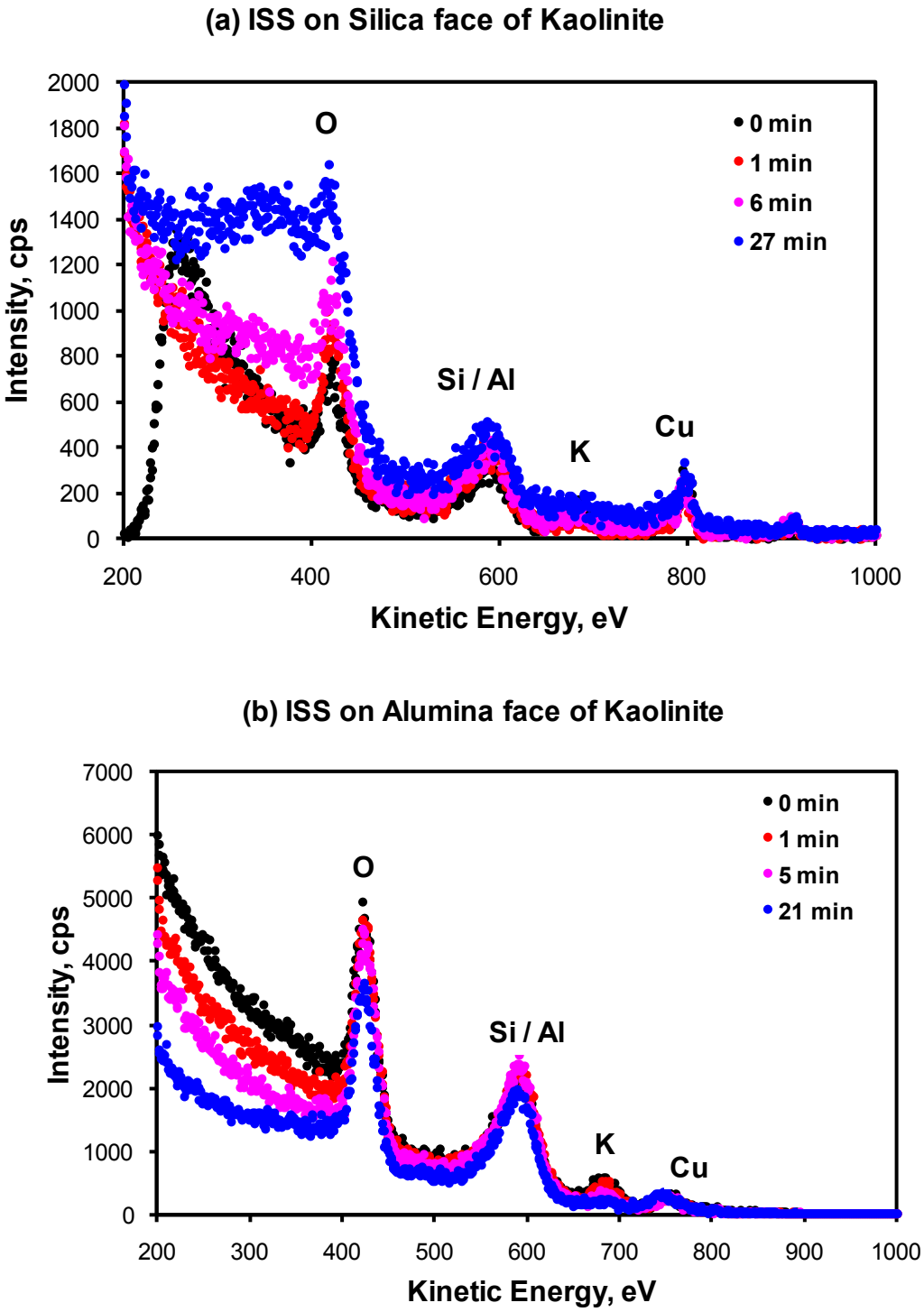

Figure 2.9- ISS spectra on (a) silica face and (b) alumina face of kaolinite particles for various bombarding times.

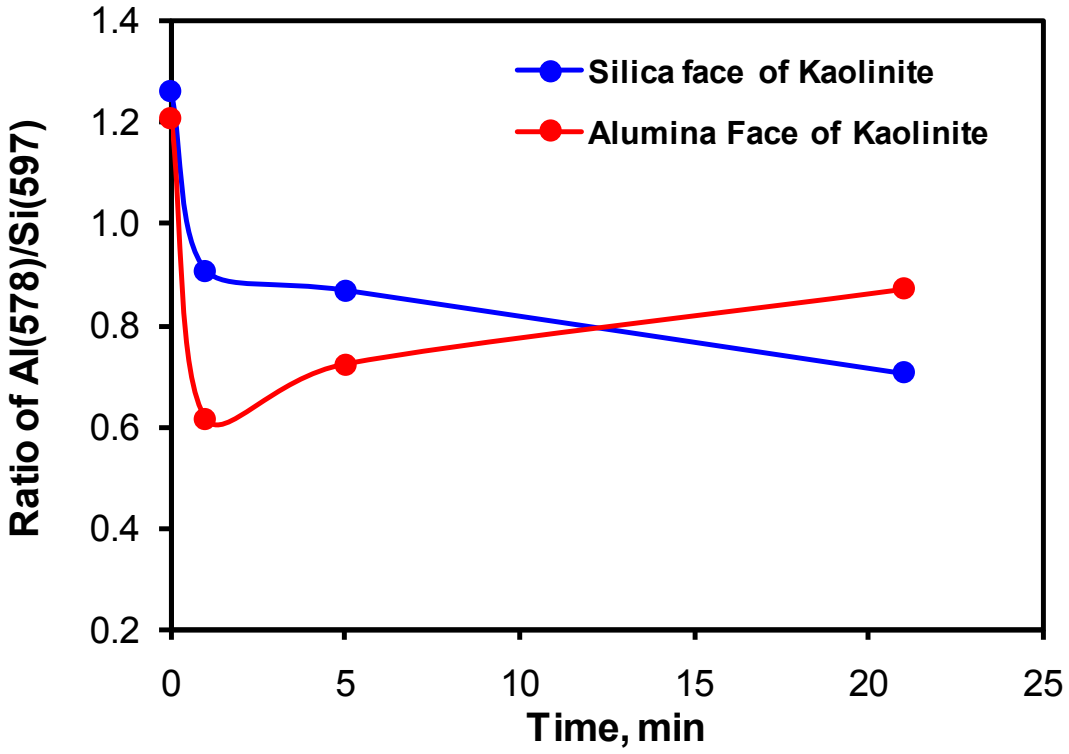

Figure 2.10- Ratio of aluminum to silicon peak areas from both silica and alumina face of kaolinite as a function of bombarding time.

It is expected that the ratio of aluminum to silicon should increase with bombarding of ions with time on the silica face, and decrease on the alumina face of kaolinite. This may be due to the removal of silicon and aluminum atoms from the silica face and the alumina face of kaolinite, respectively, by the continuous bombarding of ISS beam ($^4He^+$ ions) on the respective faces of kaolinite. In contrast to our expectations, the ratio of Al/Si decreased on the silica face, and increased on the alumina face of kaolinite with time, as shown in the Figure 2.10. The reason for such behavior of decreasing the aluminum to silicon ratio from the silica face and increasing the aluminum to silicon ratio from the alumina face is not clear, although some concerns were raised whether the peak positions for the silicon and aluminum atoms were correctly estimated. The issue of silicon and aluminum atoms peak position could not be resolved at this moment and further study is warranted in order to identify the silica face and alumina face of kaolinite using LEIS.

The FTIR spectra obtained from the silica face and alumina face of kaolinite are shown in Figure 2.11. The OH-vibration peaks were identified on both the silica face and alumina face of kaolinite. The band observed at 3620 cm^{-1} corresponds to inner OH stretching vibrations, as shown in Figure 2.11. The band observed at 3691 cm^{-1} corresponds to the in-phase motion of the three inner-surface OH group, whereas the band at 3668 cm^{-1} and 3651 cm^{-1} correspond to the out-of-phase motion of the inner-surface OH groups. These results are in excellent agreement with the band positions of inner-surface OH groups and inner OH groups published in the literature [53-55, 73, 115]. Interestingly, FTIR spectra for the silica face showed greater surface sensitivity (inner OH and inner-surface OH peaks are sharper and longer) when compared to the

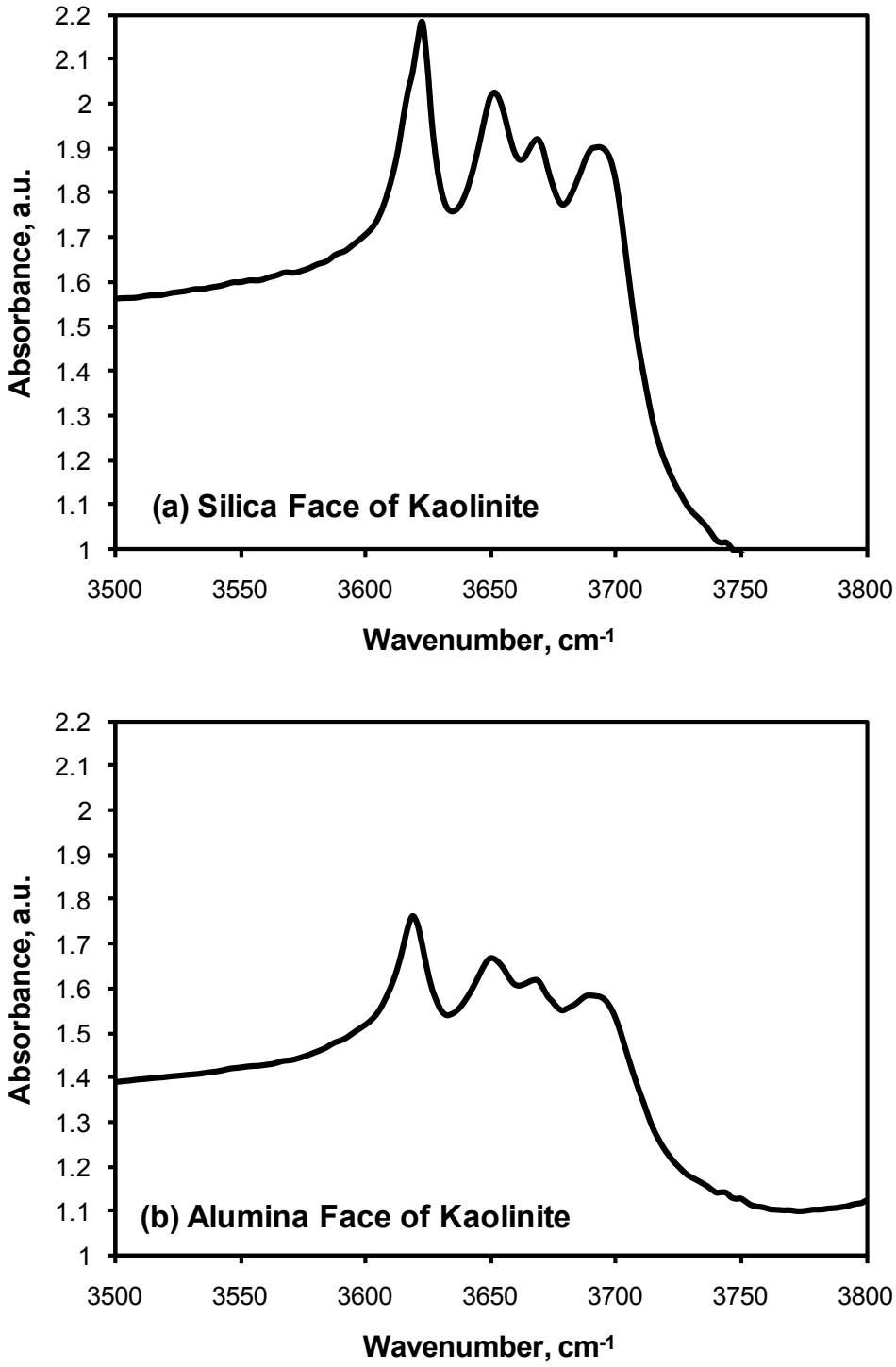

Figure 2.11- The experimental infra red spectrum of kaolinite obtained from (a) silica face, and (b) alumina face.

alumina face of kaolinite. This high surface sensitivity from the silica face of kaolinite was not reported before, and should be further investigated with highly surface sensitive techniques such as vibrational frequency spectrometry.

FTIR was compromised by greater penetration depth (~ 100 nm), and signals were collected from both the silica and alumina faces of kaolinite particles. However, it would have been ideal to gather information from the first layer of the surface only.

Recently, Burdukova [56] used time-of-flight secondary ions mass spectroscopy (ToF SIMS) to analyze the talc surface. However, these results were averaged over a few trilayers of the talc surface. The advancement of surface analysis technique seems promising to gather information about the kaolinite faces as well as other clay surfaces. Further research is warranted to improve our understanding and establish the surface chemistry features of clay surfaces, particularly kaolinite.

2.4. Summary

A pool of advanced analytical instruments such as BET, XRF, XRD, EDS, SEM, AFM, LEIS and FTIR was used for kaolinite particle characterization. The surface area of the particles was estimated using BET, whereas XRD and EDS were used to identify the mineralogy and elemental composition of kaolinite. Based on the elemental composition, the structural formula of kaolinite was determined. Only 0.05 equivalents of aluminum from the octahedral layer contributed to the silica tetrahedral layer. SEM and AFM confirmed the pseudo-hexagonal shape of the platy shaped kaolinite particles. The mean diameter and thickness of kaolinite were determined as 600 nm and 11.2 nm. LEIS and FTIR was used to obtain the spectra from the silica and alumina faces of kaolinite in

order to distinguish them from each other. The ISS spectra showed a combined broad peak for silicon and aluminum atoms, which could not be resolved in the present analysis, and further research is warranted to better understand the surface properties of the kaolinite faces.

CHAPTER 3

SURFACE FORCE MEASUREMENTS AT THE BASAL PLANES OF ORDERED KAOLINITE PARTICLES

An experimental procedure is presented to order kaolinite particles on substrates for interrogation of the two basal plane surfaces by atomic force microscopy. Surface force measurements were performed between a silicon nitride tip and each of the two kaolinite faces (silica tetrahedral face and alumina octahedral face) in 1 mM KCl solution at pH 4, 5, 6, 8 and 10, using atomic force microscopy. The colloidal force measurements reveal that the silica tetrahedral face of kaolinite is negatively charged at pH > 4, whereas the alumina octahedral face of kaolinite is positively charged at pH < 6, and negatively charged at pH > 8. Such measurements have not been reported previously and the results suggest that the iso-electric point of the silica tetrahedral face is at pH < 4, and that the iso-electric point of the alumina octahedral face lies between pH 6 and 8. These results contradict the generally accepted view that basal plane surfaces of kaolinite carry a permanent negative charge due to minor substitution of Al^{3+} for Si^{4+} in the silica tetrahedral layer, and suggest some surface charge dependency of the two faces with respect to solution pH. With this new information, it may be possible to further explain

the electrokinetic behavior of kaolinite particles, and their interactions in aqueous suspensions.

3.1 Introduction

The interaction of kaolinite [$Al_2Si_2O_5(OH)_4$] particles is of particular importance in widespread applications, e.g., in ceramics, in the manufacture of paper (as a coating, pigment and filler), in inks and paints (as an extender), and as an additive in the production of rubber and polymers [53, 63, 116]. Newer applications of kaolinite include its use as a raw material in the production of fiberglass, calcined kaolins, cosmetics and pharmaceuticals [116]. Kaolinite naturally exists as micron-to-nanosized, pseudo-hexagonal, platy-shaped, thin particles. The behavior of these nanosized kaolinite particles in suspensions, pastes and composite materials is controlled by surface chemistry features. Analysis of the surface chemistry features, such as electrokinetic phenomena, is complicated by the anisotropic, platy structure of the particles which manifests itself in edge surfaces and face surfaces. Even more so, the mineral structure suggests that there should be two types of surface faces defined by the 001 and the 00$\underline{1}$ basal planes. In this way, one face should be described as a silica tetrahedral layer and the other face should be described as an aluminum hydroxide (alumina) octahedral layer, as shown in Figure 1.1.

It is believed that the basal planes of kaolinite carry a permanent negative charge due to isomorphous substitution of Al^{3+} for Si^{4+} in the silica tetrahedral, and Mg^{2+} for Al^{3+} in the alumina octahedral layer, whereas the edge surface carries a positive or negative charge depending on the pH of the system. Therefore, it is commonly assumed

that the basal planes do not show a surface charge dependency with varying pH. However, this assumption has never been verified due to the difficulty in isolating the two faces of kaolinite (silica tetrahedral and alumina octahedral faces), and the lack of instrumentation to investigate the two faces when dealing with nanosized particles.

Limited research has been reported on the experimental characterization of these face surfaces, if the faces can even be distinguished from one another for that matter [15]. Frequently, the surface potential and/or surface charge of the kaolinite particles as measured by electrophoresis are reported in the literature [3, 4, 15, 52, 117]. It is evident, however, that the electrophoretic measurement does not take into consideration the particle shape and the structural anisotropic characteristics. In fact, it is not exactly clear what the measured electrophoretic mobility of kaolinite represents.

A few studies have reported the averaged FTIR spectra of both faces of kaolinite [53-55, 115]. Recent development of advanced analytical techniques (XPS - X-ray photoelectron spectroscopy, LEISS - Low energy ion scattering spectroscopy, and ToF-SIMS - Time of flight-secondary ions mass spectroscopy) seem promising to facilitate investigation of the two faces of kaolinite provided the particles can be oriented, and that the instrumentation is sufficiently surface sensitive to collect signals from just the very first layer of a face surface. For example, a recent study attempted ToF-SIMS analysis to study the talc surface [56]. However, these results were averaged over a few layers of talc. Recently, many researchers have used scanning electron microscopy (SEM) [58, 59], transmission electron microscopy (TEM) [60, 75] and atomic force microscopy (AFM) [59, 62, 76] as imaging tools to characterize particle shape and morphology.

It is now well established that AFM instrumentation can also be used to measure surface forces between the cantilever probe/tip and a selected substrate. In this regard, an experimental procedure has been developed to organize a set of well ordered, nanosized kaolinite particles for in-situ AFM surface force measurements, following the approach of Drelich *et al*. [118] where they have preferentially deposited silica nanoparticles on an alumina substrate, and alumina nanoparticles on a silica substrate for AFM investigation. The significance of these AFM surface force measurements is that the electrokinetic characteristics of the face surfaces of nanosized kaolinite particles can be described following earlier research in which the cantilever probe/tip is used as a reference to establish the electrokinetic features of a flat surface. Such measurements have been reported for alumina [119-122] and for fluorite [123].

The objective of this chapter is two folds, (1) to describe an experimental procedure to order kaolinite particles so that a selected face is exposed for in-situ examination, and (2) to characterize the two faces of kaolinite (the silica face and the alumina face) by surface force measurements using AFM. To order kaolinite particles with the silica face exposed, a negatively charged glass substrate is used so that the alumina face might attach to the glass substrate, as shown in Figure 3.1. In contrast, to expose the alumina face of the kaolinite particles, a positively charged fused alumina substrate is used so that the silica face will attach to the fused alumina substrate, as shown in Figure 3.1.

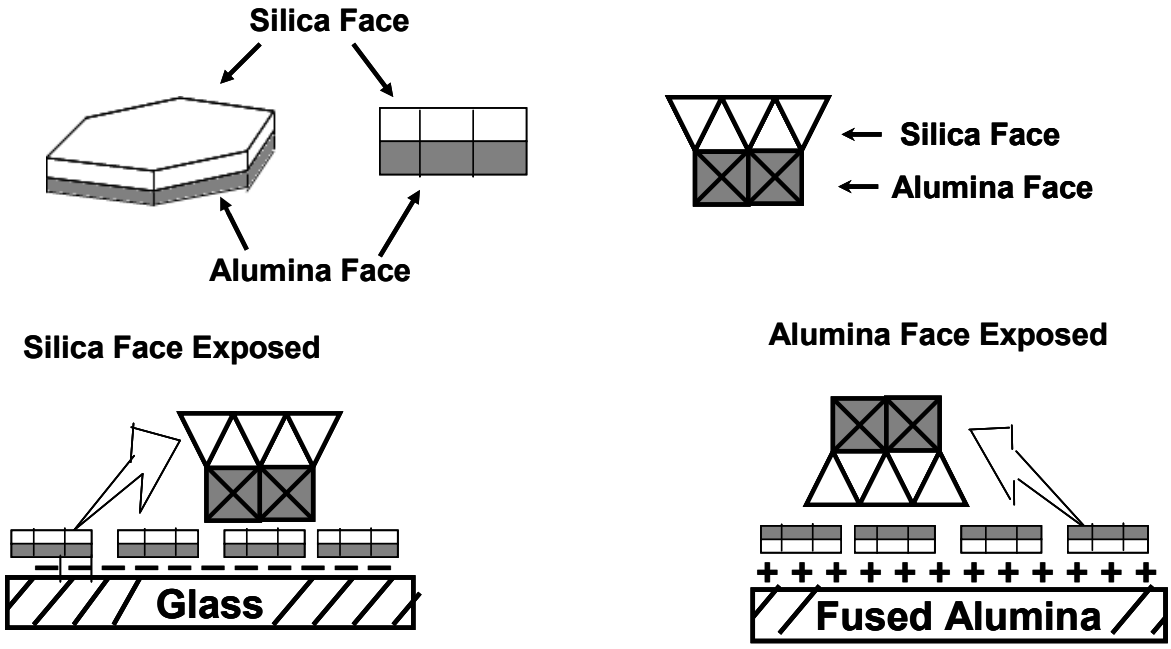

Figure 3.1- Schematic representation for the organization and ordering of kaolinite particles.

3.2 Materials and Methods

3.2.1 Sample Preparation

A clean English kaolin (Imerys Inc., UK) was obtained from the St. Austell area in Cornwall, UK. The sample was cleaned with water only using elutriation to achieve classification at a size of less than 2 μm. No other chemical treatment was done. Further details about the kaolinite extraction and preparation are given in the literature [124]. The kaolinite was used as-received in this research. The kaolinite suspension (1000 ppm) was prepared in high purity Milli-Q water (Millipore Inc.). The resistivity of the water was above 18 MΩ-cm in all experiments. Potassium chloride (1 mM solution) was used as background electrolyte for surface force measurements. The pH was adjusted to its desired value using 0.1 M HCl or 0.1 M KOH solutions. All chemicals used were of ACS grade.

XRD analysis conducted on the kaolinite sample confirmed that the kaolinite is the dominant mineral phase. EDAX analysis of the kaolinite sample showed nearly 1:1 atomic distribution of aluminum (7.98%) and silicon (7.95%) with trace amounts of potassium (0.35%), calcium (0.08%) and iron (0.15%).

3.2.2 Substrate Preparation

Two substrates – a microscopic glass slide (Fisher Scientific Inc.) and a fused alumina substrate (Red Optronics, Mountain View, CA), were used to order the kaolinite particles. Two cut pieces of microscopic glass slide (10 x 10 x 0.5 mm) were cleaned following SC1 procedure [125]. Briefly, the glass piece was cleaned in 5:1:1 mix of H_2O:NH_4OH:H_2O_2 solution, at 80^{o}C for 20 minutes, followed by rinsing with a copious

amount of high purity Milli-Q water, and dried with ultra high purity N_2 gas. On one glass substrate, a drop of kaolinite suspension at pH of 7.50 was air-dried overnight in a petri-dish cover. A second glass substrate was prepared in the same way without kaolinite and used as reference (referred to as Glass-Substrate) for surface force measurements. Two fused alumina substrates were prepared by cleaning in 10% micro-90 solution at 85^0C for 3 hours, followed by rinsing with a copious amount of high purity Milli-Q water. The alumina substrates were sonicated in 1% NaOH solution for 10 minutes to remove excess surfactant, rinsed with a copious amount of Milli-Q water, and finally blown dry with ultra high purity N_2 gas. A few drops of kaolinite suspension (1000 ppm) at pH of 5 were air-dried overnight on the one alumina substrate in a petri dish cover, whereas the second alumina substrate was used as reference (referred to as Fused Alumina-Substrate) for the surface force measurements. All substrates were attached to a standard sample puck for the surface force measurement using double-sided tape. The Fused Alumina-Substrate was cleaned in ultra-violet light cleaner (Bioforce Nanoscience Inc., IA) for 10 minutes just before surface force measurements. Kaolinite particles attached to glass and alumina substrates were each sonicated for 1 minute in Milli-Q water to remove loosely adhered kaolinite particles, washed with Mill-Q water, and gently blown with N_2 gas before AFM surface force measurements.

3.2.3 Atomic Force Microscopy

A picoforce AFM with Nanoscope V controller (Veeco Instruments Inc., Santa Barbara, CA) was used with a PF-type scanner designed for picoforce measurements. Triangular beam silicon nitride (Si_3N_4) cantilevers (Veeco Instruments Inc., Santa

Barbara, CA) having pyramid-shaped tips with spring constants of about 0.15 N/m were used. The spring constant was determined using the thermal tuning method provided in Nanoscope v 7.20 software. The spring constants were determined after all the force measurements were made. Prior to force measurements, the tip curvature and the conical angle of the pyramid-shaped tip (Figure 3.2) were determined from the images captured with a field emission scanning electron microscope (FEI, Hillsboro, Oregon). SEM images were taken after the cantilever was glued with a carbon tape on the tilted specimen stage to capture the side view of the top-portion of the tip, as shown in Figure 3.2. The tip apex curvature was determined by fitting two circles to the curvature of the tip. The radii of the two circles were determined, and an average value of the two radii representing the tip curvature was calculated.

The force measurements were made in 1 mM KCl solution at pH 4, 5, 6, 8 and 10 using the picoforce AFM equipped with a fluid cell. First, an image of the substrate with or without particles was obtained, and then using the point and shoot feature of the Nanoscope software, the surface forces of particles and substrates were measured. The contact mode of operation was used to obtain images of the surface. The raw data (deflection in volts versus distance in nanometers) were then corrected for the baseline (zero force, i.e., when the silicon nitride tip is far away from the substrate) and constant compliance to convert into force versus separation distance curves [126]. At least 50 force measurements were made on glass and alumina substrates at 10 random locations with 5 repetitions at any given location. More than 75 surface force measurements were made on 15 different kaolinite particles attached to each glass and alumina substrates. The force measurements were made on kaolinite particles which are at least 2-3 times

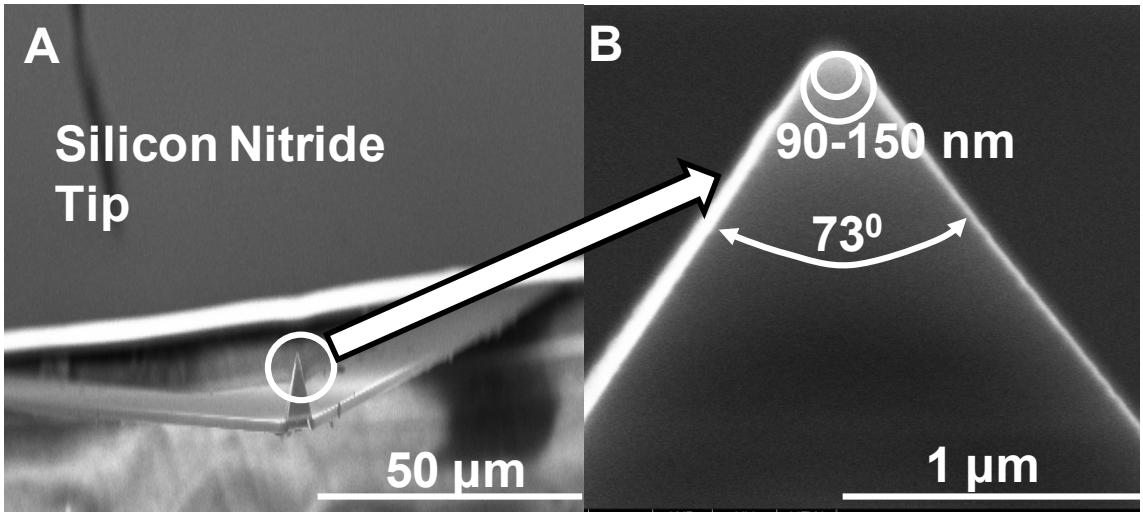

Figure 3.2- SEM images of silicon nitride tip (A) oblique view at low magnification, (B) plan view of pyramidal tip at high magnification (indicated by arrow).

larger than the cantilever tip to minimize the influence of the substrate. All the force measurements were performed at a scan rate of 1 Hz and captured at a resolution of 512 points/measurement. Approach force curves (when the cantilever is approaching the substrate or the particles) were analyzed to determine the colloidal interaction forces between the silicon nitride tip and the substrate. Maximum repulsive forces were recorded just before the silicon nitride tip jumps-in contact to the substrate. The interaction range between the silicon nitride tip and the substrate were determined when the repulsive or attractive forces (from their maximum value) were within the 10% of the zero force. Zero force was determined from the average of 100 force data points when the cantilever is far from the substrate.

3.2.4 DLVO (Derjaguin-Landau-Verwey-Overbeek) Model

The cantilevers used for the surface force measurements have pyramidal shaped silicon nitride tips. The shape of the tips can be reasonably approximated as conical with a spherical cap at its apex (see Figure 3.3). DLVO theory accounts for electrostatic and van der Walls (vdW) forces that may be of significance between the silicon nitride tip and the substrate or kaolinite particle faces. The derivation of DLVO theory for a pyramidal-shaped tip and a flat substrate is given in the literature [127], and only the final equations are listed below:

$$F^{DLVO} = F^{Electrostatic} + F^{vdW} \tag{3-1}$$

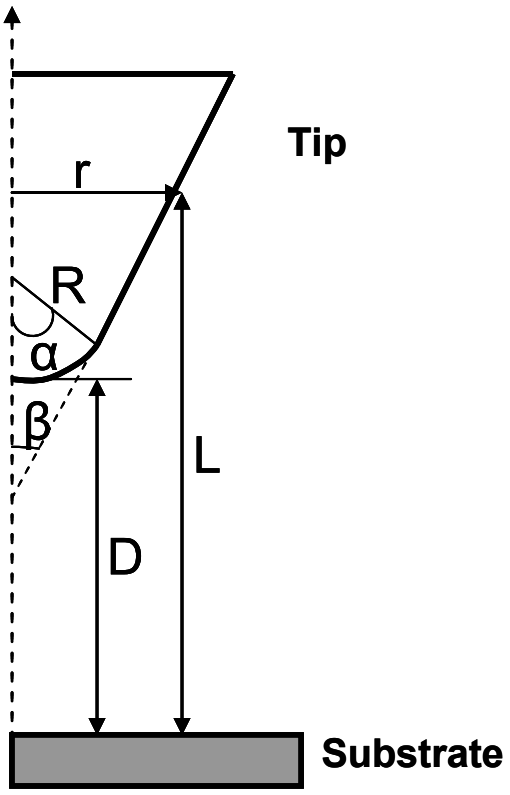

Figure 3.3- Diagram showing the conical end portion of the silicon nitride tip with a spherical cap. Angles α and β are the geometrical angle of the spherical cap at the tip apex and conical tip, respectively, with α + β = 900. D is the separation distance from the tip end to the substrate. L is the distance between a differential surface section of the tip and the substrate, r is the radius of the tip at a given vertical position, R is the radius of the spherical cap at the tip apex.

van der Waals force:

$$F^{vdW} = \frac{A}{6}\left[\frac{(R+D)-2L_1}{L_1^2} - \frac{R-D}{D^2}\right] - \frac{A}{3\tan^2\alpha}\left[\frac{1.0}{L_1} + \frac{(R\sin\alpha\tan\alpha)-D-R(1-\cos\alpha)}{L_1^2}\right] \quad (3\text{-}2)$$

Electrostatic force (constant surface potential case):

$$F^{Electrostatic} = 4\pi\varepsilon_0\varepsilon\psi_T\psi_S\left(a_0e^{-\kappa D} - a_1e^{-\kappa L_1}\right) - 2\pi\varepsilon_0\varepsilon\left(\psi_T^2+\psi_S^2\right)\left(a_2e^{-2\kappa D} - a_3e^{-2\kappa L_1}\right) + \frac{4\pi\varepsilon_0\varepsilon\kappa}{\tan\alpha}\left[b_1\psi_T\psi_S e^{-\kappa L_1} - b_2\frac{(\psi_T^2+\psi_S^2)}{2}e^{-2\kappa L_1}\right] \quad (3\text{-}3)$$

where

$$b_1 = \left[R\sin\alpha - \frac{D+R(1-\cos\alpha)}{\tan\alpha}\right] + \frac{1}{\tan\alpha}\left(L_1 + \frac{1}{\kappa}\right) \quad (3\text{-}4)$$

$$b_2 = \left[R\sin\alpha - \frac{D+R(1-\cos\alpha)}{\tan\alpha}\right] + \frac{1}{\tan\alpha}\left(L_1 + \frac{1}{2\kappa}\right) \quad (3\text{-}5)$$

$$L_1 = D + R\left(1-\cos\alpha\right), a_0 = \kappa R - 1, a_1 = \kappa R\cos\alpha - 1, a_2 = a_0 + 0.5, a_3 = a_1 + 0.5 \quad (3\text{-}6)$$

α and β are the geometrical angles of the spherical cap at the tip apex and the conical tip, respectively, with $\alpha + \beta = 90^0$. D is the separation distance from the tip end to the substrate. L is the distance between a differential surface section of the tip and the

substrate, r is the radius of the tip at a given vertical position, R is the radius of the spherical cap at the tip apex, ε is the dielectric constant of the solution in this system, ε_0 is the permittivity of a vacuum, κ^{-1} is the Debye length, ψ is the surface potential, A is combined Hamaker constant of the tip-solution-substrate system, and subscripts S and T refer to substrate and tip, respectively.

With these equations (equations (3-2) and (3-3)), the DLVO model (constant potential) was fitted to the experimental force curves obtained between a silicon nitride tip and the substrates (the Glass-Substrate and the Fused Alumina-Substrate) or the two faces of kaolinite particles (the silica tetrahedral face and the alumina octahedral face). When AFM force data are analyzed, DLVO theory requires the input of two diffuse layer potentials, $\psi_{surface}$ and $\psi_{silicon\ nitride\ tip}$. On the basis of the assumption that the measured ζ-potentials are good approximations for these diffuse layer potentials in low electrolyte conditions, we can use them as a guide in theoretical fitting of the experimental force data. Experimental force profiles at each pH can be fitted by fixing $\psi_{silicon\ nitride\ tip}$ at ζ-silicon nitride tip and adjust $\psi_{surface}$ until theoretical and experimental force profiles overlap. The surface potential of the silicon nitride tip at varying pH was taken from the literature [128].

The surface potential of the substrates or each of the two faces of kaolinite was estimated by matching the DLVO model to the experimental force curves. The parameters used for the DLVO model are: R = 120 nm, $\beta = 36.5^0$, $A_{silicon\text{-}nitride}$ = 1.62 x 10^{-19} J [128], $A_{Kaolinite}$ = 6.80 x 10^{-20} J [129], $A_{alumina}$ = 1.52 x 10^{-19} J, A_{glass} = 6.50 x 10^{-20} J, and A_{water} = 3.70 x 10^{-20} J [130]. The surface potential was then converted to surface charge density (σ) using the Grahame equation as follows:

$$\sigma = \sqrt{8c_0\varepsilon_0\varepsilon k_B T}.\sinh\left(\frac{e\psi}{2k_B T}\right) \tag{3-7}$$

where, c_0 is the bulk ion-number concentration of the salt, k_B is the Boltzmann constant, e is the electronic charge and T is the absolute temperature.

3.3 Results and Discussion

3.3.1 Interaction Forces at Reference Substrates

AFM images of the glass and fused alumina substrates are shown in Figure 3.4. The root-mean-square surface roughness values for the glass and fused alumina substrates were determined as 0.37 nm and 0.34 nm, respectively. The interaction forces between the silicon nitride tip and the glass and the fused alumina substrates are shown in Figure 3.5. The iso-electric point (pH at which the surface carries zero net electric charge) of the silicon nitride tip as determined from the interaction between a silicon nitride tip and a silicon nitride wafer was taken as pH 4 [128]. Therefore, silicon nitride is expected to be negatively charged at pH > 4. However, a few studies have reported an iso-electric point of silicon nitride in between pH 5-7, depending on the treatment of the surface [131-133].

Five force curves are shown for each pH value of interest to establish the good reproducibility between the experimental force curves (see Figure 3.5). A 10-20% variation in the magnitude of colloidal forces is commonly observed in AFM studies [127]. As expected, repulsive interactions dominate between the silicon nitride tip and the

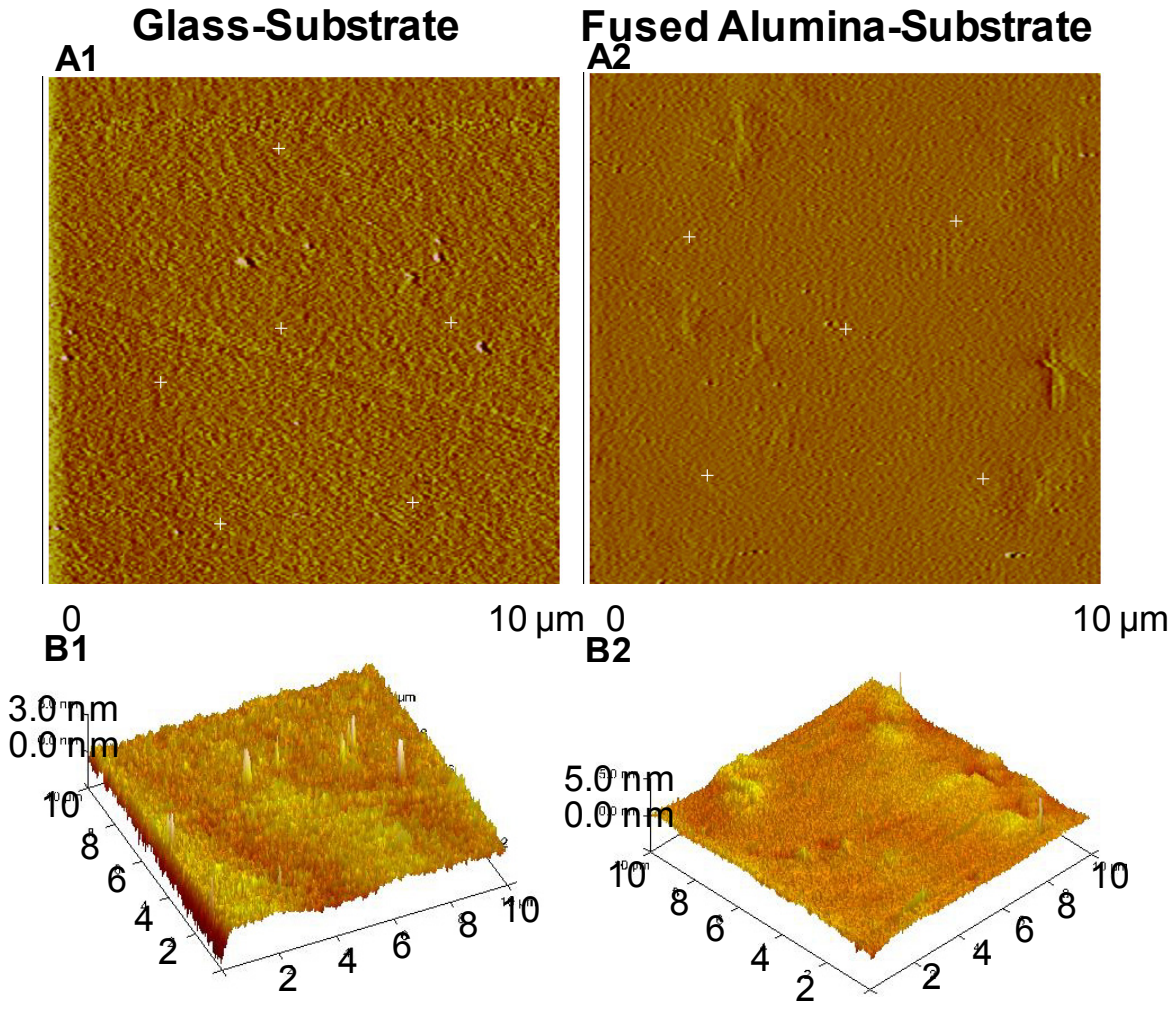

Figure 3.4- Topographic height images of Glass-Substrate (A1 and B1 above) and Fused Alumina-Substrate (A2 and B2), as obtained by AFM using a silicon nitride tip in contact mode. The white cross-bars on the A1 and A2 images show the location where force measurements between the silicon nitride tip and the substrate were performed.

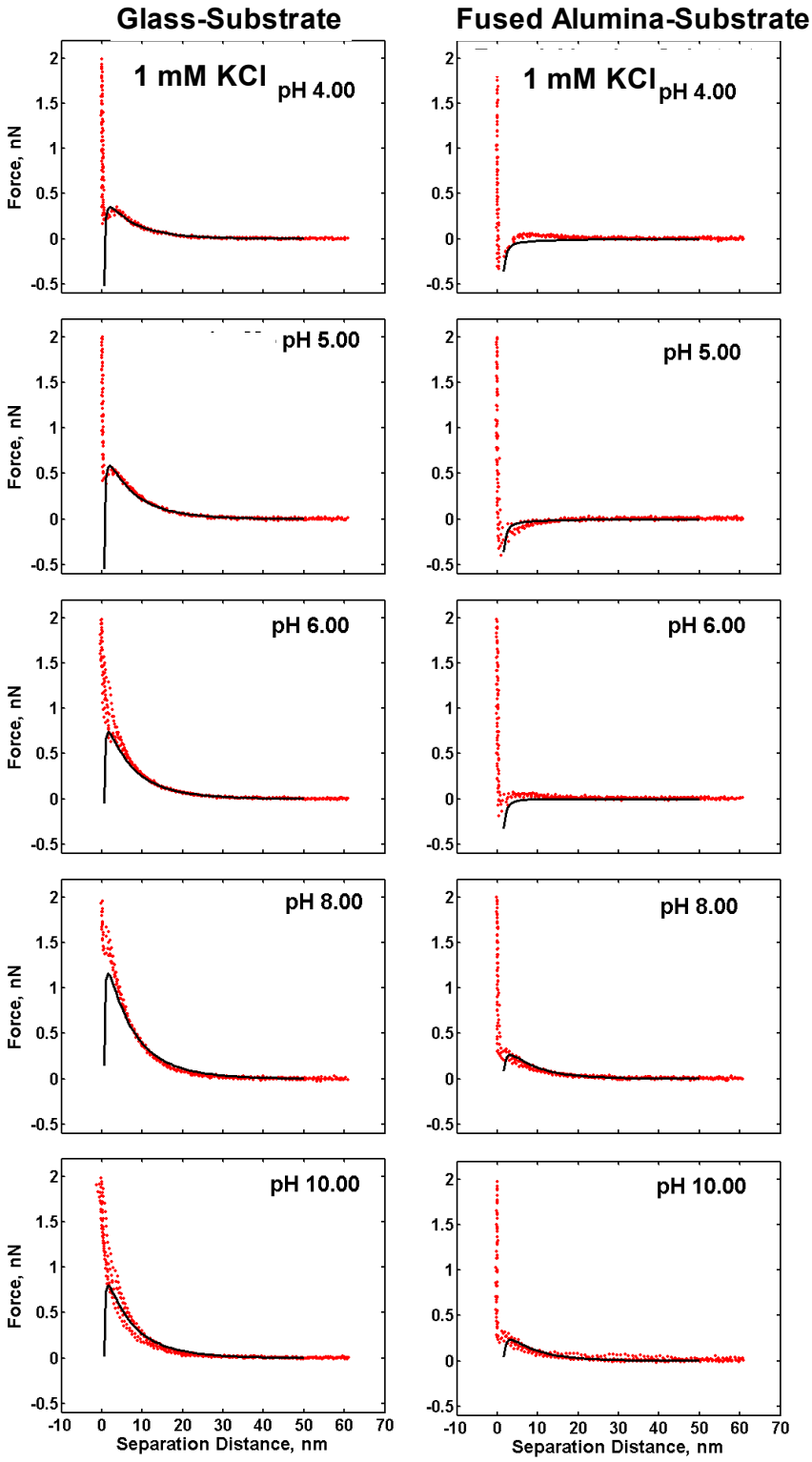

Figure 3.5- Interaction forces measured between a silicon nitride tip and the Glass-Substrate (left), and the Fused Alumina-Substrate (right) in 1 mM KCl solution at increasing pH. Five replicates (red-circle) of force curves at different locations on the substrate along with DLVO fit (black-line) are shown.

Glass-Substrate at all pH > 4 (see Figure 3.5 and Table 3.1). At least 50 force curves were analyzed at any given pH of the system, unless otherwise stated.

The magnitude of repulsive forces (indicated by positive sign in forces) increased by a factor of 5 (+0.24 to +1.22 nN) with increasing pH from 4 to 8, in good agreement with the DLVO theory. At pH 10, a slight reduction in the repulsive forces to +0.94 nN was observed, which may be related to the dissolution of glass at higher pH. At distances > 2 nm, the long-range electrostatic double layer repulsion dominates the interaction between a silicon nitride tip and the Glass-Substrate which extend up to 20 to 30 nm with increasing pH values. At distances < 2 nm, the snap-in contact between the silicon nitride tip and the Glass-Substrate was observed due to short-range van der Walls attraction. The van der Walls force being attractive and this dominant force causes the snap-in contact between the silicon nitride tip and the Glass-Substrate. At these distances, electrostatic repulsion is the dominant interaction compared to short-range interaction due to van der Wall, hydration and solvation forces which are negligible. The interaction range between a silicon nitride tip and the Glass-Substrate was nearly constant to 22-28 nm at all pH values (Table 3.1). The colloidal interaction forces indicate that the iso-electric point of the glass substrate is at a pH value < 4. This is in good agreement with the iso-electric point of pH 3.5 for glass as reported in the literature [134]. Few researchers have also determined the iso-electric point of silica surface using AFM surface force measurement considering silica as the substrate or the probe attached to the cantilever. Raiteri *et al.* [135] found the iso-electric point at pH 3.5 of SiO_2 film (>100 nm thick) as a substrate from the surface force measurements under similar solution chemistry conditions.

Table 3.1- Experimental interaction forces and the interaction range measured between silicon nitride tip and the substrates

	Glass-Substrate		Fused Alumina-Substrate	
pH	**Force nN**	**Range nm**	**Force nN**	**Range nm**
4	+0.241 ± 0.087	22.30 ± 4.51	-0.486 ± 0.286	11.81 ± 9.16
5	+0.562 ± 0.082	28.08 ± 3.83	-0.272 ± 0.097	17.49 ± 4.00
6	+0.538 ± 0.211	27.09 ± 6.05	-0.119 ± 0.060	2.73 ± 1.08
8	+1.226 ± 0.347	28.40 ± 5.58	+0.303 ± 0.057	24.33 ± 3.94
10	+0.943 ± 0.195	28.05 ± 3.86	+0.281 ± 0.036	19.03 ± 3.71

Note that the average ± standard deviations were calculated from 50 experimental forces between a silicon nitride tip and the substrates at 10 different locations with 5 repetitions at any given location. Positive and negative sign in force indicate repulsion and attraction, respectively.

Sokolov *et al.* [133] also determined the iso-electric point of silica at less than pH 4.0 from the surface force measurements between silica probe and polyurethane substrate. In contrast to the Glass-Substrate, attractive interaction dominates between a silicon nitride tip and the Fused Alumina-Substrate at pH < 6, whereas repulsive interactions were observed at pH 8 and 10 (see Figure 3.5 and Table 3.1). At pH < 6, the attractive forces (indicated by negative sign in forces) dominated by electrostatic attraction between a silicon nitride tip and the Fused Alumina-Substrate decreased by a factor of 4 (-0.49 nN to -0.12 nN) with increasing pH from 4 to 6, whereas electrostatic repulsive forces of the order of 0.30 nN were observed at pH 8 and 10. Again, a good fit between experimental force curves and DLVO theory was observed at all pH values. There is no significant dependence on interaction range with pH observed (Table 3.1), though short range attractive interaction was observed at pH 6. The force curves indicate that the isoelectric-point of Fused Alumina-Substrate is between pH 6 and 8, in good agreement with the isoelectric point of alumina at pH 7 to 9 as reported in the literature [112, 134]. Similar to our finding, Veeramasuneni *et al.* [119] and Yalamanchili *et al.* [121] also observed such similar trends in surface force measurements between the silica probe and the α-alumina substrate, i.e., attractive interaction at pH 5.5, 6.4 and 8.6, and repulsive interaction at pH 10.2 and 10.8, in de-ionized water adjusted to different pH values. However, they observed over one order of magnitude larger surface forces between the silica probe and the α-alumina substrate, which could be related to differences in the probe size and composition (4.8 μm silica probe used in their work vs. 120 nm silicon nitride tip used in this work). In research reported by Hupka [112] the repulsive force between a silica sphere and a flat surface was found to increase by a

factor of about 5 when the silica sphere colloidal probe diameter was increased from 1 μm to 20 μm.

3.3.2 Interaction Forces at Kaolinite Faces

The two faces of kaolinite are the silica face (001 basal plane) and the alumina face (00$\underline{1}$ basal plane), as discussed in the introduction. Therefore, it is expected that the 001 face of kaolinite will behave like the Glass-Substrate, and will be negatively charged at pH > 4.0. Also, it is expected that the 00$\underline{1}$ face of kaolinite will behave like the Fused Alumina-Substrate, and will be positively charged at pH < 6.0 and negatively charged at pH 8.0 and 10.0. In this way, kaolinite particles which attach to the glass substrate will expose the 001 face (silica tetrahedral layer) and the kaolinite particles which attach to the fused alumina substrate will expose the 00$\underline{1}$ face (alumina octahedral layer) to the silicon nitride tip (see Figure 3.1).

The topographic images of kaolinite particles on glass and fused alumina substrates are shown in Figure 3.6. Both the images confirm the pseudo-hexagonal shape and platy features of the kaolinite particles. Kaolinite particles consist of several layers of the silica-alumina bilayers, though in some images, a single layer of kaolinite (0.7 nm thick) was also observed (images not shown). The interaction forces between the silicon nitride tip and the two faces of kaolinite are shown in Figure 3.7. Again, a good reproducibility of force curves is shown by five replicates performed on different particles. Similar to Glass-Substrate, when the silica tetrahedral layer of kaolinite is exposed, a repulsive interaction dominates between the silicon nitride tip and the 001 face of kaolinite at all pH values, which indicates an iso-electric point of pH < 4 for the silica

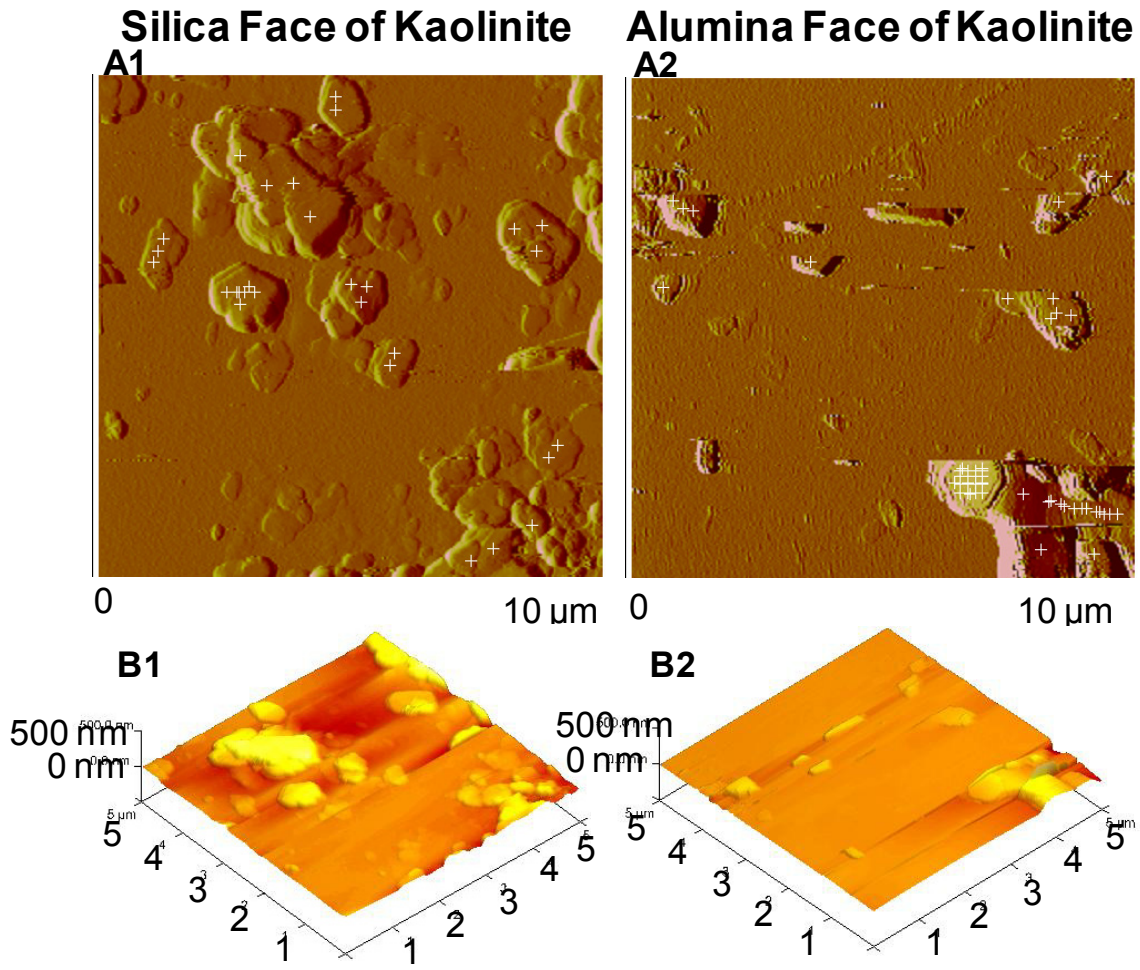

Figure 3.6- Topographic height images of kaolinite particles deposited on glass (left) and fused alumina (right) substrates respectively, as obtained by AFM using a silicon nitride tip in the contact mode. The white cross-bars on A1 and A2 images show the locations where the forces between the silicon nitride tip and the kaolinite faces were measured.

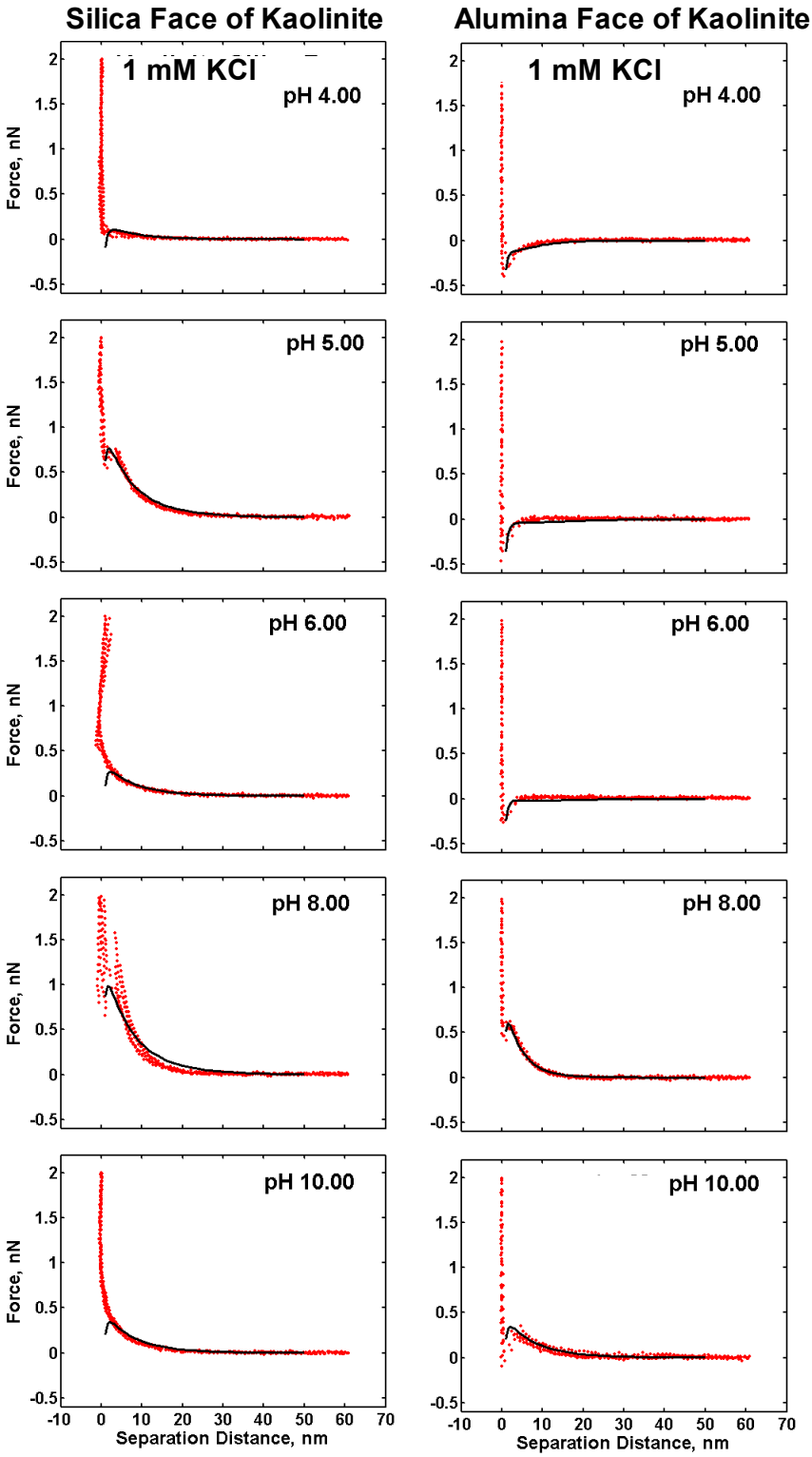

Figure 3.7- Interaction forces measured between silicon nitride tip and silica tetrahedral face (left), and alumina octahedral face (right) of kaolinite in 1 mM KCl solution at increasing pH. Five replicates (red-circle) of force curves on different particles along with DLVO fit (black-line) curve are shown.

face of kaolinite The long-range electrostatic repulsive forces between the silicon nitride tip and the silica face of kaolinite fit well with the DLVO model. The magnitude of electrostatic repulsion increased nearly over a magnitude from 0.15 to 1.28 nN with increasing pH. This is an interesting result, as an increase in over a magnitude of repulsive force could not be explained solely by the increasing surface potential and/or surface charge density of the silicon nitride tip with increasing pH. This suggests some contribution from the pH dependent surface charge density sites on the silica tetrahedral layer of kaolinite and contradicts the assumption that the silica tetrahedral face of kaolinite carries a permanent negative charge and does not show a dependency on pH. Note that the traditional position accounts for the negative charge due to minor substitution of Al^{3+} for Si^{3+} in the silica tetrahedral layer and does not account for the possibility of broken bonds which may explain some surface charge dependency on pH variation. The interaction range between a silicon nitride tip and the silica face of kaolinite does not change appreciably with increasing pH, in agreement with the results obtained on the Glass-Substrate (Table 3.2).

Similar to the pH dependency of our AFM measurement and our calculated surface charge densities for the basal planes of kaolinite, Zhou and Gunter [136] observed that the surface charge of kaolinite particles determined from potentiometric titration are over one order of magnitude greater than that predicted by varying the surface site concentration on the edge faces of kaolinite.

Even adding the structural charge of kaolinite particles determined from the cationic exchange capacity in acidic solutions [28], the results do not match the surface

Table 3.2- Experimental interaction forces and the interaction range measured between silicon nitride tip and the two faces of kaolinite

	Silica Face of Kaolinite		**Alumina Face of Kaolinite**	
pH	**Force nN**	**Range nm**	**Force nN**	**Range nm**
4	+0.147 ± 0.073	20.85 ± 3.57	-0.308 ± 0.102	12.47 ± 5.67
5	+0.817 ± 0.168	25.24 ± 2.58	-0.406 ± 0.084	6.71 ± 2.42
6	+0.667 ± 0.183	30.05 ± 5.99	-0.217 ± 0.049	4.91 ± 1.36
8	+1.282 ± 0.296	20.80 ± 3.05	+0.568 ± 0.099	12.15 ± 1.51
10	+0.604 ± 0.070	23.63 ± 4.20	+0.263 ± 0.033	17.05 ± 8.08

Note that the average ± standard deviations were calculated from 50 experimental forces on at least 10 different particles, with five measurements at one location on each particle.

charge density determined from the potentiometric titration, which led the authors to conclude that "basal faces of kaolinite are ionizable in aqueous solutions."

As expected, the interaction forces obtained on the silica face of kaolinite are comparable to these obtained on the Glass-Substrate with slightly decreased forces on the silica face of kaolinite at pH 4 and 10, and slightly increased forces at pH 5, 6 and 8.

It should be noted that the Glass-Substrate is mainly composed of SiO_2 beside other alkali and alkaline earth oxides such as Na_2O, CaO, MgO and K_2O, as well as $A1_2O_3$, Fe_2O_3/FeO [137], whereas the silica face of kaolinite is composed of SiO_2 only. These slight variations in the magnitude of repulsive forces are expected from the difference in the composition of the Glass-Substrate and the silica face of kaolinite.

In contrast to the silica tetrahedral face of kaolinite, attractive interaction dominates between a silicon nitride tip and the alumina octahedral face of kaolinite at pH 4, 5 and 6. At higher pH of 8 and 10, repulsive interactions were observed. The attractive interaction forces only decreased by a factor of 1.5 (-0.31 to -0.22 nN) with increasing pH from 4 to 6, and turned repulsive to +0.57 nN at pH 8 and +0.26 nN at pH 10 (Table 3.2). The range of interaction also decreased from 10 nm to 4.5 nm with increasing pH from 4 to 6, and remains constant at 12 nm at higher pH of 8 and 10. The force curves seem to be in accordance with the DLVO theory, as shown in Figure 3.7. These results suggest that the iso-electric point of the alumina face of kaolinite (00$\underline{1}$ basal plane) lies between pH 6 and 8. The force curves on the alumina face of kaolinite and the Fused Alumina-Substrate are comparable, and of the similar magnitude.

Interestingly, at pH 4 the attractive force field of the alumina face of kaolinite (-0.30 nN) is greater than the repulsive force field of the silica face (+0.15 nN), whereas at

pH > 5 the repulsive force field of the silica face dominates over the attractive force field of the alumina face (the magnitude of the repulsive force on the silica face is greater than the attractive force on the alumina face of kaolinite). Also, the long range of electrostatic repulsion on the silica face is significantly greater (by at least 10 nm) than the range of electrostatic attraction for the alumina face of kaolinite. This implies that the repulsive force field on the silica face starts to have a significant influence at greater separation distances, and dominates over the attractive force field from the alumina face of kaolinite at pH > 5. Hypothetically, if we ignore any contribution from the edge surfaces of the kaolinite particles, then it can be said from the combined interaction of the silica and the alumina faces of kaolinite, that kaolinite particles will be positively charged at pH 4, and will be negatively charged at pH > 5. It is commonly accepted that edge surfaces of kaolinite contain pH-dependent surface charge due to broken silica and alumina bonds with an iso-electric point at neutral pH of 7. In this way, the iso-electric point of kaolinite can be determined from the combined silica tetrahedral face and the alumina octahedral face along with the edge contribution. Such analysis is currently under investigation. Nevertheless, the present work on the surface force measurements demonstrates that the two faces of kaolinite – the silica face and the alumina face – differ significantly in their surface chemistry characteristics.

3.3.3 Surface Potential and Surface Charge

The surface potentials and surface charge densities determined from the DLVO fits of the experimental force curves on the Glass-Substrate and the Fused Alumina-

Substrate are shown in Figure 3.8. Zeta-potential values of silica and alumina particles as determined by electrophoresis are also shown in Figure 3.8 [134].

The surface potential of the silicon-nitride tip varied from -25 to -75 mV with increasing pH from 4 to 10. The surface potential of the Glass-Substrate varied from -56 to -92 mV with increasing pH from 4 to 8 and slightly decreased to -77 mV at pH 10. In contrast, the surface potential of the Fused Alumina-Substrate varied from +60 to -39 mV with increasing pH from 4 to 10.

The surface potentials of the Glass-Substrate as estimated from surface force measurements are in reasonably good agreement with the zeta-potential of silica particles as determined by electrophoresis. However, the surface potential values of Fused Alumina-Substrate estimated from surface force measurements are somewhat lower than the zeta-potential of alumina particles determined by electrophoresis. This difference may be related to the purity of the Fused Alumina-Substrate vs. that of the alumina particles.

Figure 3.9 shows the surface potential and the surface charge density of the two faces of kaolinite (the silica face and the alumina face) estimated from surface force measurement via DLVO model fitting. For the first time, the surface potential and/or surface charge of the silica tetrahedral face and the alumina octahedral face of kaolinite particles have been determined and are shown to be dependent on solution pH (see Figure 3.9), as opposed to the existing belief that the two faces of kaolinite carry a fixed negative structural charge. Furthermore, the alumina octahedral face of kaolinite shows an iso-electric point in between pH 6 and 8, whereas the silica tetrahedral face of kaolinite shows an iso-electric point at pH < 4. The surface potential of the alumina octahedral face varied from +50 to -37 mV with increasing pH from 4 to 10, whereas the silica tetrahedral face showed

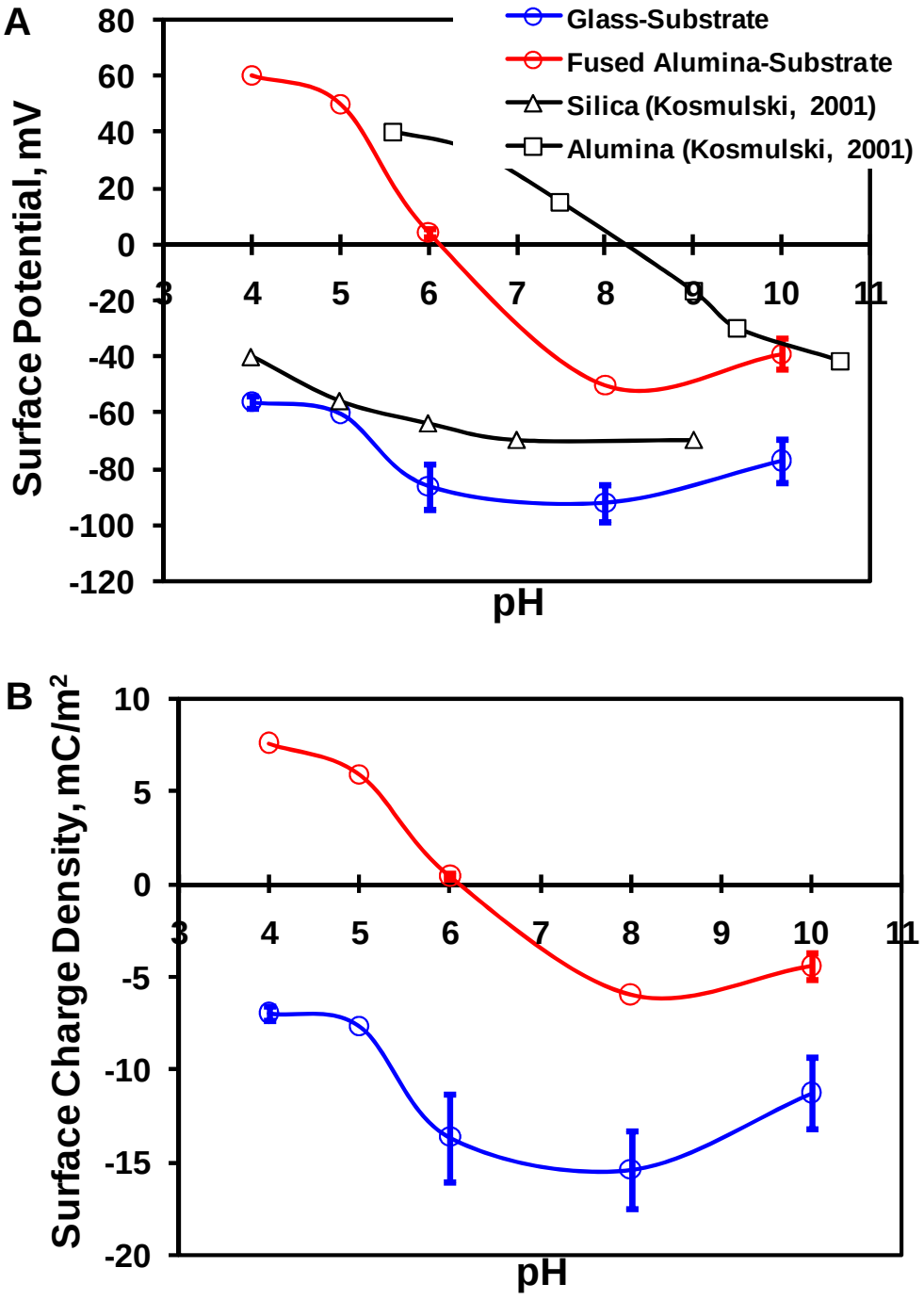

Figure 3.8- (A) Surface potential and (B) surface charge of the Glass-Substrate and the Fused Alumina-Substrate as a function of pH. The calculated surface potentials are compared to electrophoretic zeta potentials reported for silica and alumina by Kosmulski [134].

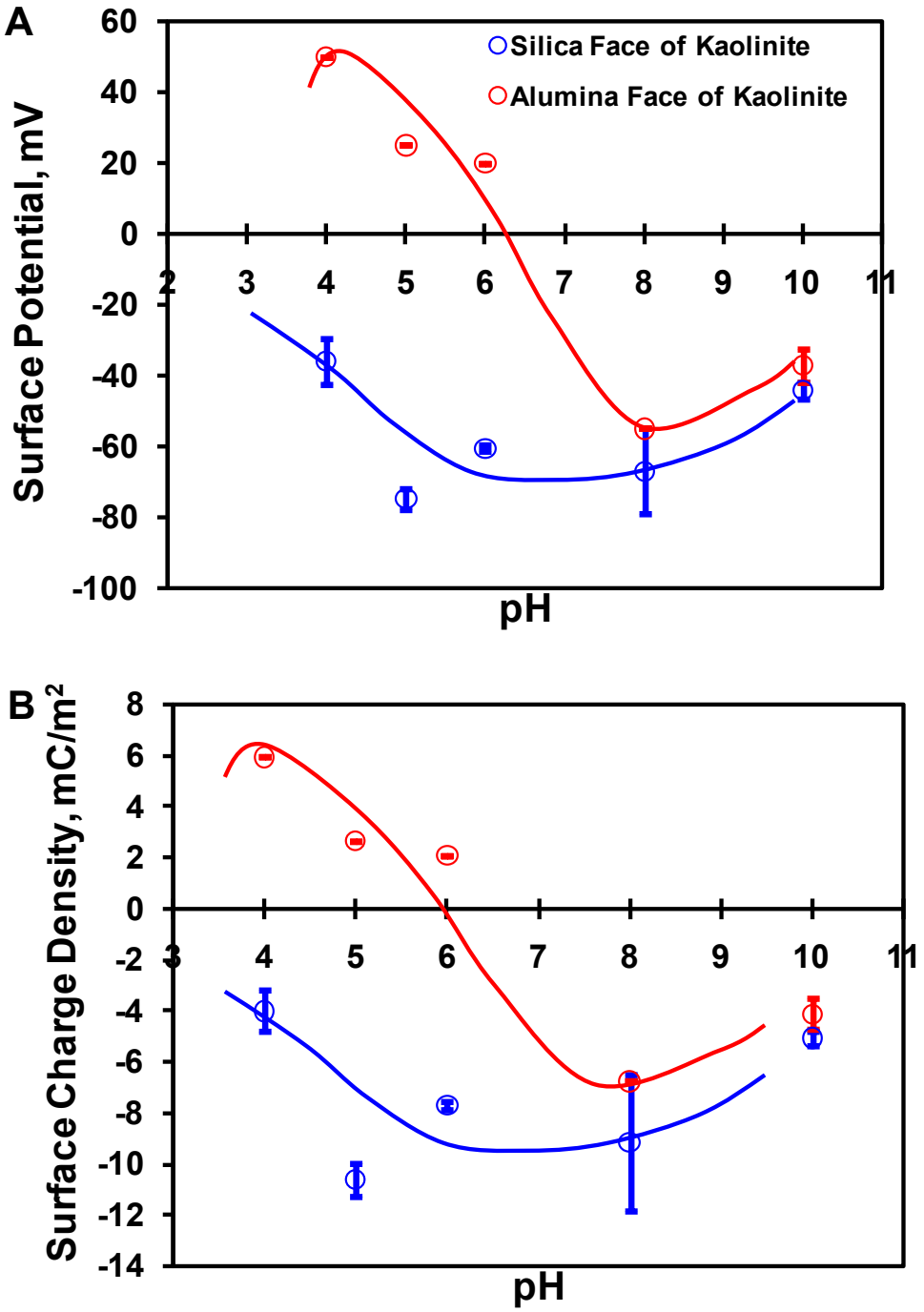

Figure 3.9- Surface potential and surface charge density of the silica face (A) and the alumina face (B) of kaolinite particles as a function of pH.

negative surface potential over the entire pH range, which varied from -36 to -67 mV with increasing pH from 4 to 8, and a slight decrease at pH 10.

This new information should be helpful to explain the electrokinetics of kaolinite. Further research is in progress to accommodate the surface charge of the edge surfaces and the two basal plane surfaces to better understand the electrokinetic behavior of kaolinite particles.

3.4 Summary

The electrokinetic characteristics of kaolinite are typically considered based on electrophoretic measurements. It is evident that the electrophoretic measurements are compromised by the shape and anisotropic character of kaolinite particles and do not reveal too much surface chemistry detail. The present work describes a procedure to expose the two faces of kaolinite (silica tetrahedral face and alumina octahedral face) by ordered deposition of the kaolinite particles on glass and alumina substrates, respectively. In this way, the 001 and 00$\underline{1}$ basal plane surfaces were interrogated using AFM for surface force measurements. The surface forces were explained using DLVO theory and the magnitude of the surface forces and the interaction range were compared. Clearly, the present work demonstrates the different behavior of the two faces of kaolinite – the silica tetrahedral face and the alumina octahedral face. On this basis, the iso-electric point of the silica tetrahedral face and the alumina octahedral face were determined and found to be < pH 4 for the silica face and between pH 6 and 8 for the alumina face.

The electrokinetic properties of kaolinite will have a contribution from both faces of kaolinite (silica tetrahedral face and alumina octahedral face), as well as from edge

surfaces. AFM surface force results are significant and provide the basis to determine the surface charge density and surface potential of kaolinite faces, thus providing more detailed information regarding the surface chemistry of kaolinite. With this new information, it may be possible to further explain the electrokinetic behavior of kaolinite particles, and their interactions in aqueous suspensions.

CHAPTER 4

ELECTROKINETICS AND TITRATION OF KAOLINITE PARTICLES

The electrokinetic properties of kaolinite are complicated by anisotropic particle features – nonuniform surface charge densities on the faces (the silica face, the alumina face and the edge surfaces), and its platy-shape. Numerous works have been conducted by researchers both experimentally and theoretically to predict the electrophoretic mobilities of the kaolinite particle and to improve the Smoluchowski's classical model in order to get better understanding of the electrokinetic properties for kaolinite particles. This dissertation research provides a review of the earlier works to attempt to predict the electrokinetic properties of kaolinite. Using Smoluchowski's classical model, the apparent iso-electric point for kaolinite was determined at less than pH 3 from electrophoretic measurement.

This chapter discussed the surface charge properties of kaolinite determined experimentally using traditional titration techniques such as M-R titration and potentiometric titration, and using a new technique to determine surface potential and surface charge density from surface force measurement using atomic force microscopy.

The point of zero charge for kaolinite particles will be established by titration techniques, and by surface force measurements.

4.1 Introduction

The surface chemistry of kaolinite [$Al_2Si_2O_5(OH)_4$], particularly its electrokinetic properties, is very important in many applications such as flotation, filtration, and many new applications such as clay-polymer nanocomposites and smart materials [1, 5-7, 53, 63, 67, 138-141]. The surface charge of kaolinite particles are manifested in their basal planes surfaces (001 and 00$\underline{1}$) and edge surfaces (010 and 110). The basal plane surfaces 001 and 00$\underline{1}$ consist of silica tetrahedral and alumina octahedral layers, respectively. The edge surfaces consist of broken covalent bonds of aluminol and silanol end-groups. It is believed that the basal planes of kaolinite carry a permanent negative charge due to isomorphous substitution of Al^{3+} for Si^{4+} in the silica tetrahedral, and Mg^{2+} for Al^{3+} in the alumina octahedral layer, whereas the edge surface carries a positive or negative charge depending on the pH of the system [23, 26, 49, 142]. Therefore, it is commonly assumed that the basal planes do not show a surface charge dependency with varying pH.

The surface charge densities of kaolinite particles are determined more frequently by electrophoretic technique to determine their iso-electric point. Researchers have reported the iso-electric point of kaolinite particle as pH of 2–4 by electrophoresis, depending on the source of kaolinite and sample preparation techniques [46, 51, 143, 144]. However, we must bear in mind that the electrophoresis is based on four basic assumptions: (1) the particle is rigid and nonconducting; (2) the local mean radius of curvature is much larger than the Debye screening length; (3) the surrounding fluid is

unbounded; and (4) the zeta-potential is uniform over the particle's surface. The kaolinite particles are pseudo-hexagonal platy shaped, and are of the order of less than a micron-to-nano sized range. Furthermore, the kaolinite particles have anisotropic properties in their basal planes surfaces and edge surfaces which complicates the electrophoretic analysis. Nevertheless, we rely on these measurements in the absence of appropriate theory.

Few researchers have also conducted potentiometric titration to determine the surface charge densities of kaolinite particles as a function of pH [34, 38]. These authors determined a point of zero net proton charge (pznpc) for kaolinite particles at pH 4.5 by titration study. The pznpc is the pH value at which the net proton surface charge is equal to zero [145, 146].

The main objective of this chapter is two-fold: (1) to highlight the limitation of the current electrophoretic theory to describe the electrokinetic properties of kaolinite particles; and (2) to compare electrophoresis potentiometer titration to determine the surface charge properties of kaolinite particles.

4.2 Materials and Methods

4.2.1 Sample Preparation

A clean English Kaolin (Imerys Inc., UK) was obtained from the St. Austell area in Cornwall, UK. The sample was cleaned with water only using elutriation to achieve classification at a size of less than 2 μm. No other chemical treatment was done. Further details about the kaolinite extraction and preparation are given in the literature [124]. The kaolinite was used as-received in this research. The kaolinite suspension was prepared in

high purity Milli-Q water (Millipore Inc.). The resistivity of the water was above 18 MΩ-cm in all experiments. Potassium chloride (1 mM, 10 mm and 100 mM solution) was used as background electrolyte. The pH was adjusted to its desired value using 0.1 M HCl or 0.1 M KOH solutions. All chemicals used were of ACS grade.

XRD analysis conducted on the kaolinite sample confirmed that the kaolinite is the dominant mineral phase. EDAX analysis of the kaolinite sample showed nearly 1:1 atomic distribution of aluminum (7.98%) and silicon (7.95%) with trace amounts of potassium (0.35%), calcium (0.08%) and iron (0.15%).

4.2.2 Zeta-Potential Measurements

The zeta-potential measurements were carried out by electrophoresis (ZetaPALS, Brookhaven Instrument Corp.; and Malvern Nanosizer). The particles suspension (0.05%) was prepared at desired solution concentration, and placed in between two electrodes. The particles mobilities were measured when the electric field is applied. This particle mobility is converted to zeta-potential ($\bar{\zeta}$) using Smoluchowski's equation as follows:

$$U = \frac{\varepsilon \varsigma}{4\pi\eta} E_{\infty} \tag{4-1}$$

Where E_{∞} is the applied electric field, and U is the particle velocity in a fluid with dielectric constant ε and viscosity η.

4.2.3 Mular-Roberts (M-R) Titration

M-R titration was named after two researchers, Mular and Roberts, who developed this technique to determine the point of zero charge of colloidal particles [147]. In this method, the pH of a suspension is measured at different ionic strengths of the solution [147]. The suspension is prepared at given solution chemistry – ionic strength and pH of the system. The ionic strength is then increased to yield a change in pH of the suspension. The change in the pH ($pH_i - pH_f$) when plotted with pH_f gave information about the iso-electric point of the particles.

At the iso-electric point:

$$\Delta pH = pH_i - pH_f = 0 \tag{4-2}$$

The particles suspension (1%) was prepared in 10 mM KCl solution. 20 ml of this suspension was taken in a SC-1 cleaned beaker in a continuous ultra high purity N_2 environment. The solution pH was then adjusted to some initial pH_i. The ionic strength was then increased to 100 mM using the appropriate amount of KCl, and the final pH (pH_f) of the system is noted. The results reported are the average of at least two full repeat experiments.

4.2.4 Potentiometric Titration

The particles suspension (5%) was prepared in 10 mM KCl solution (50 ml), and adjusted to initial acidic pH (pH_i) in a continuous ultra high purity N_2 environment. A small amount of base 10 µl (0.1M KOH) was added each time and pH of the suspension

was noted. This was continued until the pH of the suspension reach pH 9. The surface charge of the particle suspension is then calculated as:

$$\sigma = \left(\frac{F}{SA}\right)\left(\left[C_a - C_b\right] - \left[H^+\right] + \left[OH^-\right]\right) \tag{4-3}$$

where σ is the proton surface charge density (C/m^2), F is Faraday's constant, SA is mineral surface area (m^2/liter), and C_a and C_b are the amounts of acid and base titrant added (mol/liter), respectively.

4.3 Electrokinetic Theory

The electrokinetic theory deals with the charged surfaces in liquids, generally in water. Because of its high dielectric constant, water is a good solvent for ions. For this reason, most surfaces in water are charged. Different processes can lead to charging of the slid surfaces such as protonation or deprotonation reactions from the solid surfaces, lattice substitution of different valency ions, and specific adsorption. The lattice substitution is particularly important as the charging mechanism of the clay mineral surface.

Surface charges cause an electric field. This electric field attracts counter ions. The layer of surface charges and counter ions is called "electric double layer." Helmholtz first described the simplistic model of an electrical double layer; the counter ions bind directly to the surface and neutralize the surface charges much like in a plate capacitor. The electric field generated by the surface charges is accordingly limited to the thickness

of a molecular layer. Helmholtz's model was able to interpret some basic features of charged surfaces, but the model failed to explain the capacitance of an electric double layer.

Gouy and Chapman went a step further and took into account a thermal motion of the ions. Thermal fluctuations tend to drive the counterions away from the surface. They lead to the formulation of a diffuse layer, which is more extended than a molecular layer, as shown in Figure 4.1. Gouy and Chapman applied their theory on the electric double layer to the planar surfaces. Later, Debye and Hückel calculated the potential and ion distribution around the spherical surfaces. Both the Gouy-Chapman and Debye-Hückel are continuum theories.

Following the Gouy and Chapman model of "electrical diffuse double layer," the concentration of ions within the interface is assumed to follow the Boltzmann distribution which can be expressed as:

$$n_i(x) = n_i(\infty)\exp\left(\frac{-z_i e\psi_x}{kT}\right) \tag{4-4}$$

where ψ_x is electrostatic potential at the distance x from the surface of the clay platelet with a surface potential ψ_0, z_i is the valency of ion i and e is the electron charge (1.602 x 10^{-19} C). The symbol $n_i(x)$ represents the concentration of ion i in the electrolyte at the distance x from the particle surface and $n_i(\infty)$ is the concentration of ion i in the bulk solution. The product kT is the thermal energy (Brownian) with k being the Boltzmann constant and T is the absolute temperature (K). In a 1:1 symmetrical and indifferent

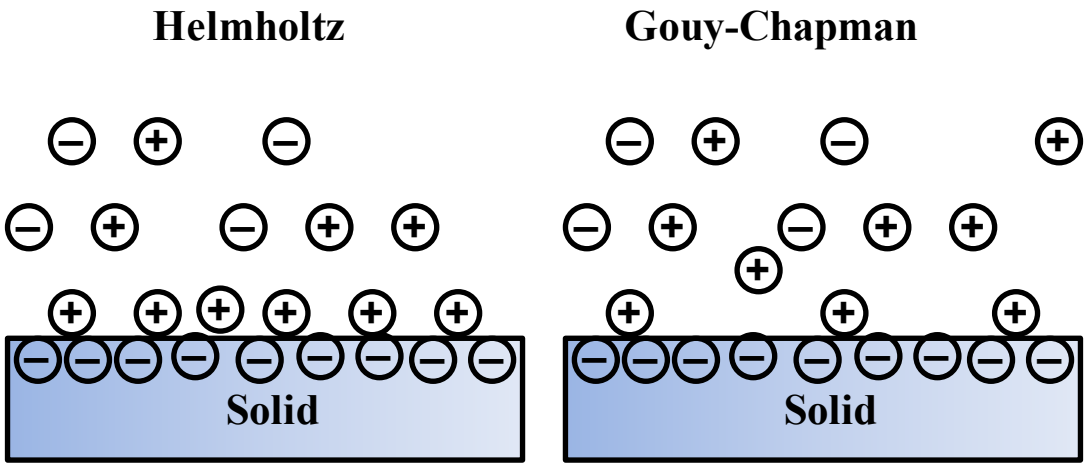

Figure 4.1- Helmholtz and Gouy-Chapman model of the electric double layer.

electrolyte solution, the charge density ρ_x at a distance x from the particle surface is given by the summation:

$$\rho_x = \sum_i z_i e n_i(x) \tag{4-5}$$

Substituting n_i (x) from equation (4-4):

$$\rho_x = \sum_i z_i e n_i(\infty) \exp\left(\frac{-z_i e \psi_x}{kT}\right) \tag{4-6}$$

A fundamental theorem of electrostatics, known as the Poisson equation, expresses the relationship between the charge density ρ_x at a point x and the change in the electrostatic potential ψ at that point in a medium with the dielectric constant ϵ_r:

$$\nabla^2 \psi = -\frac{\rho_x}{\varepsilon_o \varepsilon_r} \tag{4-7}$$

where ∇^2 is the Laplacian operator and can be reduced to $\partial^2 \psi / \partial x^2$ for a one-dimensional case which is appropriate for a double layer on a flat clay surface. Replacing ρ_x by equation (4-6):

$$\frac{\partial^2 \psi}{\partial x^2} = -\frac{1}{\varepsilon_o \varepsilon_r} \sum_i z_i e n_i(\infty) \exp\left(\frac{-z_i e \psi_x}{kT}\right) \tag{4-8}$$

This is the Poisson-Boltzmann equation which was considered to be the mathematical essence of the diffuse double layer. Unfortunately, there is no explicit solution for this equation but approximations for certain limiting cases exist; among these are Gouy-Chapman's approximation for moderate surface potentials and electrolyte concentrations up to 100 mM, and Debye-Hückel approximation for low surface potentials and dilute solutions. The Poison-Boltzmann model itself leads to imperfections due to several assumptions made in the theory such as:

i. The finites size of the ions was neglected.
ii. Ions in solution were considered as a continuous charge distribution.
iii. All noncoulombic interactions were disregarded.
iv. The solvent is supposed to be continuous and the permittivity of the medium to be constant.
v. Surfaces are assumed to be flat on the molecular scale.
vi. Image forces between the ions and the surface were ignored.

Despite these strong assumptions, the Poisson-Boltzmann theory describes electric double layers surprising well. The reason is that errors lead to opposite effects and compensate each other. For example, including noncoulombic interactions lead to an increase of the ion concentration at the surface and a reduced surface potential. On the other hand, taking the finite size of the ions into account leads to a lower ion concentration at the surface and thus an increased surface potential. Likewise, a reduction of the dielectric permittivity due to the electric field increases its range but at the same time reduces the surface potential because less ions dissociate or adsorb. The readers are

also advised to review the literature for electrokinetic theory in greater details [24, 148-150].

The most rigorous approach to improve the Poison-Boltzmann theory is by starting from first principles, applying statistical thermodynamic equations for bulk electrolytes and nonuniform fluids. Excellent reviews about the statistical mechanics of double layer have appeared [151, 152]. Also computer simulations increased our understanding of electric double layer significantly [153]. Despite these advancements dealing with statistical mechanics and computer simulations, simple analytical formulas that can easily be applied are not available. In addition, for a complete description, the molecular nature of the solvent should be considered.

Fortunately, Stern proposed a relatively simple semi-empirical extension of the Gouy-Chapman theory. In Stern theory, the electric double layer is divided into two parts: an inner part, the Stern layer; and an outer part, the Gouy or diffuse layer. The Stern layer consists of a layer of ions (δ) which are directly adsorbed to the surface, and which is immobile. The potential at the point where the bound Stern layer ends and the mobile diffuse layer begins is the zeta potential (ς potential). A simplified version of the Stern layer is shown in the Figure 4.2.

Following the Stern model of electric double layer, the surface potential of the solid particles at the solid-liquid interface is frequently characterized by electrophoresis. Significant contributions have already been made regarding electrophoresis from numerous researchers dealing with the field of electrokinetic phenomena. These studies range from the earliest works of Smoluchowski [149] and Henry [154], where the attention was devoted to the motion of a single spherical colloidal particle under certain

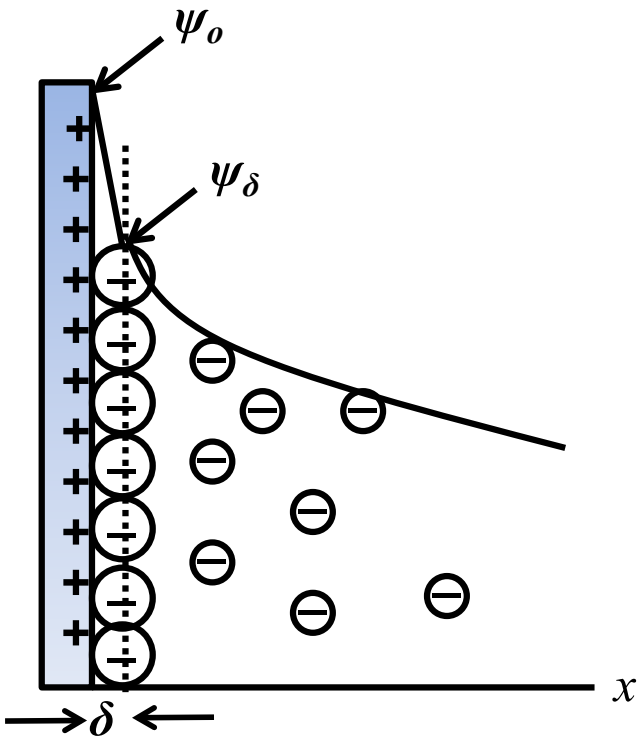

Figure 4.2- Stern model of the electric double layer.

limiting conditions, to modern theories detailing the motion of a swarm of particles in a concentrated dispersion employing cell models.

Here, we will present an analysis of evaluating the electrophoretic velocity of a charged particle when it is placed in an electric field. First, the motion of a single charged spherical particle under the influence of an external field is presented. After formulating the appropriate mathematical equations for such condition, two limiting cases of the problem will be presented, namely, when the particle is very small or in an almost perfect dielectric with few mobile charges, i.e., in the limit $\kappa a \ll 1$, and when the particle is large or in a highly concentrated electrolyte, i.e., $\kappa a \gg 1$. All the above mentioned analyses will be confined to particles having low surface potentials. Following the analysis of single charged spherical particle, complexities of dealing with the electrokinetic motion of platy shaped kaolinite particles will be presented. In the entire analysis, the particle will be assumed to be rigid and electrically nonconducting.

Let us first consider a spherical particle of radius a bearing a charge Q_s suspended in a pure dielectric fluid (containing no free charge or ions). When subjected to a uniform external electric field, E_∞, the particle will translate under the influence of the electric force acting on it. Since there is no free charge in the dielectric fluid, there will be no flow of this fluid under the influence of the uniform external electric field as long as there is no pressure gradient. The net electrical force on the charged particle will simply be:

$$F_E = Q_s E_\infty \tag{4-9}$$

The particle encounters an oppositely directed fluid drag force as soon as the particle starts to move under the influence of this electrical force:

$$F_H = 6\pi\mu a U \tag{4-10}$$

where μ is the fluid viscosity and U is the particle velocity. Equating the electrical and drag forces for steady-state motion, one obtains:

$$U = \frac{Q_s E_\infty}{6\pi\mu a} \tag{4-11}$$

The direction of the particle velocity will be governed by the sign of the particle charge. The electrophoretic mobility of the particle can be defined as velocity per unit applied electric field, and is given by:

$$\eta = \frac{U}{E_\infty} = \frac{Q_s}{6\pi\mu a} \tag{4-12}$$

Now, consider when a single charged spherical particle of radius a carrying a total charge Q_s is immersed in an electroneutral electrolyte solution (volumetric charge density, ρ_f, is zero). The charged particle will polarize the electrolyte solution surrounding it, resulting in the formation of an electric double layer. The electric double layer will have a spatially varying volumetric charge density. As soon as a charge density

is developed in the electrolyte solution, it will experience an electric body force under the influence of the overall electric field near the particle. The overall electric field is superposition of two fields:

i. the unidirectional external field
ii. a spherically symmetric field in the double layer due to the charged particle in absence of the external field

The electric body force will cause a motion in the fluid immediately surrounding the particle, and will be opposite to the direction of the particle movement. In addition to the fluid flow, the concentration gradients of the ions, as well as the electric potential gradients, will give rise to ionic fluxes, which are usually described in terms of the Nernst-Planck equations.

Therefore, a complete analysis of electrophoresis of a charged particle in an electrolyte solution involves consideration of following three coupled physical processes:

i. Interaction of the charged particle with the external electric field giving rise to an electrical force on the particle
ii. Formation of the electric double layer surrounding the particle giving rise to a spatially inhomogeneous charge distribution, which results in an electrical body force driven fluid flow, and,
iii. Transport of ions relative to the charged particle under the combined influence of convection, diffusion and migration.

The governing equations describing the three coupled processes mentioned above apply to the steady state velocity of a single charged spherical particle under an imposed electric field E_∞. The geometry is shown in Figure 4.3. Note that the particle velocity U,

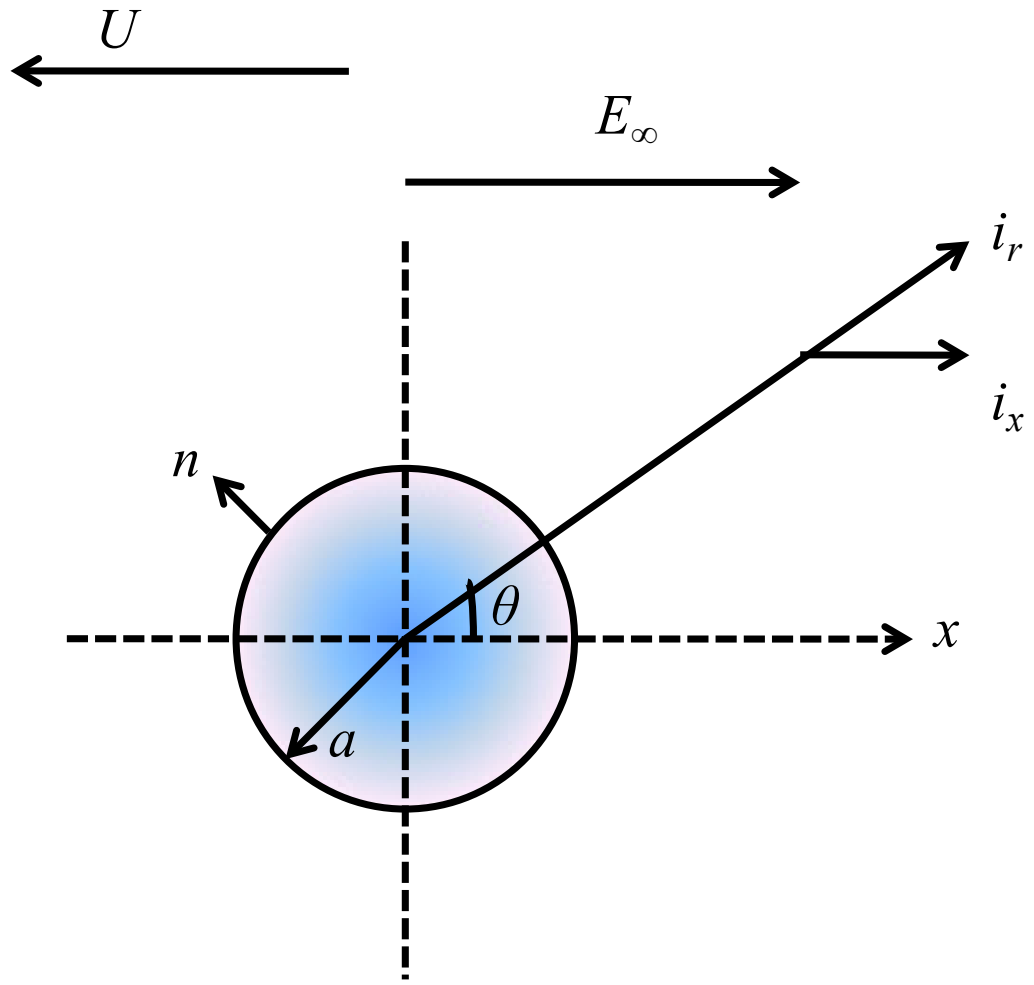

Figure 4.3- A spherical particle of radius a held stationary in a uniform electric field E_∞.

and the electric field are represented as vector quantities. The fixed particle reference frame was chosen here, and the flow of an electrolyte solution around a stationary charged particle was considered.

In this case, far from the particle, the velocity of electrolyte solution is then given as:

$$u_\infty = -Ui_x \tag{4-13}$$

where U is the particle velocity along the x direction and i_x is a unit vector. Consequently, $u_\infty = -U$ represents the fluid velocity necessary to keep the particle stationary. The electrolyte solution contains N ionic species of valency z_i with a bulk concentration $n_{i\infty}$ and diffusion coefficient D_i.

The electric potential, ψ, in the electrolyte solution surrounding the charged particle is given by equation (4-7). For small Reynolds number and neglecting the effect of gravity, the electrolyte solution velocity field, u, is given by the modified momentum equation as:

$$\mu\nabla^2 u - \nabla p - \rho_x \nabla\psi = 0 \tag{4-14}$$

where ∇p is the pressure gradient and $\rho_x\nabla\psi$ is the electrical body force on the electrolyte solution caused by the overall potential gradient, $\nabla\psi$. The steady-state continuity equation for the electrolyte solution under dilute conditions, i.e., constant density, provides:

$$\nabla u = 0 \tag{4-15}$$

The ionic fluxes are given by the Nernst-Planck equations, which can be written in terms of the number concentration, n_i, of the i^{th} ionic species as:

$$j_i^{**} = n_i v_i = n_i u - D_i \nabla n_i - \frac{z_i e n_i D_i}{kT} \nabla \psi \tag{4-16}$$

where v_i and D_i are the velocity and diffusivity of the i^{th} ionic species, respectively. For a steady state transport process, the ion conservation equation then yields:

$$\nabla . j_i^{**} = n_i v_i = \nabla . \left[n_i u - D_i \nabla n_i - \frac{z_i e n_i D_i}{kT} \nabla \psi \right] = 0 \tag{4-17}$$

4.3.1 Electrophoresis in the Limit $\kappa a \ll 1$

Using a spherical coordinate system and utilizing symmetry in the angular directions, the potential distribution around the sphere can be represented by the Poisson-Boltzmann equation as:

$$\frac{1}{r^2} \frac{\partial}{dr} \left(r^2 \frac{\partial \psi}{dr} \right) = \kappa^2 \psi \tag{4-18}$$

where κ is the inverse Debye length, given by:

$$\kappa = \left(\frac{2e^2 z^2 n_\infty}{\varepsilon kT} \right)^{1/2} \tag{4-19}$$

Let say

$$\xi = r\psi \tag{4-20}$$

which renders equation (4-18) as:

$$\frac{\partial^2 \xi}{dr^2} = \kappa^2 \xi \tag{4-21}$$

The general solution of the above equation is:

$$\xi = Ae^{-\kappa r} + Be^{-\kappa r} \tag{4-22}$$

where A and B are constants, which can be evaluated from the boundary conditions. The boundary conditions are:

$$\psi \to \psi_\infty = 0 \quad \text{as} \quad r \to \infty \tag{4-23}$$

and

$$\psi \to \psi_s = \zeta \quad \text{as} \quad r = a \tag{4-24}$$

Substituting the boundary conditions, equations (4-23) and (4-24) in equation (4-22) yields the potential distribution as:

$$\psi = \zeta \frac{a}{r} \exp\left[-\kappa\left(r-a\right)\right] \tag{4-25}$$

Now to determine the charge on the particle surface, Q_s, we will apply the electroneutrality condition (total charge of a system comprised of a charged particle and the surrounding electrolyte should be zero) as:

$$Q_s = -\int_a^{\infty} \left(4\pi r^2\right) \rho_f \partial r \tag{4-26}$$

Using Poisson's equation,

$$\frac{1}{r^2}\frac{\partial}{dr}\left(r^2 \frac{\partial \psi}{dr}\right) = -\frac{\rho_f}{\varepsilon} \tag{4-27}$$

Substituting equation (4-27) into equation (4-26) gives:

$$Q_s = 4\pi\varepsilon \int_a^{\infty} r^2 \left[\frac{1}{r^2}\frac{\partial}{dr}\left(r^2 \frac{\partial \psi}{dr}\right)\right] \partial r = 4\pi\varepsilon \left[r^2 \frac{\partial \psi}{dr}\right]_a^{\infty} \tag{4-28}$$

Noting that

$$r \to \infty, \quad \frac{d\psi}{dr} \to 0 \tag{4-29}$$

we obtain

$$Q_s = 4\pi a^2 \varepsilon \left. \frac{\partial \psi}{dr} \right|_{r=a} \tag{4-30}$$

Using the derivative of equation (4-25), and substituting in equation (4-30) gives:

$$Q_s = 4\pi a^2 \varepsilon \zeta \frac{\left(1+\kappa a\right)}{a} \tag{4-31}$$

The electrical force acting on the particle in an external field E_∞, is given by:

$$F_E = Q_s E_\infty = 4\pi a^2 \varepsilon \zeta E_\infty \frac{\left(1+\kappa a\right)}{a} = 4\pi a \varepsilon \zeta E_\infty \left(1+\kappa a\right) \tag{4-32}$$

The particle will also encounter drag force, as soon as it starts to translate under the influence of the electrical force. Oseen formulation [150] is used here to calculate the velocity field due to a point force acting at a given location in the fluid, and that the overall velocity field due to disturbed point forces is obtained by integrating the singular

solutions of the Stokes equation. Here, the point force is given as the product of the external field, E_∞, and the differential charge, $\partial Q = \rho_f \partial \mathrm{V}$, of a small volume element $\partial \mathrm{V}$ in the fluid. The velocity component acting along the field direction is then given by:

$$U_R = \int_V \frac{E_\infty \rho_f}{8\pi\mu r}\left[1+\cos^2\theta\right]\partial V \tag{4-33}$$

where U_R is the velocity of the center of the spherically symmetric charge cloud, V is the volume of the charge cloud, r is the radial position, and θ is the polar angle. After integration over the entire volume of the charge cloud, one obtains the velocity of the center of the charge cloud as:

$$U_R = -\frac{2}{3}\frac{\varepsilon\zeta}{\mu}\left(\kappa a\right)E_\infty \tag{4-34}$$

This is the retardation velocity of the fluid surrounding the particle, and it approaches zero as $\kappa a \to 0$.

In an infinitely dilute colloidal dispersion, the Stokes hydrodynamic drag force on the spherical particle of radius a is given as:

$$F_H = 6\pi\mu a(U - U_R) \tag{4-35}$$

where $U - U_R$ is the velocity of the particle relative to the electrolyte solution. At steady state, balancing the electrical and drag forces, i.e., $F_E = F_H$, results in

$$U = \frac{2}{3}\frac{\varepsilon\zeta E_\infty}{\mu} \tag{4-36}$$

This is Hückel's [150] solution for the electrophoretic velocity valid for small κa. Equation (4-36) is usually written as:

$$\eta = \frac{U}{E_\infty} = \frac{2}{3}\frac{\varepsilon\zeta}{\mu} \tag{4-37}$$

where η is referred to as the electrophoretic mobility. The Hückel equation is valid for large Debye length and, in particular, for nonelectrolyte systems, e.g., organic liquids, where κ^{-1} is generally large relative to the particle radius, a.

4.3.2 Electrophoresis in the Limit $\kappa a \gg 1$

When the particle radius is large, or more specifically, when the Debye screening length κ^{-1} is small relative to the particle radius, i.e., $\kappa a \gg 1$, the electric double layer becomes extremely thin compared to the particle radius, and we can neglect the curvature effects of the particle. In this limiting case, one can consider the relative movement of the ions with respect to a planar surface. The analysis based on this assumption is generally referred to as the Helmholtz-Smoluchowski analysis.

The governing Navier-Stokes equation for the fluid flow past a horizontal flat surface, with the surface moving at a velocity U is given as:

$$\mu \frac{\partial^2 u_x}{dy^2} = -\rho_f E_\infty \tag{4-38}$$

Here u_x is the velocity of the fluid tangential to the plate. Combining with the Poisson equation, equation (4-38) becomes:

$$\mu \frac{\partial^2 u_x}{dy^2} = \varepsilon E_\infty \frac{\partial^2 \psi_x}{dy^2} \tag{4-39}$$

The boundary conditions for the problem are as follows:

$$\psi \to 0 \quad \text{and} \quad u_x \to -U \quad \text{as } y \to \infty \tag{4-40}$$

$$\frac{\partial \psi}{\partial y} \to 0 \quad \text{and} \quad \frac{\partial u_x}{\partial y} \to -U \quad \text{as } y \to \infty \tag{4-41}$$

$$\psi = \zeta \quad \text{and} \quad u_x = 0 \quad \text{at } y = 0 \tag{4-42}$$

Integrating equation (4-39) from infinity to an arbitrary distance y from the particle surface, and employing the boundary conditions as in equations (4-40) and (4-41) yields:

$$u_x(y) = \frac{\varepsilon E_\infty \psi(y)}{\mu} - U \tag{4-43}$$

Substituting the boundary condition at the particle surface given by equation (4-42) in equation (4-43) results in:

$$U = \frac{\varepsilon E_\infty \zeta}{\mu} \tag{4-44}$$

or, expressed in terms of electrophoretic mobility as:

$$\eta = \frac{U}{E_\infty} = \frac{\varepsilon \zeta}{\mu} \tag{4-45}$$

This is referred to as the Helmholtz-Smoluchowski electrophoretic mobility equation, and is valid in the limit $\kappa a \gg 1$ and $ze\zeta/kT < 1$.

It should be noted that both the Hückel and Helmholtz-Smoluchowski results given by equations (4-37) and (4-45), respectively, provide the two limiting values of the electrophoretic velocity of a single colloidal particle as $\kappa a \to 0$ and $\kappa a \to \infty$, respectively. Note that both of these equations are independent of particle size.

Notably, the two classical analyses (Hückel and Helmholtz-Smoluchowski) discussed above deal with the motion of a spherical particle with uniform surface charge densities under the influence of electric field. However, the great challenge still remains with determining the surface charge densities of most clay minerals by electrophoresis.

From the double layer point of view, the challenge is that most clay minerals are heterogeneous; the basal plane surface or "plates," as well as the "edge" surface carry a non-uniform surface charge which is dependent on pH and salt concentration [24]. Other challenges involve the shapes of the particles, and the fact that some clay types swell by lowering the electrolyte concentration. The shape problem, together with the heterogeneous nature of the charge distribution, makes the interpretation of electrophoretic mobilities in terms of ζ-potential very difficult.

A few researchers have gone beyond and considered nonuniform surface charge densities of particles of different shape such as a sphere [155], spheroid [156], and disc [157], and described the electrophoretic motion for such particles. Due to the extreme complexities of the mathematical equations, analytical solutions for particles of different shape and nonuniform charge densities do not exist. This opens the option for more traditional analyses to characterize the surface charge densities of clays and other differently shaped particles using titration such as potentiometric titration and M-R titration and one new analysis based on surface force measurements using atomic force microscopy, which will be discussed in subsequent sections.

4.4 Results and Discussion

4.4.1 Zeta-Potential of Kaolinite by Electrophoresis

The zeta-potential of kaolinite particles as determined by electrophoresis is shown in Figure 4.4. The zeta-potential of pure silica and alumina particles are also plotted for comparison purposes. As shown, the iso-electric point of kaolinite and pure silica particles is less than pH 3. In fact, the zeta-potential of kaolinite particles is very close to

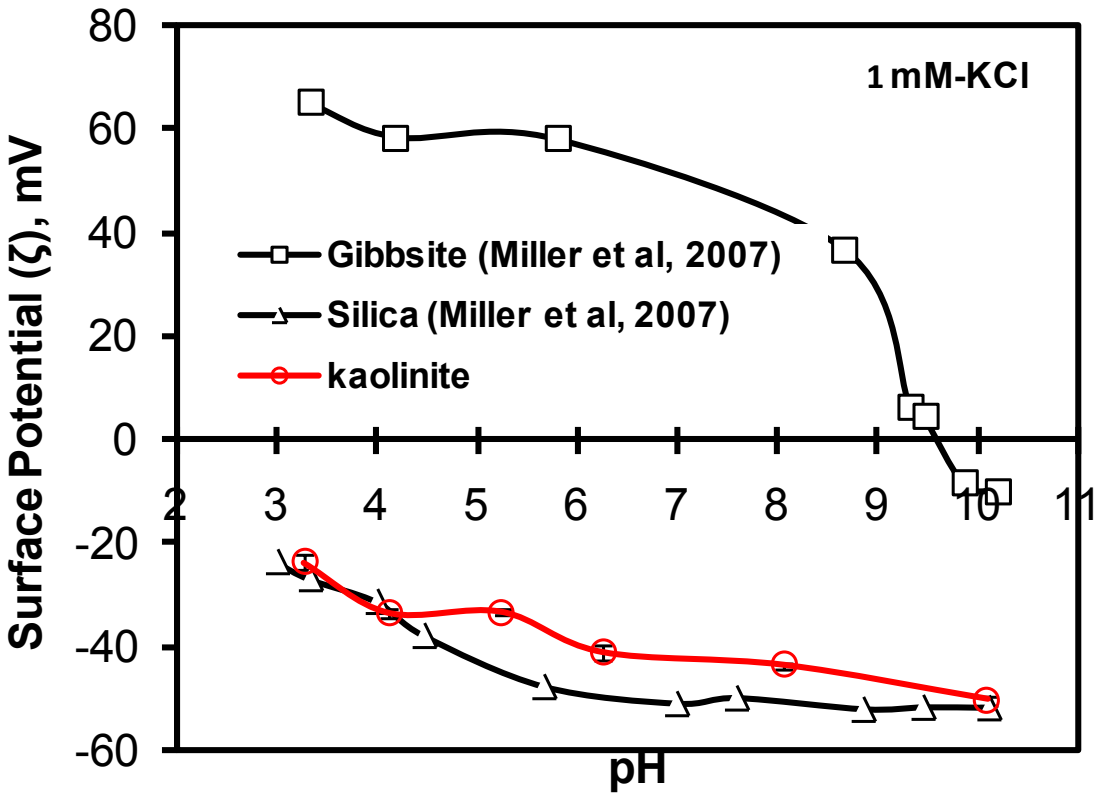

Figure 4.4- Electrophoresis of kaolinite as a function of pH.

pure silica particles as a function of pH. Similar results for the iso-electric point for kaolinite particles at less than pH 3 were reported by several researchers [29, 39-45]. The iso-electric point of gibbsite is at pH 9.2, also in close agreement with the literature [15].

Smith and Narimatsu [39] determined the iso-electric point for kaolinite at pH 2.2 by micro-electrophoresis, and found no iso-electric point for kaolinite by streaming potential. Cases *et al.* [40] reported an iso-electric point at pH 3 for kaolinite particles, and found the sample to spontaneously flocculate at pH < 3.5, and stabilized at pH > 5. Yuan and Pruet [45] also reported the iso-electric point in the range of pH 1.5-3.5 for five commercial kaolinite deposits from Georgia. A few studies have also shown higher iso-electric points for kaolinite, between pH 3 and 4, by electrophoretic measurements [7, 158]

The iso-electric point of kaolinite as determined by electrophoresis is quite intriguing, as one would expect that the kaolinite particles should show the iso-electric point at pH of 5.7 as an average of silica (iso-electric point at pH of 2.2) and gibbsite (iso-electric point at pH of 9.2), since the composition of silica to alumina in kaolinite is nearly 1:1. However, the iso-electric point of kaolinite particles as measured by electrophoresis is consistently less than pH 3, which is more closely related to silica (see Figure 4.4). It appears from the electrophoresis results that the aluminum hydroxide octahedral layer does not contribute to the surface charge properties of kaolinite particles.

We must, however, understand that the zeta potential of kaolinite inferred from the electrophoretic mobility using the Smoluchowski equation has been criticized because of the heterogeneous nature of the surface charge, and the hexagonal platy shape of the particles [15, 24, 46]. The calculation of zeta potential and surface charge densities for

nonspherical kaolinite assuming an equivaent sphere may result in quite misleading values. The zeta potentials calculated from such mobilities does not reflect the potential at the shear plane because of the screening effect of positive charges on the edges relative to those of negative charges at faces, resulting in lower negative mobility [47]. Therefore, other methods for characterizing the surface charge properties of kaolinite must be considered in order to better understand its electrokinetic properties.

4.4.2 Mular-Roberts (M-R) Titration

The change in pH as a function of final pH of kaolinite suspension is shown in Figure 4.5, following the procedure of Mular and Roberts [147]. The iso-electric point (value of final pH where $\Delta pH = 0$) of kaolinite suspension is determined as pH 4.51. Notably, this iso-electric point is higher than that determined by electrophoresis, further supporting that the present electrokinetic theory does not appropriately address the surface charge of anisotropic particles such as kaolinite.

In M-R theory, the ionic strength is increased (increasing concentration of indifferent electrolyte), resulting in a decrease in the double layer thickness of a surface. Thus, the rate of potential decay increases, which causes more potential determining ions to adsorb at the surface when the surface is not at its iso-electric point. As a result, when H^+ or OH^- are dissociated, they induce a change in pH. Korpi [159] points out that an oxide surface has a finite number of adsorption sites capable of reacting with hydrogen and/or hydroxyl ions. When this point is reached, any further addition of acid or base will alter the pH of the suspensions strictly according to the amount added and no further adsorption takes place.

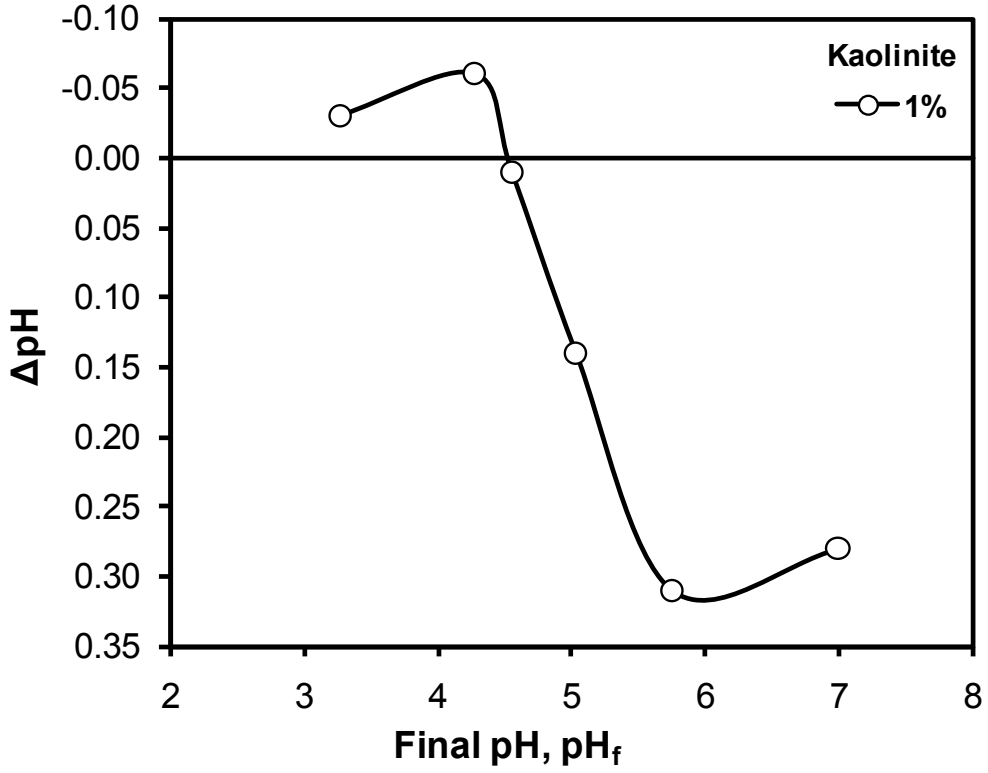

Figure 4.5- Change in pH of the kaolinite suspensions as a function of final pH for kaolinite suspension. Supporting electrolyte (KCl) concentration changes were from 10 to 100 mM.

In view of the above, there must be some $(pH)_i$ in strong acidic or basic suspensions for which the addition of an indifferent electrolyte will result in very small pH shifts. ΔpH approaches zero at these extremes, and represent the iso-electric point. Recently, Alvarez-Silva [160] validated the M-R titration technique with alumina and silica particles. The point of zero charge for alumina and silica particles as determined by the M-R titrations were found to be comparable with the iso-electric point determined by electrophoresis.

4.4.3 Potentiometric Titration

Figure 4.6 presents the surface charge densities of kaolinite as obtained by acid-base potentiometric titrations. The titration curves were corrected for the blank titration conducted in the absence of kaolinite particles. The common intersection point, however, for the two curves at 1 mM and 10 mM was not obtained, but the curves seem to be superimposed well in the pH range of 5-7. The point of zero charge was determined as pH 4.72 and pH 4.45, at 1 mM and 10 mM, respectively. These results are in good agreement with the point of zero charge of kaolinite published in the literature as pH 4.3 [34], pH 4.5 [38] and pH 4.6 [161], as determined by potentiometric titrations. Recently, Brady *et al.* also looked into the dissolution of Si and Al species from kaolinite face surfaces, and found that even at a very low level (< 3 ppm), the surface charge densities of kaolinite particles are impacted significantly [34]. The results are also in good agreement with the point of zero charge of kaolinite of pH 4.51 as determined by M-R titrations, discussed in the previous section.

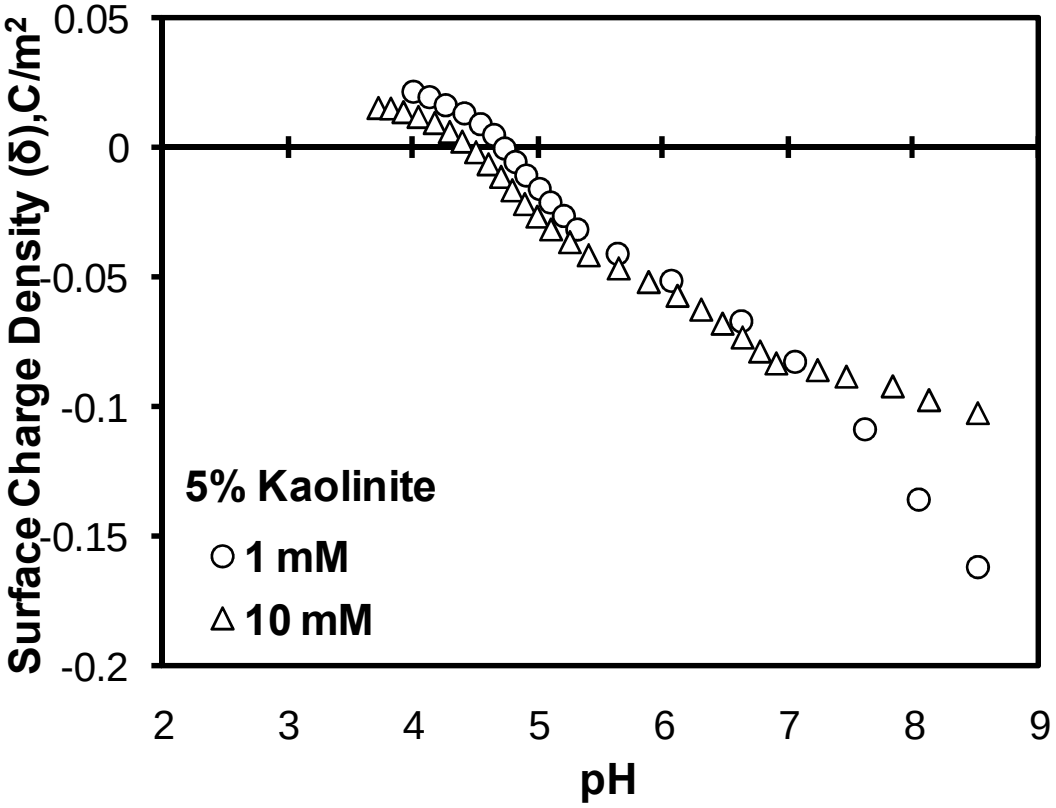

Figure 4.6- Surface charge densities of kaolinite particles as determined by acid-base potentiometric titration.

The potentiometric titrations were also conducted as a function of solid loading, and the results are shown in Figure 4.7. The results indicate that the two curves overlap each other well in the pH region of 5-7, whereas a little deviation exists at low and high pH. The iso-electric point reduced to pH 4.03 for a more concentrated suspension of 10%. This small difference in the iso-electric point of kaolinite could be due to improved aggregation in a concentrated suspension, which could reduce the exposed area of the kaolinite particles.

4.4.4 Zeta-Potential of Kaolinite by Surface Force Measurements

Surface force measurements by atomic force microscopy measure the interaction forces between a silicon nitride tip or colloidal particle of known zeta potential attached to cantilever and the particles of interest as a function of pH of the system. The interaction forces are then fitted to the DLVO model (sum of electrostatic and van der Waal interactions) to predict the surface charge densities and surface potentials of the particles of interest. In this way, the zeta potential or surface charge densities profile of particles as a function of pH of the system can be obtained.

It must be again emphasized here that the classical electrokinetic theory is based on uniformly charged spherical particles which may not be applicable here, as the kaolinite particles are nonspherical platy shaped and carry nonuniform surface charge densities on their faces. In order to gain a better understanding of the surface charge properties of kaolinite particles, we must investigate the surface charge densities on the two basal planes surfaces (the silica tetrahedral layer and the alumina octahedral layer) and edge surfaces. Only recently, Gupta and Miller [72] reported the surface charge

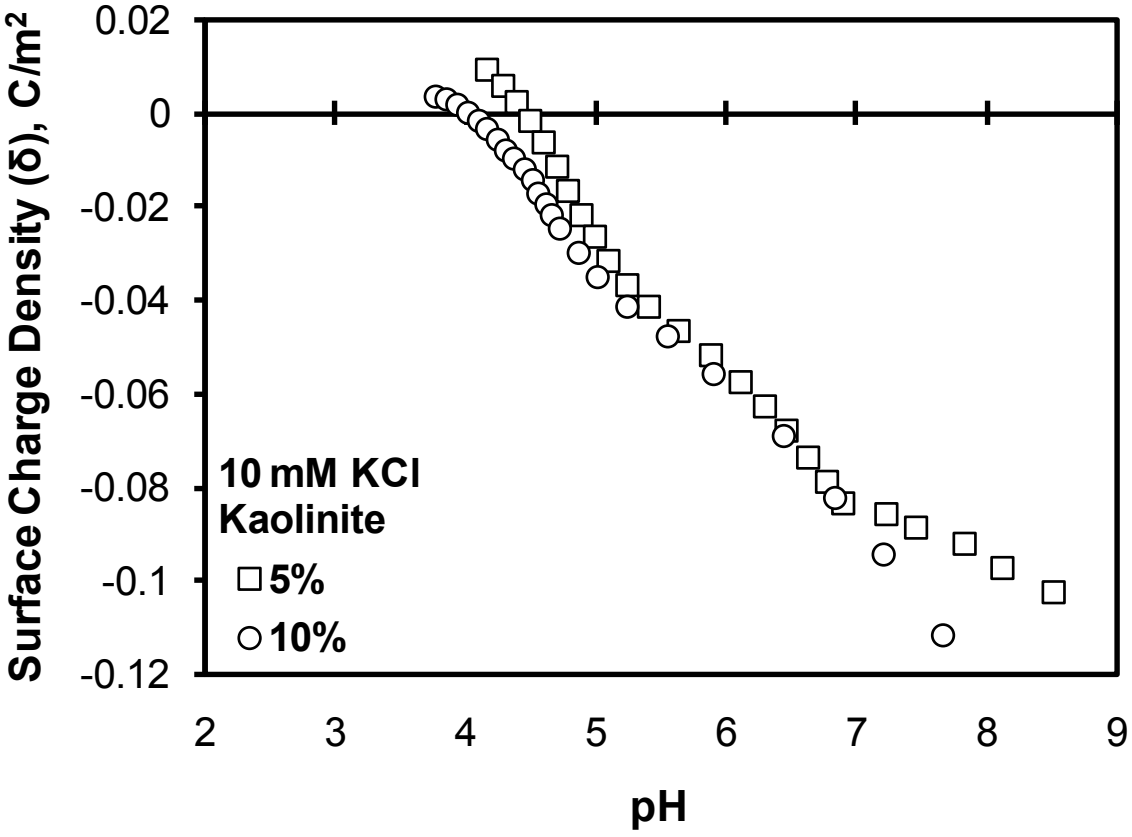

Figure 4.7- Surface charge densities of kaolinite particles as determined by acid-base potentiometric titration applying equation (4-3).

densities of the two basal plane surfaces (the silica and alumina face surfaces) through the surface force measurements of the two faces using atomic force microscopy. They reported that the silica face of kaolinite is negatively charge at pH > 4, whereas the alumina face of kaolinite is positively charged at pH < 6 and negatively charged at pH > 4. Williams and Williams [41] predicted the zeta-potential of edge surfaces of kaolinite with an iso-electric point at pH 7.2, assuming a linear combination of quartz and alumina. It was realized that the zeta-potential does not define the surface potential of the edge surface appropriately. Instead, potentiometric titration was used to determine the surface potential and surface charge of the edge surface of kaolinite. The surface charge density of the edge surface of the kaolinite particles was calculated following the charge balance as:

$$\sigma_{\text{kaolinite}} A_{\text{kaolinite}} = \sigma_{\text{silica face}} A_{\text{silica face}} + \sigma_{\text{alumina face}} A_{\text{alumina face}} + \sigma_{\text{edge face}} A_{\text{edge face}} \qquad (4\text{-}46)$$

where $\sigma_{\text{kaolinite}}$ is the surface charge density of kaolinite particles as determined by potentiometric titration, $\sigma_{\text{silica face}}$ and $\sigma_{\text{alumina face}}$ are the surface charge densities of the silica face and the alumina face of kaolinite as determined by surface force measurements. The symbols $A_{\text{kaolinite}}$, $A_{\text{silica face}}$, $A_{\text{alumina face}}$ and $A_{\text{edge face}}$ represent the total area of kaolinite particles, area of silica face, alumina face and edge surfaces, respectively. The area of the silica face surface, the alumina face surface and the edge surface was determined from the kaolinite particle equivalent circle diameter and thickness.

Utilizing this new information – surface charge densities of the silica, the alumina and the edge surfaces – we can determine the surface charge densities of the kaolinite particles by combining the surface charge densities of each surface with respect to its interaction area, as shown in Figure 4.8. As shown in Figure 4.8, the surface charge density of the edge surface is significantly greater, over one order of magnitude greater when compared to the surface charge densities of the silica face and the alumina face of the kaolinite particles at high pH. At low pH, the surface charge density of the edge face of kaolinite is of a similar magnitude (within a factor of two) with that of the surface charge densities of the silica face and the alumina face. The median diameter and thickness of kaolinite particles were determined as 600 nm and 11.2 nm, respectively, from scanning electron microscopy and atomic force microscopy analysis of 150 kaolinite particles. The composite surface charge of kaolinite particles was then determined and showed an iso-electric point in between pH 4 and 5. This is an interesting result as it showed a higher iso-electric point of less than pH 3 as determined by electrophoresis. This technique of determining the surface charge properties of kaolinite particle is particularly useful, as it also describes the surface charge properties of each surface – the silica face surface, the alumina face surface and the edge surface.

4.4.5 Cation Exchange Capacity (CEC)

The cation exchange capacity of the kaolinite particles is frequently determined to characterize the surface charge properties of its faces – the silica face and the alumina face, whereas the surface charge densities of edges were determined by titration technique (Lyklema, 1995). The maximum number of exchangeable groups can be

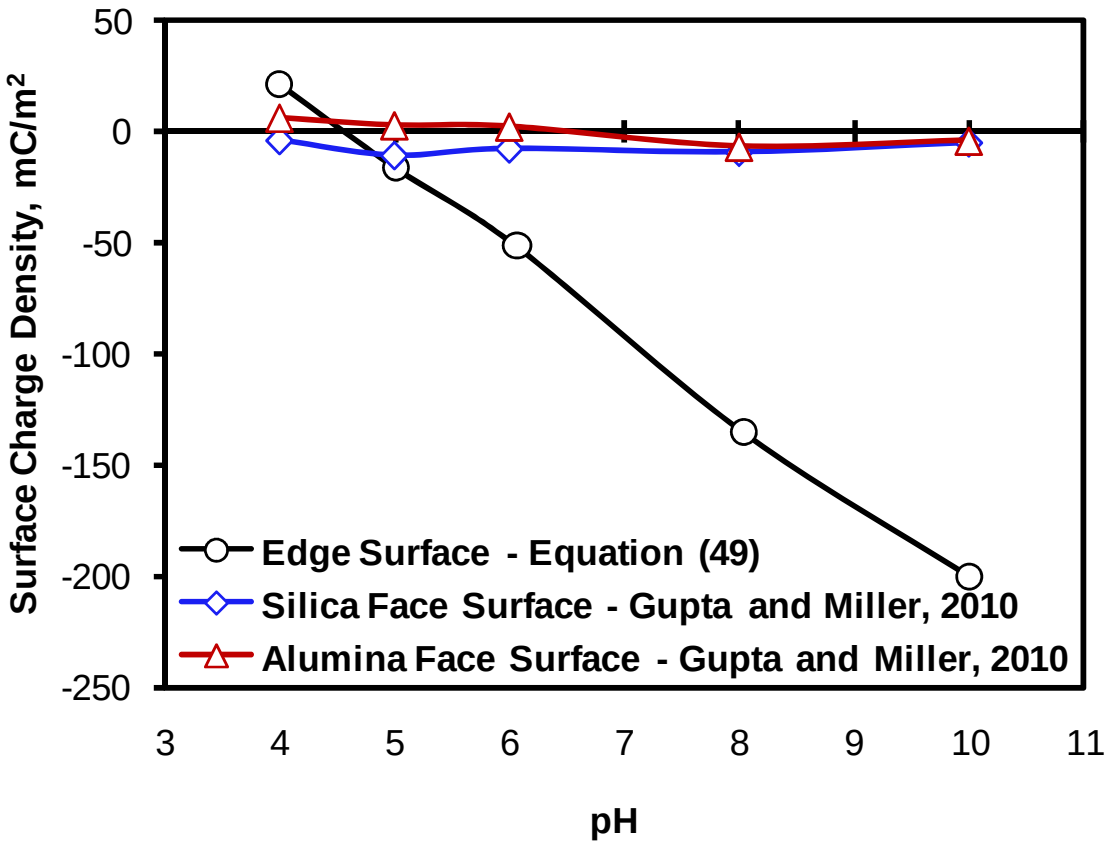

Figure 4.8- The surface charge densities of the kaolinite edge surface and the two face surfaces (silica and alumina face) as a function of pH in 1 mM KCl solution.

established on the silica and the alumina faces of kaolinites by counter ion exchange method.

The cation exchange capacity involves converting the silica and the alumina faces of kaolinite into a state with only one type of counterions (for example, NH_4^+ as in the ammonium acetate method) and then desorbing these quantitatively, measuring how many came off (in the example, by exchange with Na^+ and determining the NH_4^+ liberated by a Kjeldahl distillation). The experiments are normally conducted in acidic condition (where the edge surfaces are positively charged) to exclude adsorption of cations at the edges. Depending on the different counterions and source of kaolinite, different values for cation exchange capacity for kaolinite are suggested in the range of 36-100 μ-mole/g [29-32]. Cation exchange capacities can be utilized to convert to maximum counterions charge density as

$$\sigma_+ = CEC\frac{F}{A_f} \tag{4-47}$$

where CEC is cation exchange capacity, F is the faraday constant and A_f is the specific surface area of the basal planes of silica tetrahedral (001) and alumina octahedral (00$\underline{1}$) layers. The surface charge density of the faces (σ^0) can be obtained from counterions charge density (σ^+) under the conditions where negative adsorption may be neglected. Alternatively, the diffuse layer can be suppressed by working at high electrolyte concentrations. In this way, σ^0 for faces has been established at a value between -0.1 to -0.2 C/m^2 [24].

Gupta and Miller [72], however, disagreed with the traditional emphasis of permanent negative charge on the kaolinite faces (the silica face and the alumina face). As discussed in the surface force section, the silica face of kaolinite is negatively charged at pH > 4, whereas the alumina face of kaolinite is positively charged at pH < 6 and negatively charged at pH > 4. Also, the surface charge on the silica face and the alumina face show dependency on the pH of the system. In agreement of our analysis, Ferris and Jepson [29] also do not support the isomorphous substitution charge on the faces so often assumed in the past. Their data show no evidence for any definite cation exchange capacity for well-crystallized kaolinite from the St. Austell area of Cornwall, and assigned a value of zero for permanent structural charge. Their findings showed that the cation uptake, however, is not fixed and depends upon the cation chosen, the electrolyte concentration and pH, and on whether the experiments were conducted from aqueous or 95% ethanol solvent.

Different electrokinetic techniques were utilized by researchers obtaining a different iso- electric point for kaolinite particles. A review of the literature for the iso-electric point for kaolinite particles is given in Table 4.1. The electrophoresis and electroacoustic analysis gave a smaller value for the iso-electric point for kaolinite as pH < 3 with one exception at pH 3.8 obtained by Hu and Liu [3]. It should be noted that the electrokinetic measurements are questionable as it does not incorporate the platy nature and the heterogeneous nature of differently charged basal plane surfaces and edge surface of kaolinite. Instead, the potentiometric titrations are in general agreement of point of zero charge for kaolinite in between pH 4.5 to 5. The potentiometric titration better

Table 4.1- Review of literature for iso-electric point of kaolinite by different electrokinetic techniques

Method	Value	References
Electrophoresis	< 2	Chassagne *et al.* [52]
	< 2	Sondi *et al.* [51]
	< 3	Tombacz and Szekeres [143]
	< 3	Miller *et al.* [15]
	< 3	Williams and Williams [41]
	3.8	Hu and Liu [3]
Electroacoustic	< 3	Johnson *et al.* [49]
	< 2	Galassi *et al.* [144]
Potentiometric Titration	< 4	Schindler *et al.* [33]
	4.5	Motta and Miranda [38]
	4.5	Xie and Walther [162]
	5.0	Zhou and Gunter [136]
	7.5	Wieland and Stumm [14]
	3.0	Braggs *et al.* [158]
	4.8	Ferris and Jepson [29]
	4.99	Schroth and Sposito[36]

represents the average surface charge properties of kaolinite as it includes the surface charge on the diffuse layer of the particles and not its electrokinetic motion.

4.5 Summary

The surface charge properties of kaolinite particles are manifested in their face surfaces – the silica face, the alumina face and the edge surfaces. The current electrokinetic analysis by electrophoresis does not provide the appropriate surface charge information for kaolinite due to the heterogeneity of the surface charge on the three faces, and the platy nature of particles, which are not accounted in the present theory.

In the absence of an appropriate theory, traditional titration experiments (M-R titration and potentiometric titration) and new surface force measurements by AFM provide more details about the surface charge densities on the three surfaces of kaolinite – the silica face, the alumina face and the edge surface. Both titration experiments estimated a point of zero charge close to pH 4.50 for kaolinite particles, which is in excellent agreement with iso-electric point in between pH 4 and 5, as determined by surface force measurements. The surface force measurement technique is unique in that it provides specific surface charge densities of the silica and the alumina faces of kaolinite as a function of pH. The improvements in kaolinite sample preparation are, however, needed for surface force measurements in order to analyze the surface charge properties of the edge surfaces independently. The electrokinetic properties of kaolinite particles are important and will play a significant role in particle interactions in many different applications such as flotation, filtration, paper making and clay-polymer composites.

CHAPTER 5

PARTICLE INTERACTIONS IN KAOLINITE SUSPENSIONS AND CORRESPONDING AGGREGATE STRUCTURES

The surface charge densities of the silica face surface and the alumina face surface of kaolinite particles, recently determined from surface force measurements using atomic force microscopy, show a distinct dependence on the pH of the system. The silica face was found to be negatively charged at pH > 4, whereas the alumina face surface was found to be positively charged at pH < 6, and negatively charged at pH > 8. The surface charge densities of the silica face and the alumina face were utilized in this study to determine the interaction energies between different surfaces of kaolinite particles.

Results indicate that the silica face–alumina face interaction is dominant for kaolinite particle aggregation at low pH. This face–face association increases the stacking of kaolinite layers, and thereby promotes the edge–face (edge–silica face and edge–alumina face) and face–face (silica face–alumina face) associations with increasing pH and hence, the maximum shear yield stress at pH 5-5.5. With further increase in pH, the face–face and edge–face association decreases due to increasing surface charge density on the silica face and the edge surfaces, and decreasing surface charge density on the

alumina face. At high pH, all kaolinite surfaces become negatively charged, kaolinite particles are dispersed and the suspension is stabilized. The face–face association at low pH has been confirmed from cryo-SEM images of kaolinite aggregates taken from suspension which show that the particles are mostly organized in a face–face and edge–face manner. At higher pH conditions, the cryo-SEM images of the kaolinite aggregates reveal a lower degree of consolidation and the edge–edge association is evident.

5.1 Introduction

The rheological properties of concentrated suspensions of clay minerals such as kaolinite [$Al_2O_3.2SiO_2.2H_2O$] are very important in ceramics, in paper and pulp, in drilling mud, in filtration, in dewatering and in many other new applications such as clay-polymer nanocomposites etc. [53, 63, 116]. Kaolinite particles are naturally pseudo-hexagonal platy shaped ranging from micron to nanosize particles. The crystallographic structure suggests that kaolinite particles consist of a silica tetrahedral surface corresponding to the 001 basal plane and an aluminum hydroxide octahedral surface corresponding to the 00$\underline{1}$ basal plane, as shown in Figure 5.1. Of course, the kaolinite particles have 010 and 110 edge surfaces which are generated as a result of broken covalent bonds. The rheological properties of kaolinite are governed by its surface chemistry, in particular its electrokinetic features, which generally determine the particle interactions and hence, the mechanical properties of the suspension.

It is traditionally believed that the 001 and 00$\underline{1}$ basal plane surfaces of kaolinite particles are negatively charged due to isomorphic substitution of Al^{3+} for Si^{4+} in the silica tetrahedral layer and Mg^{2+} for Al^{3+} in the alumina octahedral layer, whereas

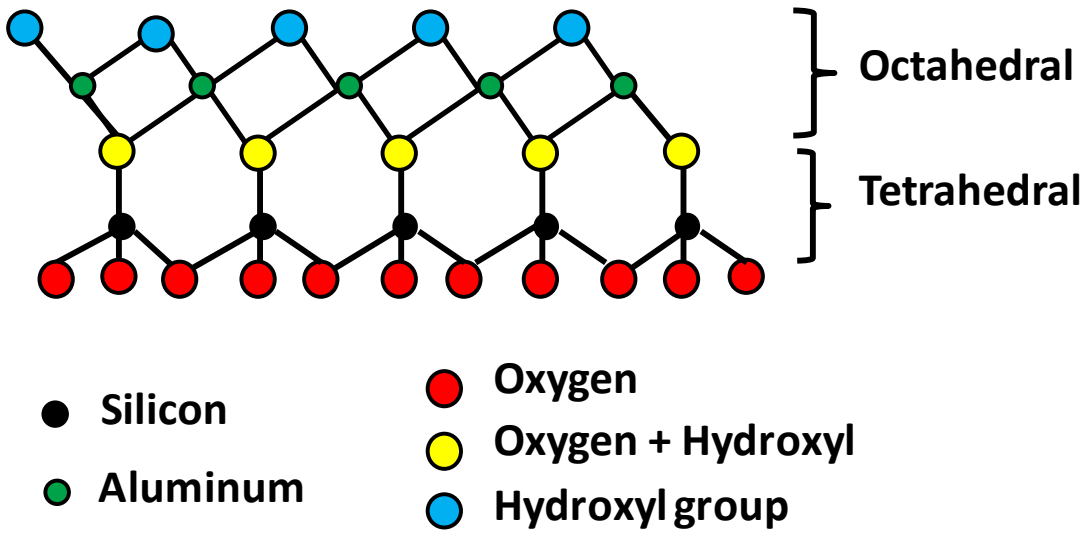

Figure 5.1- The structure of kaolinite along 010 edge surface showing a silica tetrahedral layer and an alumina octahedral layer.

the edge surface (010 and 110 plane surfaces) carries a positive or negative charge depending on the pH of the system [23, 26, 48-50, 142]. Following this assumption, several researchers have defined the rheological properties of kaolinite, and have explained the abnormal behavior of a maximum yield stress for kaolinite suspensions at pH 5-5.5 [26, 48-50]. Such a maximum might be expected at kaolinite's iso-electric point of pH < 3 [51, 52]. Johnson *et al.* [49, 50] have gone further in their analysis and explained this abnormal rheological behavior based on the aggregation behavior of kaolinite particles, which is described mainly by edge–face attractions and some face–face attractions. On this basis, the maximum shear-yield stress at pH 5.5 shown in Figure 5.2 was explained.

The assumption that both basal planes carry a fixed negative charge has only recently been examined experimentally through surface force measurements using atomic force microscopy (AFM) [72]. These colloidal force measurements reveal that the silica tetrahedral face of kaolinite is negatively charged at pH > 4, whereas the alumina octahedral face of kaolinite is positively charged at pH < 6, and negatively charged at pH > 8. The results suggest that the iso-electric point of the silica tetrahedral face is at pH < 4, and that the iso-electric point of the alumina octahedral face lies between pH 6 and 8 [72]. Based on this new finding, Gupta *et al* .[163] determined the interaction energies between different surfaces of kaolinite particles, which showed that the silica face–alumina face association is likely to be dominant for kaolinite particle association at low and intermediate pH conditions. However, the above conclusion of dominant silica face–alumina face association was reached by assuming that the zeta-potential of the edge was a linear combination of the zeta-potentials on silica and alumina surfaces [41].

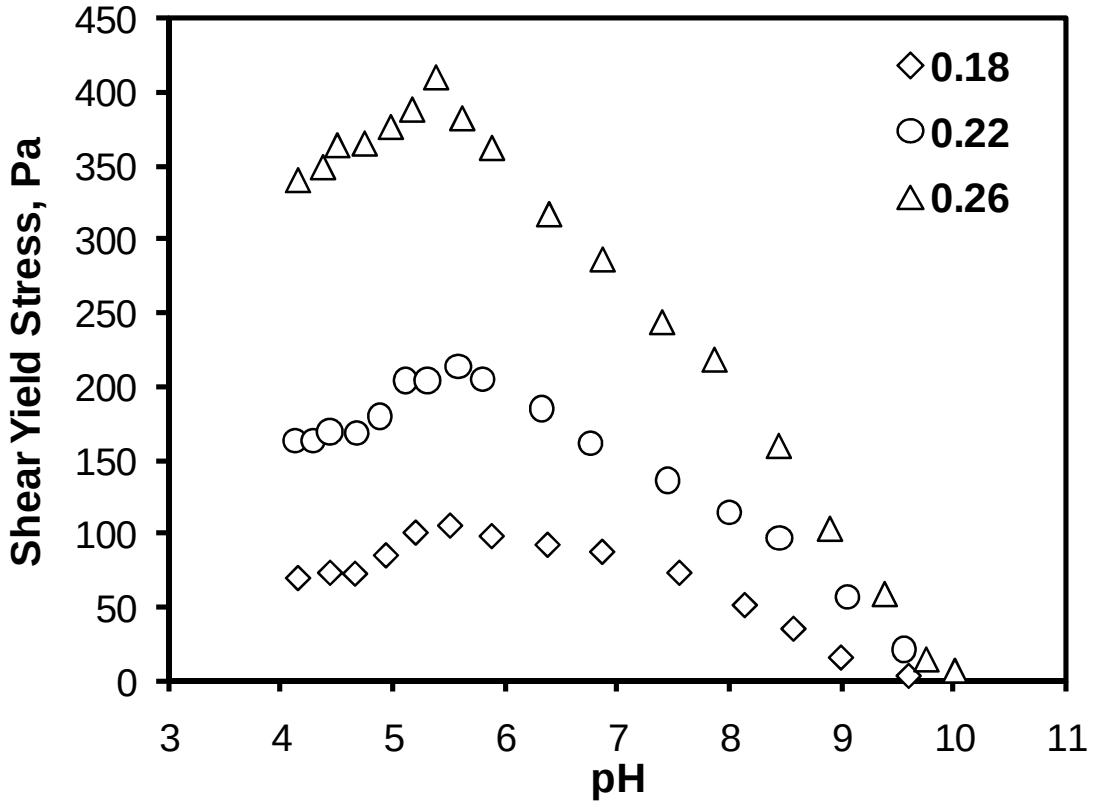

Figure 5.2- Shear yield stress of kaolinite suspensions as a function of pH for selected volume fractions (adapted from Johnson *et al.* [49, 50]).

The assumption for edge surface zeta-potential will be discussed later in this study. It seems that the edge surface zeta-potential for kaolinite is under-estimated, and that an experimental technique such as potentiometric titration should be considered in the analysis of kaolinite surface potentials.

Several researchers have examined images of flocculated kaolinite suspensions using electron microscopy to determine the aggregate structure, and relate these observations to rheological properties. The earliest significant discussion of clay fabric was given by Terzaghi in 1925 (see O'Brien [164]) in which the structure of cohesive soils was discussed with regards to adhesion between adjacent minerals. Casagrande [165] presented a theory for a honeycomb structure in soils. Idealized drawings of clay fabric forming a card-house or honeycomb structure have been proposed [16, 23, 166, 167]. Rosenqvist [168, 169] published the first electron micrograph of freeze-dried samples of undisturbed marine Oslo blue clay and supported the idea of card-house arrangement in the undisturbed sediment. O'Brien [164] examined the fabric of kaolinite in distilled and slightly saline water, and found that the fabric is dominated by a 3-dimensional network of twisted chains of face–face oriented flakes having the appearance of a stair-stepped cardhouse. Recently, Zbik *et al.* [170] investigated the structure of kaolinite aggregates at pH 8 during sedimentation experiments using cryogenic-scanning electron microscopy (cryo-SEM). They found that the kaolinite aggregates initially show edge–face and edge–edge association, which rearranges from edge–edge chains to more compact face–face associations during settling. In another study, Zbik and Frost [171] observed differences in the physical behavior of a number of kaolinite clays from Birdwood and Georgia. For example, SEM micrographs of the Birdwood kaolinite

aggregates show the predominance of stair step edge–edge contacts forming a spacious cell structure, whereas Georgia kaolinite aggregates display edge–face contacts building a card-house structure. From these studies, it is suggested that kaolinite clays are very complex and each kaolinite should be considered separately. It is evident that each kaolinite from different sources must be characterized and detailed examination may be necessary to determine the aggregate structures at low, medium and high pH values.

It is the objective of this chapter to utilize the surface charge information on the face surfaces and edge surfaces of kaolinite in order to understand the structure of kaolinite suspensions and corresponding rheological behavior. Furthermore, the influence of particle aspect ratio and electrical double layer thickness is investigated with regard to the aggregation behavior of kaolinite particles. Finally, cryo-SEM images were used to examine the modes of particle association (face–face, edge–face, and edge–edge).

5.2 Materials and Methods

5.2.1 Sample Preparation

A clean English Kaolin (Imerys Inc., UK) was obtained from the St. Austell area in Cornwall, UK. The sample was cleaned with water only using elutriation to achieve classification at a size of less than 2 μm. No other chemical treatment was used. Further details about the kaolinite extraction and preparation are given in the literature [124]. The kaolinite suspension was prepared in high purity Milli-Q water (Millipore Inc.). The resistivity of the water was 18.2 MΩ-cm in all experiments. Potassium chloride (1 mM solution) was used as background electrolyte for surface force measurements. The pH

was adjusted to its desired value using 0.1 M HCl or 0.1 M KOH solutions. All chemicals used were of ACS reagent grade.

X-ray diffraction (Bruker AXS, Inc., Madison, WI, USA) analysis conducted on the kaolinite sample confirmed that kaolinite is the dominant mineral phase. Energy dispersive X-ray spectroscopy (FEI, Hillsboro, Oregon, USA) analysis of the kaolinite sample showed nearly 1:1 atomic distribution of aluminum (7.98%) and silicon (7.95%) with trace amounts of potassium (0.35%), calcium (0.08%) and iron (0.15%). Other details about the purity of kaolinite are provided elsewhere [72].

The kaolinite particles with a median diameter of 600 nm and median thickness of 11.2 nm in 1 mM KCl solution were used in this study, unless otherwise mentioned. The median diameter and thickness were determined from the imaging of at least 150 kaolinite particles using atomic force microscopy. The kaolinite particles were air-dried on a thin sheet of mica and an image of the particle was obtained using the contact mode imaging technique. Section analysis was then conducted to obtain information about the diameter and thickness of the particle.

5.2.2 Aggregate Size

The aggregate size of kaolinite particles in suspension at desired pH values was determined using photon correlation spectroscopy (PCS). In a PCS experiment, the fluctuation of scattered light from the particles by their Brownian motion is collected at a scattering angle of 90° by an optical fiber, and detected by a photo-electric detector. The amplified signal from the photo-electric detector is fed into an autocorrelator for computing the intensity autocorrelation function. This autocorrelation function is used to

determine the relaxation of intensity fluctuations, which in turn is related to translational diffusion coefficient of the particles. Particle size (equivalent spherical diameter) is then determined from the diffusion coefficient of the particles.

Kaolinite suspensions (4%) were prepared in 1mM KCl solution at pH 9.0, sonicated for 5 minutes and stirred for 1 hour for complete dispersion. After conditioning, 50 mL of the suspensions was taken in a volumetric flask and adjusted to the desired pH of 3, 5, 7 and 9. A small amount of kaolinite suspensions (1 mL) was taken at each pH into a cuvette for PCS analysis. Each experiment was replicated three times and the average aggregate size was determined.

5.2.3 Cryo-SEM

Kaolinite suspensions (1%) were prepared in 1 mM KCl solution (100 mL). About 15 ml of the sample was taken in a vial and adjusted to pH 3, 5, 7 and 9 using 0.1 M HCl or 0.1 M KOH solutions. The suspension was left overnight for conditioning. The sample was hand-shaken, and then a few microliters of the suspension were taken in a small metal rivet sealed with glue at one end. The sample was immediately plunged into a liquid N_2 slush using the Oxford LN_2 slush freezing apparatus for freezing the water without allowing crystallization, i.e. vitrifying. Vitrified samples were placed onto the liquid nitrogen-cooled specimen stage of the field emission scanning electron microscope Philips XL30 FESEM with Oxford CT 1500 Cryo stage. The sample was fractured under vacuum and a small amount of vitrified H_2O was sublimed off by raising the stage temperature to $-90\ ^{\circ}C$ for 10 minutes to expose the aggregate structure, then lowering back to $-180\ ^{\circ}C$. Finally, the sample was coated with platinum before SEM imaging.

5.2.4 DLVO Model

Interactions between kaolinite particles were characterized by the (Derjaguin-Landau-Vervey-Overbeek) DLVO model, which considers the sum of electrostatic and van der Waals forces. An appropriate form for the van der Waals interaction energy per unit area (E^{vdW}) between two planar surfaces of thickness δ_1 and δ_2 is given as [150]

$$E^{vdW} = -\frac{A_H}{12\pi}\left[\frac{1}{h^2} + \frac{1}{\left(h+\delta_1+\delta_2\right)^2} - \frac{1}{\left(h+\delta_1\right)^2} - \frac{1}{\left(h+\delta_2\right)^2}\right] \tag{5-1}$$

where A_H is the combined Hamaker constant of the two surfaces interacting in the suspending medium and h is the shortest separation distance between two interacting particles. At the closest approach, h was taken as 20 Å in all calculations for comparison with existing literature [49]. In the case of kaolinite, we have to consider six different surfaces for particle interaction, edge–edge, edge–silica face, edge–alumina face, silica–silica face, alumina–alumina face and silica face–alumina face interactions. Therefore, the nonretarded Hamaker constants for each of the six cases were determined from the Hamaker constant of silica and alumina as given in Table 5.1. Hamaker constants in the Table 5.1 were calculated from the following equation:

$$A_{123} = \left(\sqrt{A_{11}} - \sqrt{A_{33}}\right)\left(\sqrt{A_{22}} - \sqrt{A_{33}}\right) \tag{5-2}$$

where A_{11} is the Hamaker constant for the first interacting surface, for example the silica face, alumina face or edge surface; A_{22} is the Hamaker constant for the second

Table 5.1- Hamaker constant for different interactions between kaolinite particles

Interaction	**Interaction Type**	**Hamaker Constant, J**
1	Edge–Edge	2.37×10^{-20}
2	Edge–Silica Face	1.63×10^{-20}
3	Edge–Alumina Face	3.05×10^{-20}
4	Silica Face–Silica Face	1.11×10^{-20}
5	Alumina Face–Alumina Face	3.90×10^{-20}
6	Silica Face–Alumina Face	2.08×10^{-20}

interacting surface, for example the silica face, alumina face or edge surface; and A_{33} = the Hamaker constant for the suspending medium which in our study is water. The Hamaker constants for silica and alumina were taken as 8.86×10^{-20} J and 1.52×10^{-19} J, respectively [130]. The Hamaker constant for the edge surface was determined as 1.20×10^{-19} J from the average of the Hamaker constants for silica and alumina. The Hamaker constant for water was taken as 3.70×10^{-20} J [130].

The electrical double layer interaction energy per unit area (E^{Edl}) between two planar surfaces with surface potentials ψ_1 and ψ_2 is given by the Hogg-Healy-Fuerstenau (HHF) expression for dissimilarly charged surfaces as [172]

$$E^{Edl} = \varepsilon\epsilon_0\kappa\left[\frac{2\psi_1\psi_2 exp(\kappa h) - \psi_1^2 - \psi_2^2}{exp(2\kappa h) - 1}\right] \tag{5-3}$$

where ε_o is is the permittivity of free space, ε is the dielectric constant and κ^{-1} is the Debye screening length of the electrical double layer.

For cases when the surface potential of the two planar surface are similar, i.e., $\psi_1 = \psi_2 = \psi$, the electrical double layer interaction energy reduces to

$$E^{Edl} = \frac{2\psi^2\varepsilon\epsilon_0\kappa}{exp(\kappa h) + 1} \tag{5-4}$$

Similarly, the electrical double layer interaction energy under the condition of constant surface charge, first established by Langmuir28, can be used. In this case,

revising equation (3) by replacing the two minus signs in the numerator by plus signs gives the Langmuir equation. In particular, the double layer interaction energy at constant surface potential and/or constant surface charge presents the lower and upper limits of the interaction energy. The actual double layer interaction energy with a mixed boundary condition or a surface charge regulation is between the two limits. The calculation shows that the trend of the total interaction energy for the cases is similar. Therefore, only the interaction energy described by equation (5-3) is used hereafter. The resulting DLVO interaction energy is given as:

$$E = E^{vdW} + E^{Edl} \tag{5-5}$$

The total interaction energy was multiplied by the measured interaction area ratio of basal plane surface to edge surface of 13.39:1 as determined by atomic force microscopy. In calculating the edge and face surface areas, the kaolinite particle was assumed to be a circular disc. The energies are scaled against the maximum predicted silica face-alumina face interaction energy, E_{max}.

5.3 Results and Discussion

The rheological behavior of a suspension is essentially determined by the forces that control the spatial arrangement and dynamics of the suspended particles. In a suspension under the predominant influence of repulsive electrostatic energies, the particles tend to take up positions as far from each other as possible. This may lead to a regular arrangement of the particles, i.e., to the development of the spatial order in the

suspension. Clusters of particles, or aggregate structures, form in a suspension when the particle interactions are dominated by attractive energies. The aggregate structure or flocs will immobilize the suspending medium, and give rise to increasing viscosity and yield strength of the suspension. The particle characteristics such as morphology, size, surface area etc. will also greatly affect the suspension viscosity, and the strength of the aggregate structure. The aggregate structure plays a major part in the flow behavior of clay suspensions. The rate and mechanism of formation of such aggregate structures and the characteristics of the aggregate structures are therefore important parameters to describe the rheological characteristics of such suspensions. In this study, we will discuss the formation of aggregate structures of kaolinite and their validation by cryo-SEM in the following and subsequent sections.

5.3.1 Particle Interactions

As mentioned previously, the surface chemistry and rheology of kaolinite particles is complicated greatly by the nonuniform surface charge densities on edge and face surfaces. It was realized that electrophoretic measurements of kaolinite particles do not give detailed information about surface charge characteristics, and therefore information on electrophoretic mobility is not used in this analysis [15]. Instead, surface charge densities of the two faces of kaolinite particles (silica face and alumina face) determined from surface force measurements are used in this analysis [72]. Recently, Gupta *et al.* [163] used the zeta-potential for the edge surfaces as a linear combination of the zeta-potential of silica and alumina particles. It was realized that the zeta-potential does not define the surface potential of the edge surface appropriately. Instead,

potentiometric titration was used to determine the surface potential and surface charge of the edge surface of kaolinite. The surface charge density of the edge surface of the kaolinite particles was calculated following the charge balance as:

$$\sigma_{\text{kaolinite}} A_{\text{kaolinite}} = \sigma_{\text{silica face}} A_{\text{silica face}} + \sigma_{\text{alumina face}} A_{\text{alumina face}} + \sigma_{\text{edge face}} A_{\text{edge face}} \quad (5\text{-}6)$$

where $\sigma_{\text{kaolinite}}$ is the surface charge density of kaolinite particles as determined by potentiometric titration, $\sigma_{\text{silica face}}$ and $\sigma_{\text{alumina face}}$ are the surface charge densities of the silica face and the alumina face of kaolinite as determined by surface force measurements. With this information, the surface charge densities of the edge surface of kaolinite was determined, and the results are presented in Figure 4.8. As shown in Figure 4.8, the surface charge density of the edge surface is significantly greater, over one order of magnitude greater when compared to the surface charge densities of the silica face and the alumina face of the kaolinite particles at high pH. At low pH, the surface charge density of the edge face of kaolinite is of a similar magnitude (within a factor of two) with that of the surface charge densities of the silica face and the alumina face.

Considering the surface charge data provided for the different faces of kaolinite, the net interaction energy between different surfaces of kaolinite was determined and is shown in Figure 5.3. The interaction energies were scaled to maximum attractive interaction energy determined for silica face–alumina face, and multiplied by the average interaction area ratio of 13.39:1 [163]. Figure 5.4 shows the scaled interaction energies calculated for a separation distance, h = 20 Å, when there is no energy barrier, consistent with previous studies [49]. When there is an energy barrier between surface interactions,

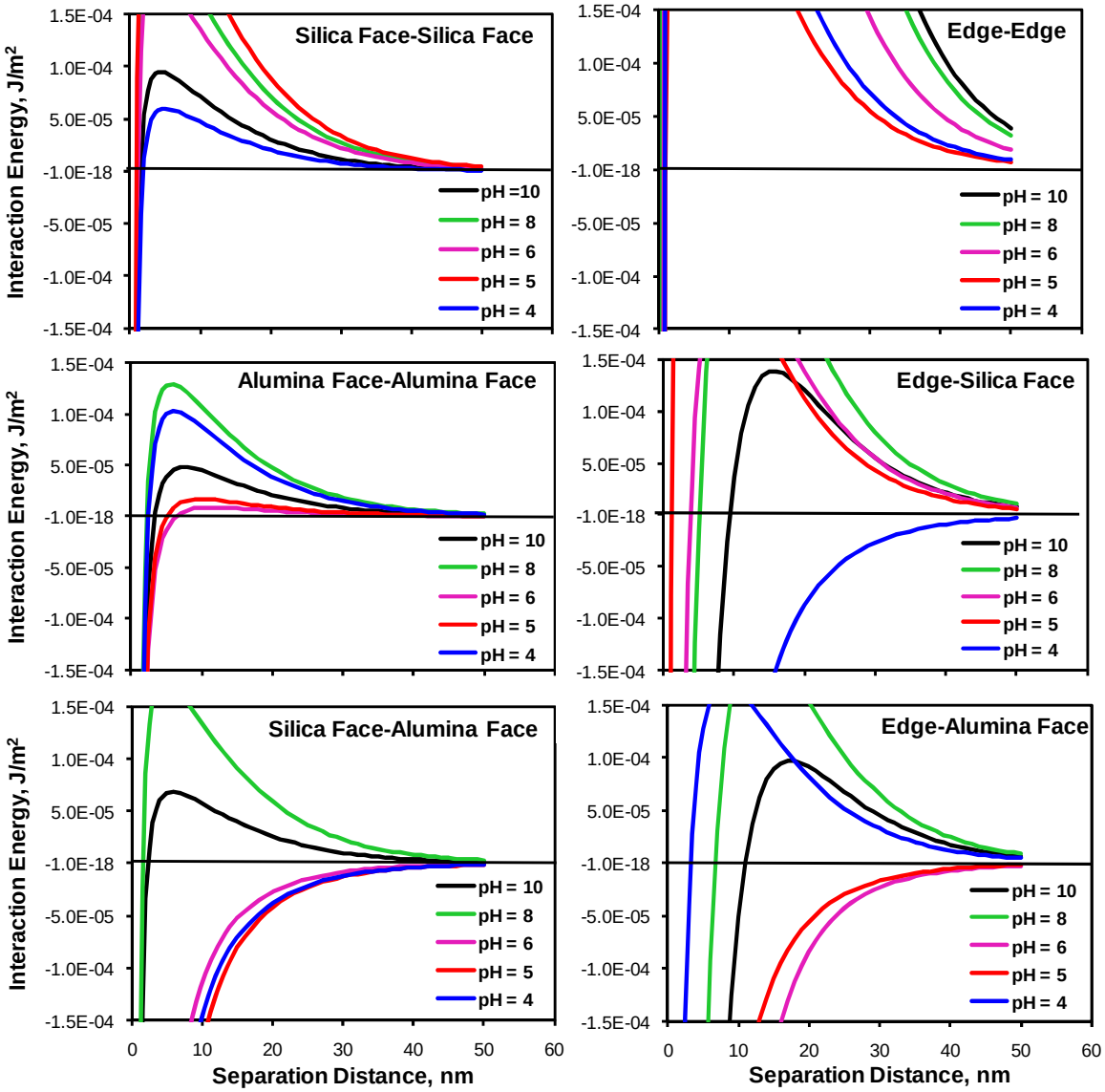

Figure 5.3- Interaction energy profiles for different surface interactions of kaolinite particles.

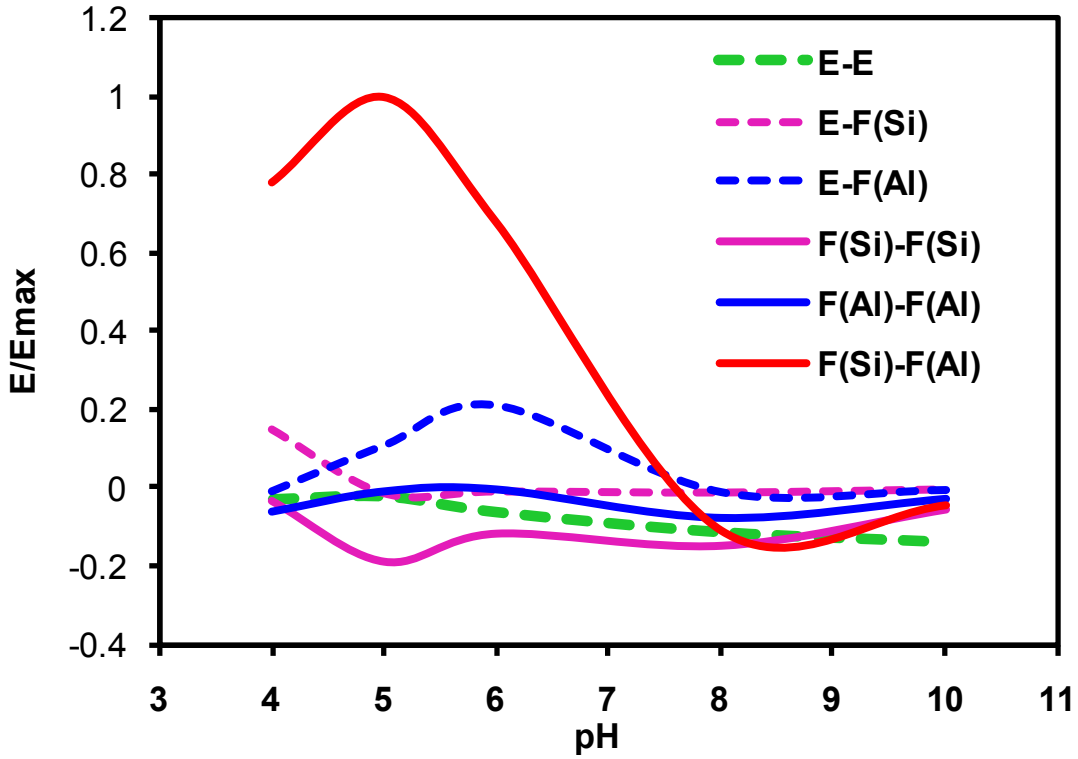

Figure 5.4- The predicted kaolinite edge–edge, edge–silica face (E-F(Si)), edge–alumina face (E-Al(Si)), silica face–silica face (F(Si)-F(Si)), alumina face–alumina face (F(Al)-F(Al)), and silica face–alumina face (F(Si)-F(Al)) interaction energies scaled to maximum attractive energy for the silica face–alumina face interaction. Kaolinite particles with diameter 600 nm and thickness 11.2 nm in 1 mM KCl solution.

the interaction energies were calculated at the separation distance for the maximum energy barrier.

It is evident that the silica face–silica face interaction is repulsive in the pH range of 4–10 due to the strong electrostatic repulsion between negatively charged silica faces (see Figure 5.3 and Figure 5.4). The alumina face–alumina face interactions showed a slight repulsion with a small energy barrier at pH 6 due to weak electrostatic repulsion and stronger van der Waals attraction. Below pH 7.5, the silica face–alumina face interaction is attractive with a maximum at pH 5, whereas a slight repulsion was observed at higher pH (pH > 7.5). This is due to the opposite sign of the surface charge densities for the silica face and alumina face at pH $\leq$ 6 (silica face is negatively charged and alumina face is positively charged), causing stronger attraction both electrostatic and van der Waals attraction (see Figure 5.3 and Figure 5.4). At higher pH (pH $\geq$ 8), both the silica face and alumina face carry the same surface charge sign (both silica and alumina face carry negative charge), and hence a slight repulsive electrostatic interaction was found. The edge–edge surfaces showed repulsive interaction for the entire pH range, due to the similar nature of surface charge, i.e., edge surfaces carry a positive surface charge at pH 4, which becomes increasingly negative at pH values greater than 5 (see Figure 4.8). The edge–alumina face showed repulsive interactions at low pH (pH of 4) and at high pH (pH $\geq$ 8) due to strong electrostatic repulsive interactions, whereas an attractive interaction was found at an intermediate pH of 5-6. In contrast, the edge–silica face showed attractive interaction only at low pH 4 and repulsion at a higher pH (pH $\geq$ 5), due to the similar nature of the surface charge on the edge surface and the silica face of kaolinite at higher pH. The edge–silica face and edge–alumina face interactions indicate

that the edge–face interactions are favorable at pH < 8. Though the magnitude of edge–silica face and edge–alumina face interactions suggest an insignificant interaction on an interaction area basis, the interaction cannot be ignored as the edge effect could become significant in concentrated suspensions when the kaolinite particles are stacked due to the silica face–alumina face interaction.

On the basis of these different interactions shown in Figure 5.3 and Figure 5.4, it is expected that the overall interaction of kaolinite particles will be dominated by silica face–alumina face in acidic solutions (pH < 7.5). However, the alumina face–alumina face interactions are unfavorable over the entire pH range of the system. Although lower in magnitude, the edge–silica face showed favorable interaction at low pH of 4 and therefore, some edge–face associations will also be expected at low pH. It is therefore anticipated that the kaolinite particles will aggregate initially in a silica face–alumina face manner forming a lamellar tactoid structure in kaolin suspensions at low pH values [23]. This results in a lower suspension shear yield stress. As the pH rises, the face–face association will grow, causing the formation of tactoids with thicker edge surfaces, thereby promoting the edge–face association. This is supported by Secor and Radke [173] who found by numerical simulation that the electrostatic field from the basal plane may "spill-over" to dominate the positive edge surface. Chang and Sposito [174] also showed that the negative electric field from the basal plane of a disc-shaped clay mineral particle near the edge surface is mainly controlled by particle thickness. This face–face association is found to be dominant at pH 5, and edge–face associations dominant at pH 6, which corresponds to the maximum shear yield stress at pH 5-5.5. As the pH is increased further, the face–face and edge–face association decreases due to lower

magnitude of surface charge density on edge surfaces and face surfaces, resulting in lower shear yield stress. At high pH, the edge–face and face–face interaction forces become repulsive, and the system becomes completely dispersed, and a negligible shear yield stress is measured. In this way, the maximum shear yield stress at pH 5.5 can be explained based on particle aggregation and its variation with system pH. Even if the edge surface charge density and corresponding interactions are based on zeta potential measurements as dismissed at the beginning of this section on particle interactions, the relative significance of some interactions changes but in general, the same conclusion is found regarding the variation of interactions with pH.

O'Brien [164] observed the dominant face-face and some face-edge aggregation behavior of kaolinite both in distilled water and in electrolyte solutions using scanning electron microscopy of freeze-dried kaolinite samples. However, concern was raised that the freeze-drying technique can alter the structure of these aggregates during drying. Recently, Zbik *et al.* [170] observed stacks of kaolinite aggregated dominantly in face-face manner at pH 8 using cryo-vitrified technique with scanning electron microscopy. The authors could not explain the face–face type interaction based on the assumption that 001 and 00$\underline{1}$ faces of kaolinite are negatively charged. Instead, it follows from our new results that the kaolinite particles are aggregating according to silica face–alumina face and alumina face–alumina face interactions.

In contrast to our results, Johnson *et al.* [49, 50] predicted that the kaolinite particles will mostly interact in an edge–face manner at lower pH. However, their studies were based on the assumption that both faces of kaolinite are negatively charged, which analysis must be reconsidered in view of the AFM surface force results reported by Gupta

and Miller [72]. These different surface interactions are of importance in order to control the aggregation behavior of kaolinite particles, and the mechanical properties of such suspensions.

5.3.2 Influence of Aspect Ratio

The influence of aspect ratio (ratio of particle diameter to thickness) on the different surface interactions is shown in Figure 5.5. The aspect ratio was determined from the atomic force microscopy images of kaolinite particles. About 150 particles were imaged and analyzed using Nanoscope V7.2 software for the atomic force microscope (Veeco Instruments Inc., Santa Barbara, CA). As shown, the edge–silica face and edge–alumina face interactions are significant for particles with a low aspect ratio (9) as compared to particles with a high aspect ratio (165). Notably, the edge–alumina face interactions are dominant at pH 6, whereas silica face–alumina face interactions are dominant at pH 5 for kaolinite particles with low aspect ratio. This is particularly interesting as significant edge–face interaction for particles with a low aspect ratio indicates that particles will orient themselves in both edge–face and face–face (silica face–alumina face) organizations. The particles with high aspect ratio will orient themselves dominantly in a face–face manner (silica face–alumina face). It is shown that the aggregate structures can be expected to depend on the aspect ratio of kaolinite particles and thereby, the mechanical properties of the kaolinite suspensions will be affected by the aspect ratio.

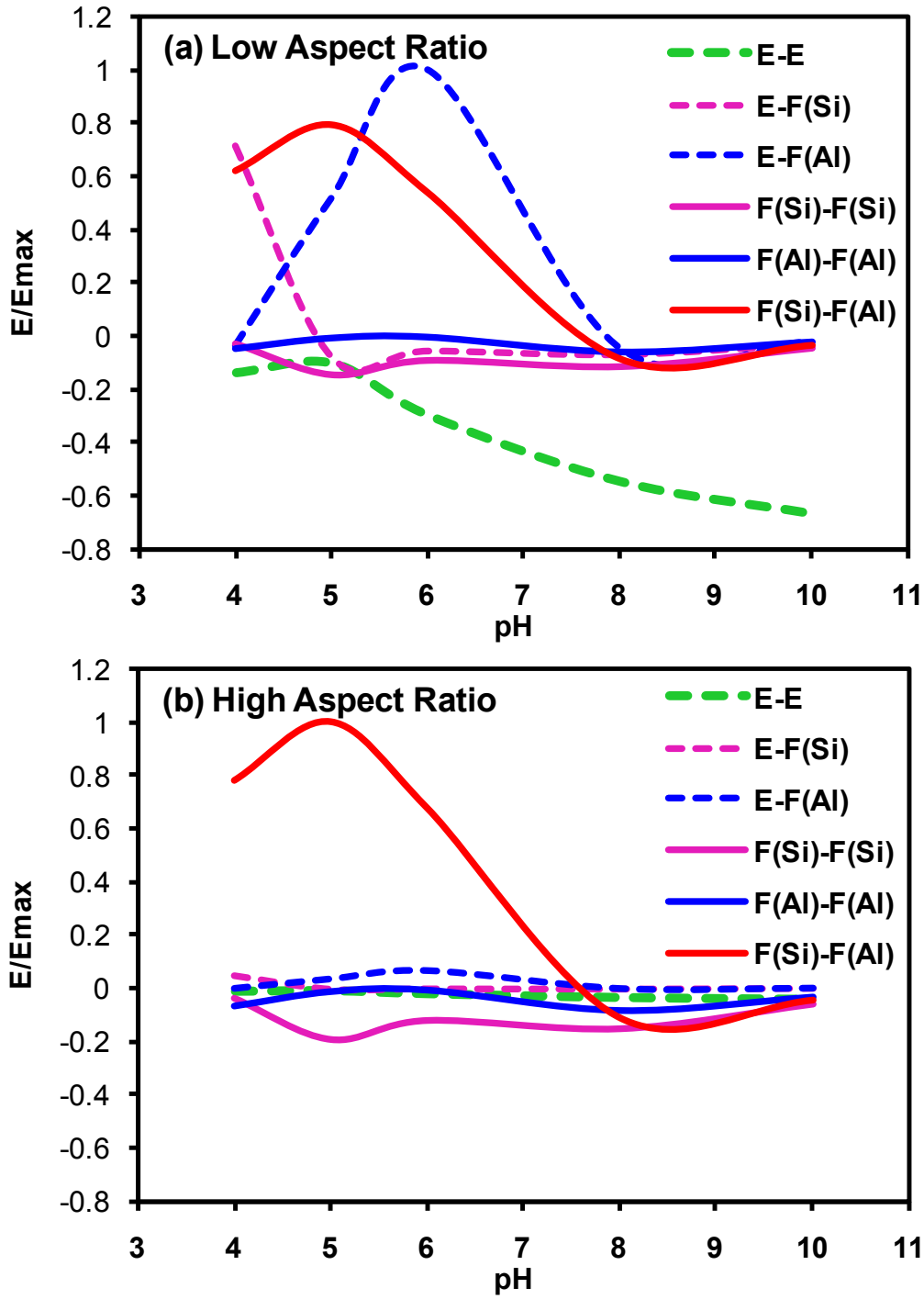

Figure 5.5- Effect of aspect ratio on different face type interaction of kaolinite particles (a) low aspect ratio = 9 and (b) high aspect ratio = 165 in 1 mM KCl solution. The symbols E, F(Si) and F(Al) represent edge, silica face, and alumina face, respectively.

5.3.3 Influence of Electrical Double Layer Thickness

Figure 5.6 shows the effect of electric double layer thickness on the different surface interactions. Particles suspended at high ionic strength will experience a small double layer thickness (3.04 nm) (see Figure 5.6b). Under these circumstances, there is a greater alumina face–alumina face attraction and greater repulsion of silica faces, and edge faces when compared to particles suspended in a solution with a larger double layer thickness (9.6 nm) (see Figure 5.6a). Also at high ionic strength, there is a greater increase in the edge–alumina face interactions which promote edge–face associations as compared to low ionic strength. It is evident that at high ionic strength, i.e., at small values of the reciprocal of the Debye constant (the thickness of the double layer), κ^{-1} = 3.04 nm, the silica face–alumina face interactions will be increased at pH 5 with improved aggregation. At the same time, the increased alumina face–alumina face interactions will expose the silica faces on the kaolinite particles, which may also further promote aggregation with alumina faces, forming a larger aggregate structure. Olphen [16] observed decreasing viscosity and yield stress of dilute and concentrated clay suspensions at lower NaCl concentration. With further addition of NaCl, both the viscosity and the yield stress increase, slowly at first, and rather sharply when the flocculating concentration of NaCl for the clay was approached.

5.3.4 Aggregate Structure

In a suspension of clay particles, three different modes of particle association or aggregate structure may occur: face–face, edge–face, and edge–edge [16]. The DLVO

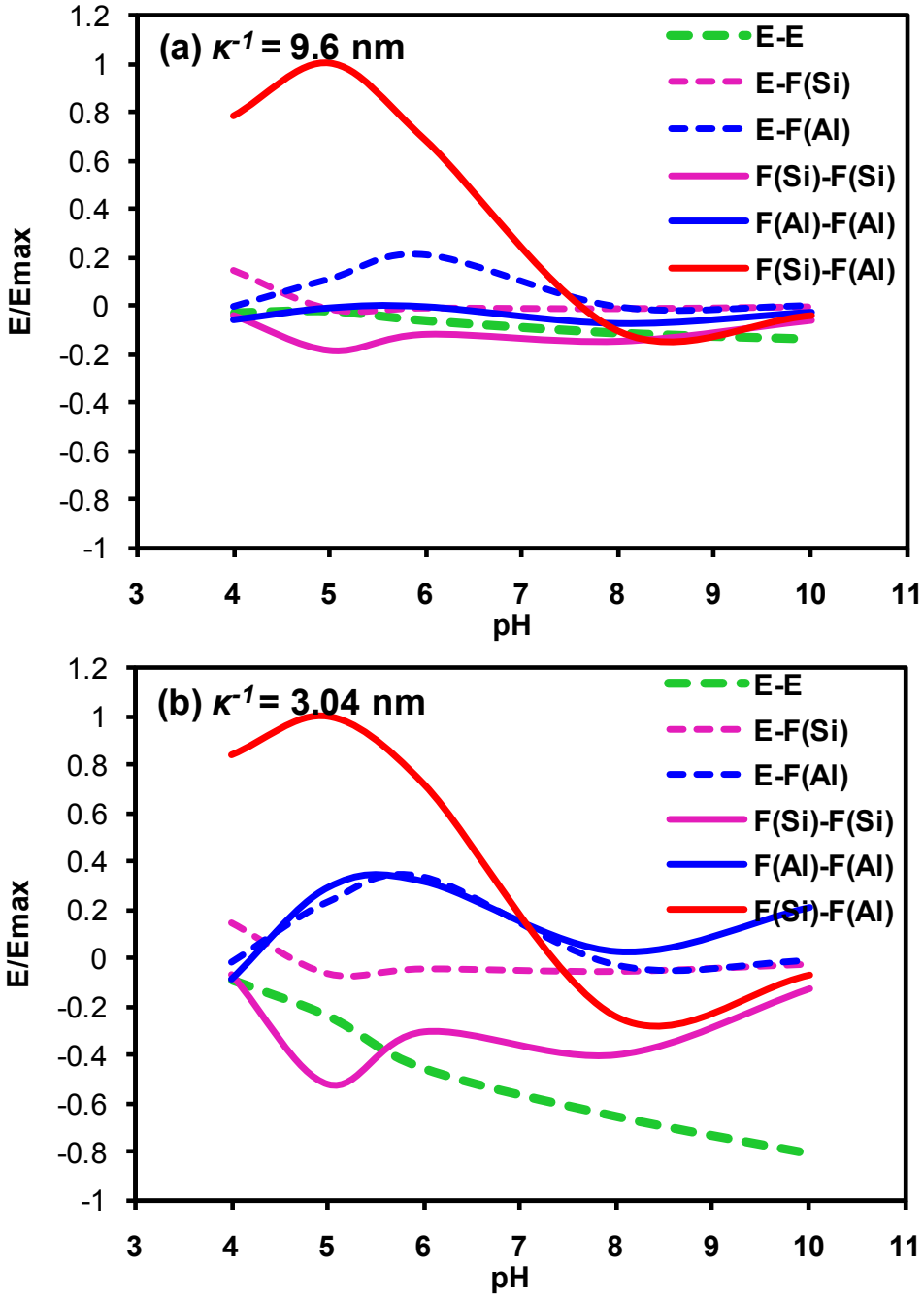

Figure 5.6- Effect of electric double layer thickness (κ-1) on different surface interactions for kaolinite particles with particle diameter 600 nm and thickness 11.2 nm at (a) κ-1 = 9.6 nm (1 mM KCl solution) and (b) κ-1 = 3.04 nm (10 mM KCl solution). The zeta-potentials of the silica face and the alumina face are assumed to be reduced by 30% with increasing ionic strength from 1 mM to 10 mM KCl solution. The edge surface potential data for 10 mM KCl solution were taken from literature[41]. The symbols E, F(Si) and F(Al) represent edge, silica face, and alumina face surfaces, respectively.

interaction energies (electrostatic energy and the van der Waals interaction energy) for the three types of association are governed by six different combinations of the three surfaces interactions – the silica face, the alumina face and the edge surface, as explained previously. Consequently, the three types of association will not necessarily occur simultaneously or to the same extent when a kaolinite suspension is aggregated.

Face–face associations will lead to thicker and possibly larger aggregates, whereas edge–face and edge–edge associations will form three-dimensional voluminous card-house structures [16]. The various modes of particle association are shown in Figure 5.7.

The SEM micrographs of kaolinite aggregates under cryogenic conditions at pH 3, 5, 7, and 9 are shown in Figure 5.8. It can be seen that the kaolinite particles are mostly associated in a face–face manner (silica face–alumina face and/or alumina face–alumina face), and some face-edge organization (edge–silica face) at pH 3 and pH 5 (see Figure 5.8). This is in good agreement with the theoretical predictions that at low pH, the attraction between the silica face and the alumina face dominates and thereby accounts for the face-face association. This face-face association also promotes edge-face aggregation of kaolinite particles with an increase in pH-to-pH 5.

At pH 7, the particles are mostly associated in edge–edge manner and edge–face manner (edge–silica face) (Figure 5.8). At higher pH (pH = 9), the particles are mostly associated in edge-edge manner creating a porous structure. Also, due to repulsion between the silica face and alumina face, face–face association was not observed at pH 9, in agreement with theoretical considerations. The edge–edge interaction at pH 9.0 should also be unfavorable due to similar surface charge density at the edge surfaces, which

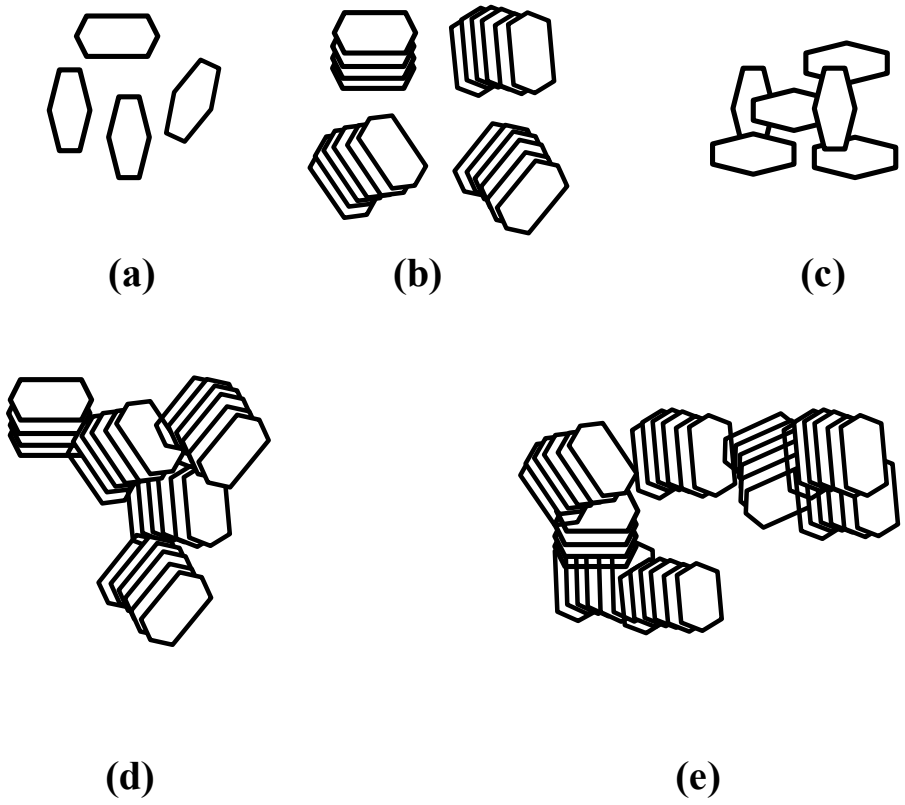

Figure 5.7- The formation of aggregate structures in kaolinite suspensions, as (a) dispersed, (b) face–face, (c) edge–face, (d) edge–edge, and (e) a combination of (b), (c) and (d), depending on the solution chemistry of the suspension.

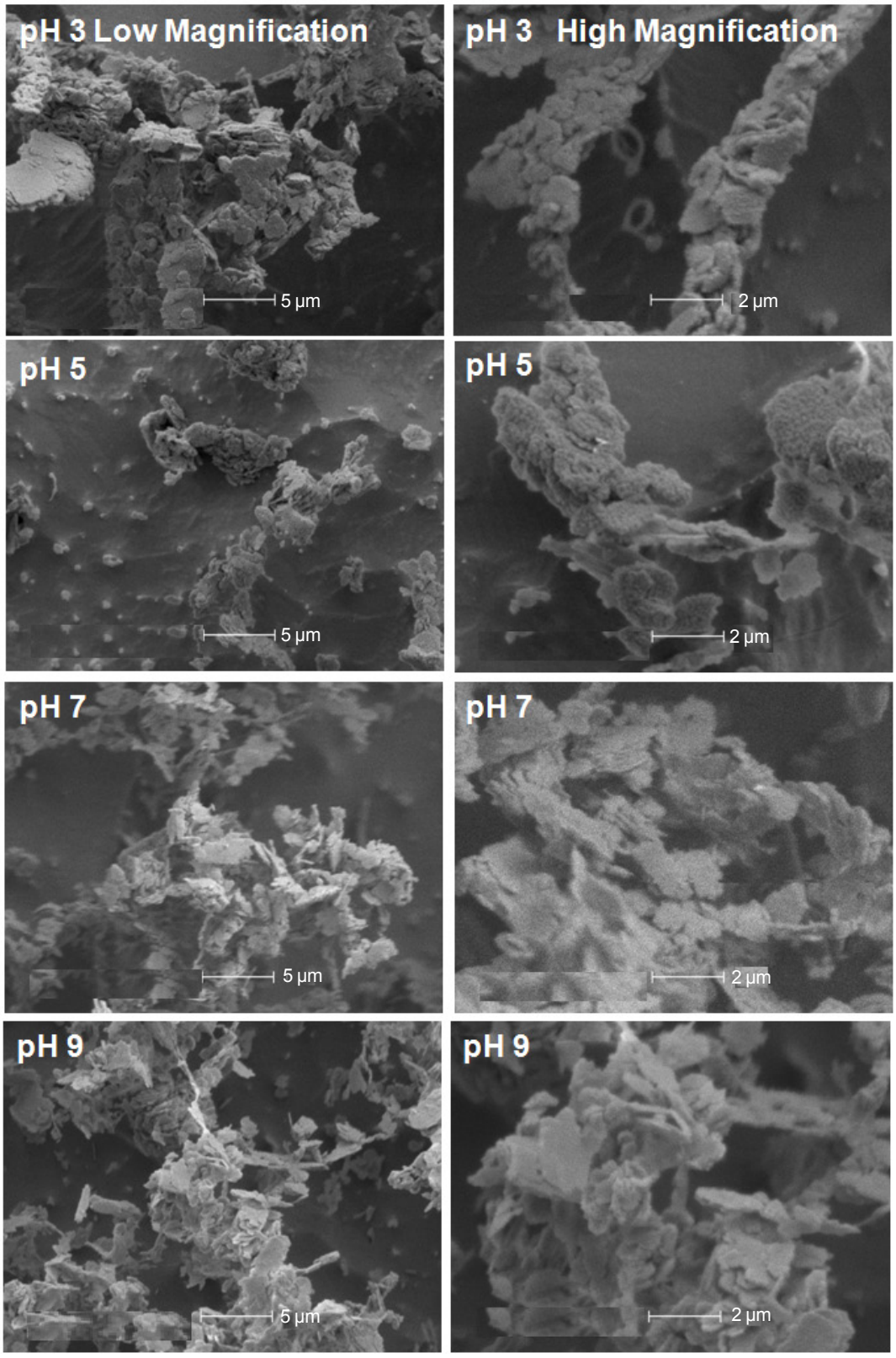

Figure 5.8- Cryo-SEM micrographs of kaolinite aggregates at pH 3, 5, 7 and 9 at low (left) and high (right) magnification.

causes repulsion. The edge–edge associations at high pH 9 were contrary to DLVO expectation, since all the surfaces of kaolinite particles are negatively charged, and the suspension is stable. In agreement with our observation, Zbik and Horn [175] also observed similar structures involving edge–edge association for kaolinite particles, and they proposed that hydrophobic interaction between edge surfaces could contribute to such structures. Such a proposition needs further consideration. Alternatively, the edge–edge association observed at pH 9.0 may be due to the experimental conditions associated with freezing the sample under cryogenic conditions.

The cryogenic-SEM images showed the kaolinite aggregate structure for a 4% kaolinite suspension. This concentration may well be above the gelation point [171], but the general trends of the aggregate structure showing dominant face-face association was also observed in dilute (0.01%) and semidilute (0.1%) kaolinite suspensions (SEM graphs not shown). Our results are also supported by Zbik and Frost [171] who observed similar face–face and edge–face contacts in kaolinite from Georgia. Other modes of particle associations such as stair step edge–edge contacts were also revealed in Birdwood kaolinite aggregates [171].

5.3.5 Aggregate Size

The aggregate structure of kaolinite suspensions at different pH values as revealed by cryo-SEM are also supported by further experiments conducted using photon correlation spectroscopy (PCS) to estimate the particle size of such aggregates. In our analysis, we estimated the equivalent sphere diameter of aggregate-structures for kaolinite suspensions. These aggregate structures for kaolinite suspensions are three-

dimensional networks of particles forming an arbitrary shape or so-called “card-house” structure [16]. The precise information for the size of aggregate structures in kaolinite suspensions could not be revealed with present instrumentation, and only qualitative trends are realized. Figure 5.9 shows the average particle size of kaolinite aggregates in suspension as a function of pH. As shown, the average aggregate size of kaolinite is about 16.3±0.3 nm at pH 7 and 9. The average aggregate size of kaolinite remains unchanged when measured as a function of time at pH 9, which represents a more dispersed state for the kaolinite particles. The aggregate size grows to 38.9±0.3 nm at pH 7 in 40 minutes, which could be indicative of a loose aggregate structure formed mainly by edge–edge associations. The initial aggregate size for kaolinite suspensions at pH 3.5 and 5 were 266.8±12.0 nm and 127.1±7.9 nm, respectively. The aggregates of kaolinite grow over an order of magnitude in size in just a few minutes at pH 3 and 5, and then remain constant. These results suggest that kaolinite particles are associated with all three modes of interactions – face–face, edge–face and edge-edge – forming a three-dimensional network. In our analysis, we estimated the equivalent sphere diameter of aggregate-structures for kaolinite suspensions. These aggregate structures for kaolinite suspensions are three-dimensional networks of particles forming an arbitrary shape or so called “card-house” structure [16]. The precise information for the size of aggregate structures in kaolinite suspensions could not be revealed with present instrumentation, and only qualitative trends are realized. Of course, as stated previously, the aggregate structure as revealed by cryo-SEM and PCS will influence the mechanical properties of kaolinite suspensions, and thereby affect the rheological properties of such suspensions.

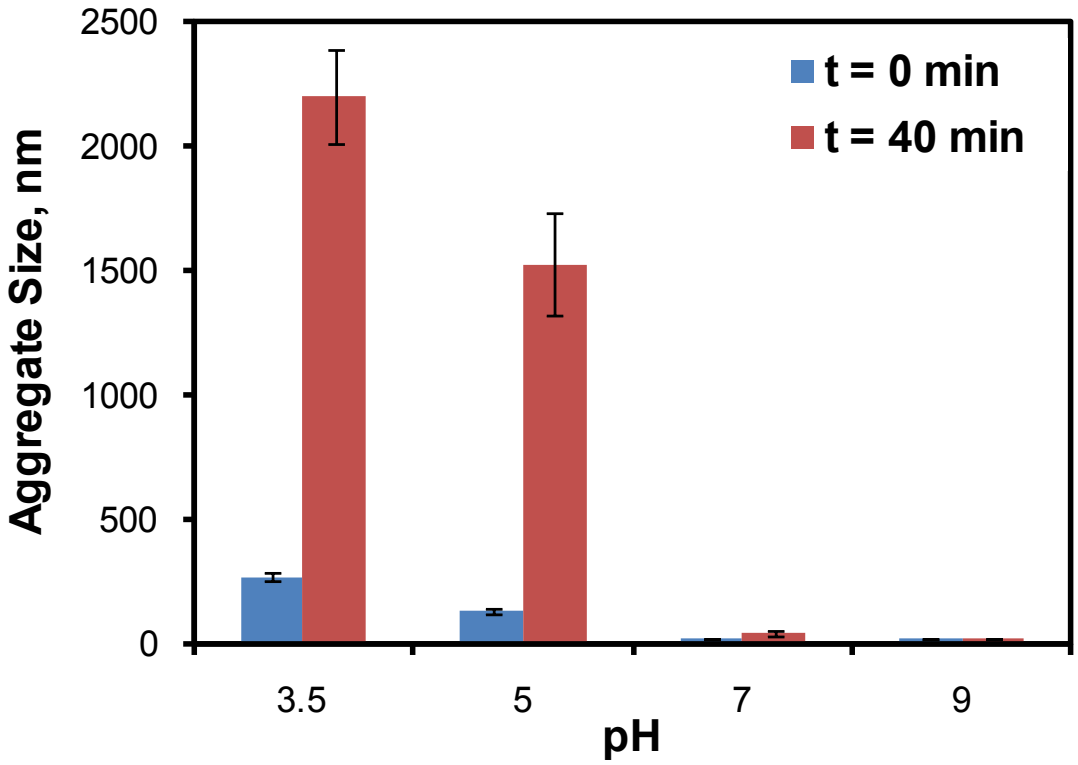

Figure 5.9- Average aggregate size for a suspension of kaolinite particles as a function of pH.

5.4 Summary

The mechanical properties of kaolinite suspensions, particularly the shear yield stress, is explained based on the aggregate structure of the kaolinite particles. A new analysis based on the surface charge densities of the silica face, alumina face and edge surfaces demonstrate the role of pair-wise interactions in controlling the rheology of kaolinite particulate suspensions. The maximum shear yield stress of kaolinite suspensions is indicative of the significant role played by particle organization in the formation of aggregates as governed by edge–edge, edge–silica face, edge–alumina face, silica face–alumina face, silica face–silica face, and alumina face–alumina face interaction energies.

The results indicate that the face–face (silica face–alumina face) is the dominant particle interaction at low pH values, which promotes edge–face (edge–silica face and edge–alumina face) and face–face (silica face–alumina face) interaction at intermediate pH values, justifying the maximum shear yield stress at pH 5-5.5. This conclusion is also confirmed by cryo-SEM analysis of kaolinite aggregate structure and photon correlation spectroscopy. At a higher pH (pH = 7), the kaolinite aggregates show edge–edge and edge–face interactions, whereas a more porous structure of aggregates was observed at high pH (pH = 9).

The influences of particle aspect ratio and electrical double layer thickness were also examined to determine their effect on interaction energies. The findings show that the edge surface–silica face interactions become favorable at a low aspect ratio, whereas the silica face–alumina face and alumina face–alumina face interactions are increased at high ionic strength conditions. These different interactions and their relative significance,

provide the basis for a more detailed explanation of the rheological behavior of kaolinite suspensions as well as an improved foundation for the modification of kaolinite interactions and control of rheological properties.

CHAPTER 6

CRYSTAL LATTICE IMAGING OF THE SILICA AND ALUMINA FACES OF KAOLINITE USING ATOMIC FORCE MICROSCOPY

The crystal lattice images of the two faces of kaolinite (the silica face and the alumina face) have been obtained using contact-mode atomic force microscopy (AFM) under ambient conditions. Lattice resolution images reveal the hexagonal surface lattice of these two faces of kaolinite. Analysis of the silica face of kaolinite showed that the hexagonal surface lattice ring of oxygen atoms had a periodicity of 0.50 ± 0.04 nm between neighboring oxygen atoms, which is in good agreement with the surface lattice structure of the mica basal plane. The center of the hexagonal ring of oxygen atoms is vacant.

Analysis of the alumina face of kaolinite showed that the hexagonal surface lattice ring of hydroxyls surround a hydroxyl in the center of the ring. The atomic spacing between neighboring hydroxyls was determined as 0.36 ± 0.04 nm. Ordering of the kaolinite particles for examination of the silica and alumina surfaces was accomplished using different substrates, a procedure previously established. Crystal lattice imaging

supports previous results and independently confirms that the two faces of kaolinite have been properly identified.

6.1 Introduction

Kaolinite [$Al_2O_3.2SiO_2.2H_2O$] is an industrial mineral and its surface properties are of particular importance in widespread applications, e.g., in ceramics, in the manufacture of paper (as a coating, pigment and filler), in inks and paints (as an extender), and as an additive in the production of rubber and polymers [53, 63, 116]. In other situations, kaolinite is a nuisance when present as a gangue mineral in flotation separations and during the thickening of plant tailings.

Kaolinite naturally exists as pseudo-hexagonal, platy-shaped, thin particles generally having a size of less than one micron extending down to 100 nm. The behavior of these nanosized kaolinite particles in suspensions, pastes, and composite materials is controlled by its surface chemistry features. Analysis of the surface chemistry features, such as electrokinetic phenomena, is complicated by the anisotropic, platy structure of the particles, which manifests itself in edge surfaces and face surfaces. Additionally, the bilayer mineral structure suggests that there should be two types of surface faces defined by the 001 and the 00$\underline{1}$ basal planes. In this way, one face should be described by a silica tetrahedral surface and the other face should be described by an aluminum hydroxide (alumina) octahedral surface, as shown in Figure 1.1.

Limited research has been reported on the experimental characterization of these face surfaces [15]. A few studies have reported the average FTIR spectra of both faces of kaolinite [53-55]. Recent development of advanced analytical techniques (XPS - X-ray

photoelectron spectroscopy, LEISS - Low energy ion scattering spectroscopy, and ToF-SIMS - Time of flight-secondary ions mass spectroscopy) seem promising to facilitate investigation of the two faces of kaolinite provided that the particles can be oriented, and that the instrumentation is sufficiently surface sensitive to collect signals from just the very first layer. For example, a recent study attempted to use ToF-SIMS to study the talc surface [56]. However, these results were averaged over a few layers of talc. Recently, many researchers have used scanning electron microscopy (SEM) [58, 59], transmission electron microscopy (TEM) [60] and atomic force microscopy (AFM) [59, 61, 62] as imaging tools to characterize particle shape and morphology.

It is now well established with some success that AFM can also be used to investigate the crystal lattice structure of mineral surfaces. Atomic resolution has been successfully obtained on graphite [176, 177], molybdenum sulfide [176], boron nitride [178], germanium [179], sapphire [180], albite [181], calcite [182] and sodium chloride [183]. The AFM has also been used to investigate the crystal lattice structure of the tetrahedral layer of clay minerals in 2:1 layer structures, such as muscovite [184], illite [185] and montmorillonite [185]. Atomic-scale resolution has also been obtained for the basal oxygen atoms of a mixed-layered illite/smectite [186], zeolite clinoptilolite [187] and hematite [188]. The details of obtaining atomic and subnanometer resolution imaging in ambient conditions by AFM is given in the literature [189].

Wicks *et al.* [190] were probably the first to simultaneously report the surface images of both the tetrahedral and octahedral sheets of lizardite (1:1 layer structure) using AFM, and they identified the surface hydroxyl groups and magnesium atoms in the octahedral sheet. In this way, they identified the two sides of the lizardite clay mineral.

The surface images of chlorite (2:1:1-type structure) were also investigated by AFM, and both the tetrahedral sheet and the brucite-like interlayer sheet was observed [191].

Recently, Kumai *et al.* [192] examined the kaolinite surface using AFM. They used the "pressed" powder sample preparation technique, and obtained the surface images of both the silica tetrahedral surface and alumina octahedral surface of kaolinite particles. However, this technique is compromised as the particles are randomly oriented, and poses difficulty in identifying the appropriate face surface (silica face or alumina face) of kaolinite.

A recent study by Gupta and Miller [72] demonstrates an appropriate technique to orient the kaolinite particles, which selectively exposes the silica face and alumina face of kaolinite by depositing the particles on glass and alumina substrates, respectively. These researchers have indirectly confirmed the silica face and alumina face of kaolinite by surface force measurements on the two faces of kaolinite. The objective of this paper is to distinguish the silica face and alumina face of kaolinite by direct surface imaging at the atomic level using AFM, thus providing independent confirmation of the procedure developed previously [72].

6.2 Materials and Methods

6.2.1 Sample Preparation

A clean English kaolin (Imerys Inc., UK) was obtained from the St. Austell area in Cornwall, UK. The sample was cleaned with water and elutriation was used to achieve classification at a size of less than 2 μm. No other chemical treatment was done. Further details about the kaolinite extraction and preparation are given in the literature [124]. The

kaolinite suspension (1000 ppm) was prepared in high purity Milli-Q water (Millipore Inc.) with a resistivity of 18.2 MΩ-cm. The pH was adjusted to 5.5 using 0.1 M HCl or 0.1 M KOH solutions. All chemicals used were of ACS grade. The kaolinite was the dominant mineral phase as characterized using X-ray diffraction and energy dispersive spectroscopy. Further details of kaolinite characterization are reported in the literature [72].

6.2.2 Substrate Preparation

Two substrates – a mica disc (ProSciTech, Queensland, Australia) and a fused alumina substrate (Red Optronics, Mountain View, CA), were used to order the kaolinite particles [72]. The kaolinite particle suspension (1000 ppm) was sonicated for 2 minutes, and about 10 μl of the suspension was air-dried overnight on a freshly cleaved mica substrate under a petri-dish cover in a laminar-flow fume hood. In this way, the kaolinite particles attach to the mica substrate with the alumina face down exposing the silica face of kaolinite, as shown from previous surface force measurements [72], i.e., the positively charged alumina face of kaolinite is attached to the negatively charged mica substrate.

The fused alumina substrate was cleaned using piranha solution (a mixture of sulfuric acid and hydrogen peroxide in a ratio of 3:1) at 120^0C for 15 minutes, followed by rinsing with copious amounts of Milli-Q water, and finally blown dry with ultra high purity N_2 gas. A 10 μl kaolinite suspension was applied to the alumina substrate and dried in the same manner as the mica. It was found that the alumina face of kaolinite was exposed on the fused alumina substrate based on previous surface force measurements

[72], i.e., the negatively charged silica face of kaolinite is attached to the positively charged fused-alumina substrate.

The samples were prepared the night before AFM analysis and stored in a desiccator until their use. Just prior to the AFM experiments, the substrates were sonicated for a minute in Milli-Q water to remove loosely adhered kaolinite particles, washed with Milli-Q water, and gently blown with N_2 gas before AFM investigation. All substrates were attached to a standard sample puck using double-sided tape.

6.2.3 Atomic Force Microscopy

A Nanoscope AFM with Nanoscope IV controller (Veeco Instruments Inc., Santa Barbara, CA) was used with an E-type scanner. Triangular beam silicon nitride (Si_3N_4) cantilevers (Veeco Instruments Inc., Santa Barbara, CA), having pyramid-shaped tips with spring constants of about 0.58 N/m, were used. The cantilevers were cleaned using acetone, ethanol, water in that order, and gently dried with ultra high purity N_2 gas. The cantilevers were subsequently cleaned in a UV chamber for 30 minutes prior to use. The substrates were loaded on AFM equipped with a fluid cell. The contact mode imaging was done in Milli-Q water. The AFM instrument was kept in an acoustic and vibration isolation chamber. The imaging was commenced 30 minutes after sample loading to allow the thermal vibration of the cantilever to equilibrate in the fluid cell. First, an image of the particles was obtained at a scan rate of 1 Hz and scan area of 1 μm. Subsequently, the atomic resolution imaging was completed using the zoom-in and offset feature of the Nanoscope vs. 5.31R1 software (Veeco Instruments Inc., Santa Barbara, CA) to scan an area of 12 nm on the particle surface. The atomic imaging was obtained at a scan rate of

30 Hz at scan angle of 80^0–90^0 with very low integral and proportional gain (0.06). The online filters (low pass and high pass) were turned off during the online crystal lattice imaging.

During offline image processing, flattening and low pass filtering were applied to obtain clear images using Nanoscope vs. 5.31R1 software. The images were further Fourier-filtered (2D FFT) to obtain the crystal lattice images using SPIP software (Image Metrology A/S, Denmark).

6.3 Results and Discussion

In order to obtain the crystal lattice imaging of the silica face and alumina face of kaolinite, the scanner was first calibrated using a mica substrate. Figure 6.1 presents the crystal lattice imaging of mica, which shows the height image, fast-Fourier transform (FFT) spectra and the FFT transformed height image. In order to make sure that the image is real, the imaging was done at other locations on the mica substrate and also with varying scan size and scan angle. The repeated pattern of dark and light spots was reproducible and the dark spots observed were scaled appropriately with the scan size and angle. The images showed some drift in both x and y direction during imaging. The dark spots in Figure 6.1C and 2D correspond to a hole surrounded by the hexagonal lattice of oxygen atoms. The light spots are attributed to the three-surface oxygen atoms forming a SiO_4 tetrahedron or pairs of SiO_4 tetrahedra forming a hexagonal ring-like network. Similar images were reported for the 1:1 type clay mineral, lizardite [190] and other 2:1 type clay minerals [184, 185, 193] from AFM observations on a single crystal. The fast-Fourier transform showed the intensity peaks of oxygen atoms arranged in a hexagonal

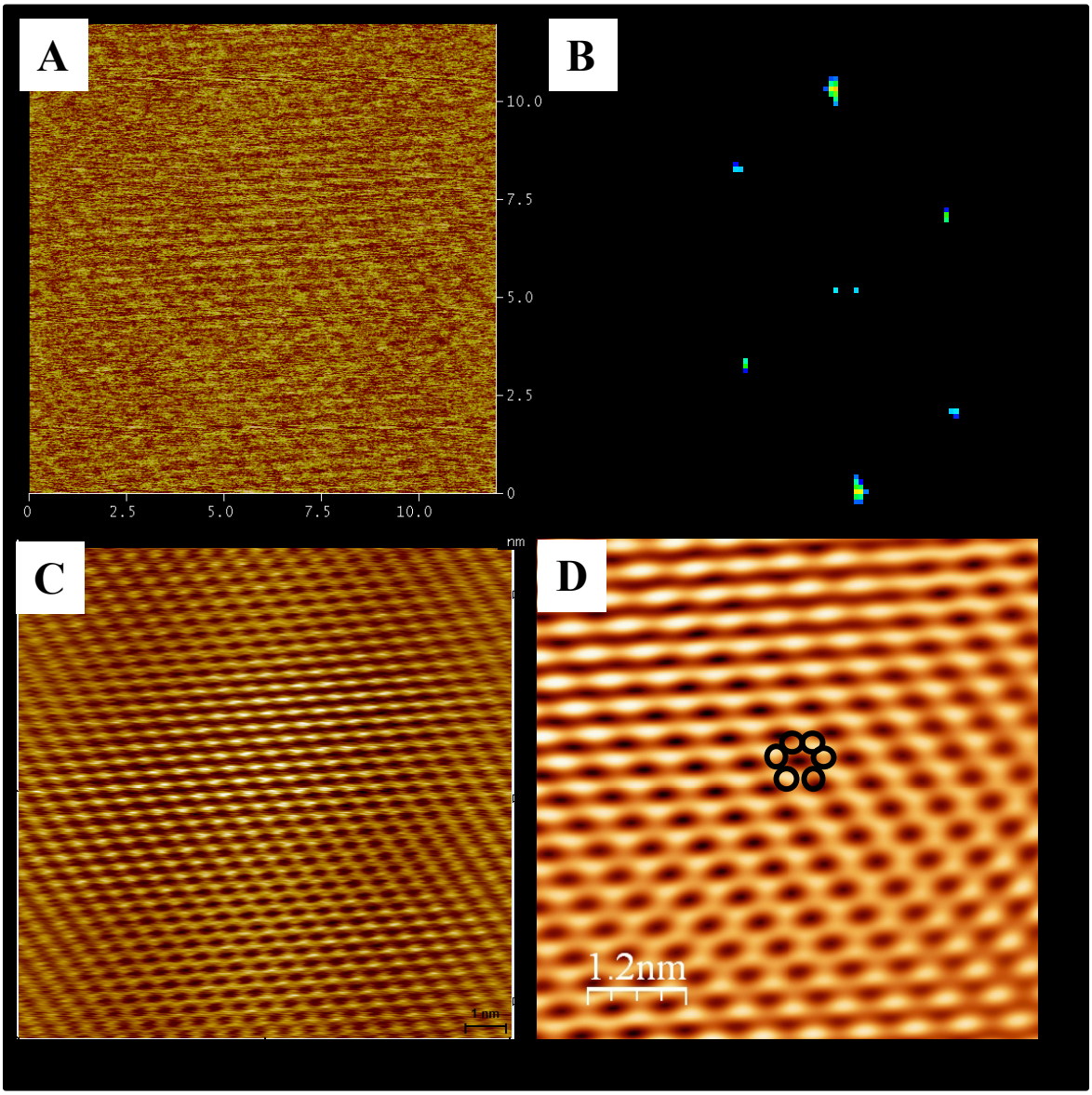

Figure 6.1- Crystal lattice imaging of mica substrate showing (A) Flattened height image, (B) FFT spectra, (C) FFT transformed flattened height image, and (D) Zoomed-in image of (C) of scan area of 36 nm2. The six light spots in (D) shows the hexagonal ring of oxygen atoms around the dark spots representing a hole.

ring network (see Figure 6.1B). The crystal lattice spacing between neighboring oxygen atoms was calculated as 0.51 ± 0.08 nm, from the average of 10 neighboring atoms. This is in very good agreement with the literature value of 0.519 nm [194].

Figure 6.2 shows an image of a kaolinite particle on a mica substrate. The image shows the platy nature and the pseudo-hexagonal shape of the kaolinite particle. The scanning was sequentially zoomed on the particle. Figure 6.3 shows the crystal lattice imaging of the silica face of a kaolinite particle on the mica substrate. The flattening and low pass filtering was applied to the height image in an offline mode (see Figure 6.3B). The FFT spectra showed the similar intensity of peaks of oxygen atoms arranged in a hexagonal ring network as observed for the mica substrate. As expected, the silica face of kaolinite showed the similar hexagonal ring-like network of oxygen atoms as observed on the mica substrate (compare Figure 6.1D and Figure 6.3D). Note that the scan scale for the image of the silica face of kaolinite was twice that used for the mica substrate (12 nm vs. 6 nm), which shows the reproducibility of the crystal lattice images obtained on different substrates. The crystal lattice spacing between neighboring oxygen atoms was calculated as 0.50 ± 0.04 nm, from the average of 10 neighboring atoms. This lattice spacing is in good agreement with 0.53 nm as reported in the literature [192].

The crystal lattice imaging of the alumina face of kaolinite on a fused alumina substrate is shown in Figure 6.4. The FFT spectra shows the intensity peaks of the hydroxyl atoms forming a hexagonal ring network similar to that obtained on the silica face of kaolinite (see Figure 6.4c). Notice that the hexagonal ring of hydroxyls shows the inner hydroxyl in the center of the ring instead of a hole as observed for the silica face of kaolinite and mica substrates (compare Figure 6.1D, Figure 6.3D, and Figure 6.4D). The

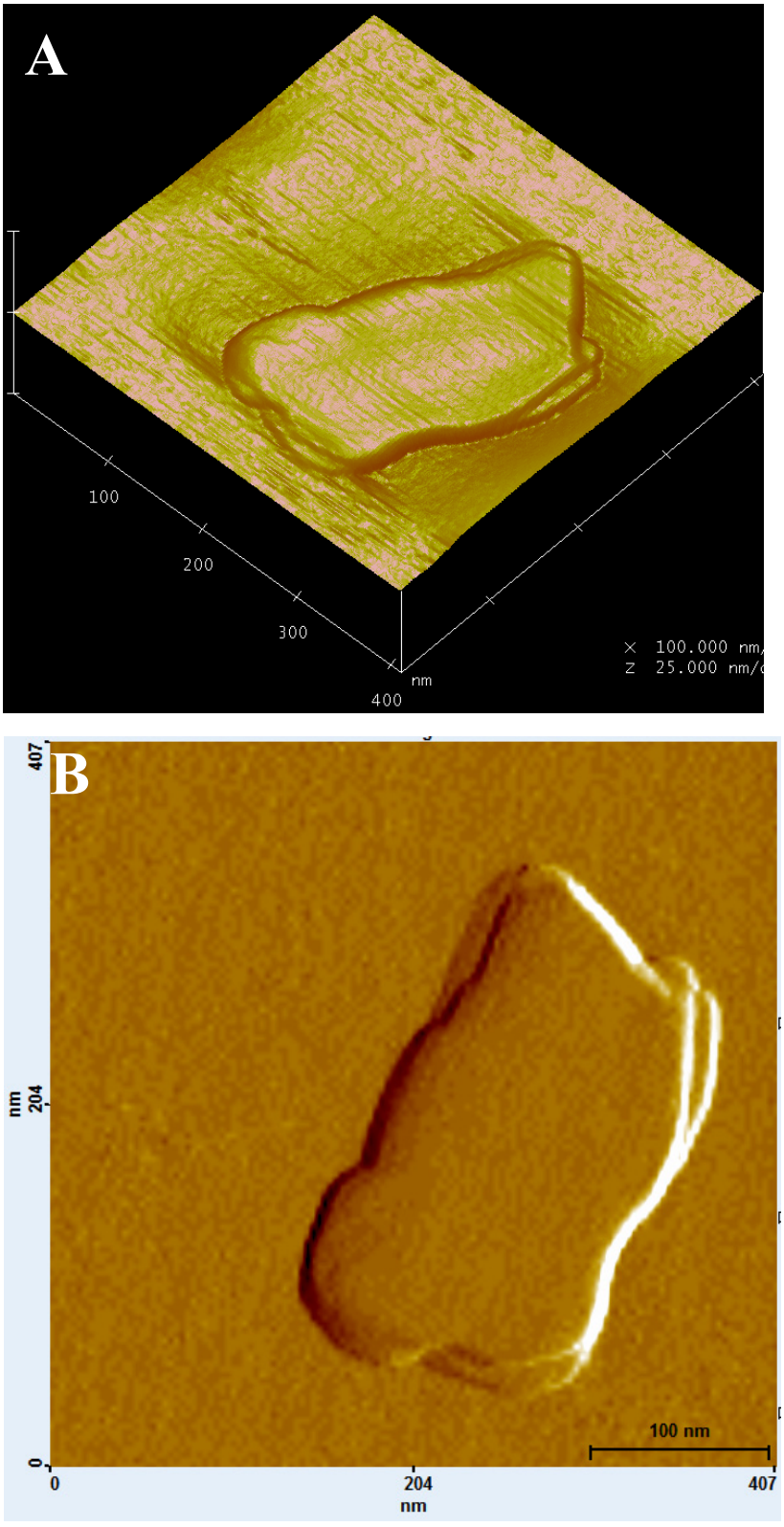

4.1

Figure 6.2- (A) Topography, and (B) Deflection images of kaolinite particle on the mica substrate.

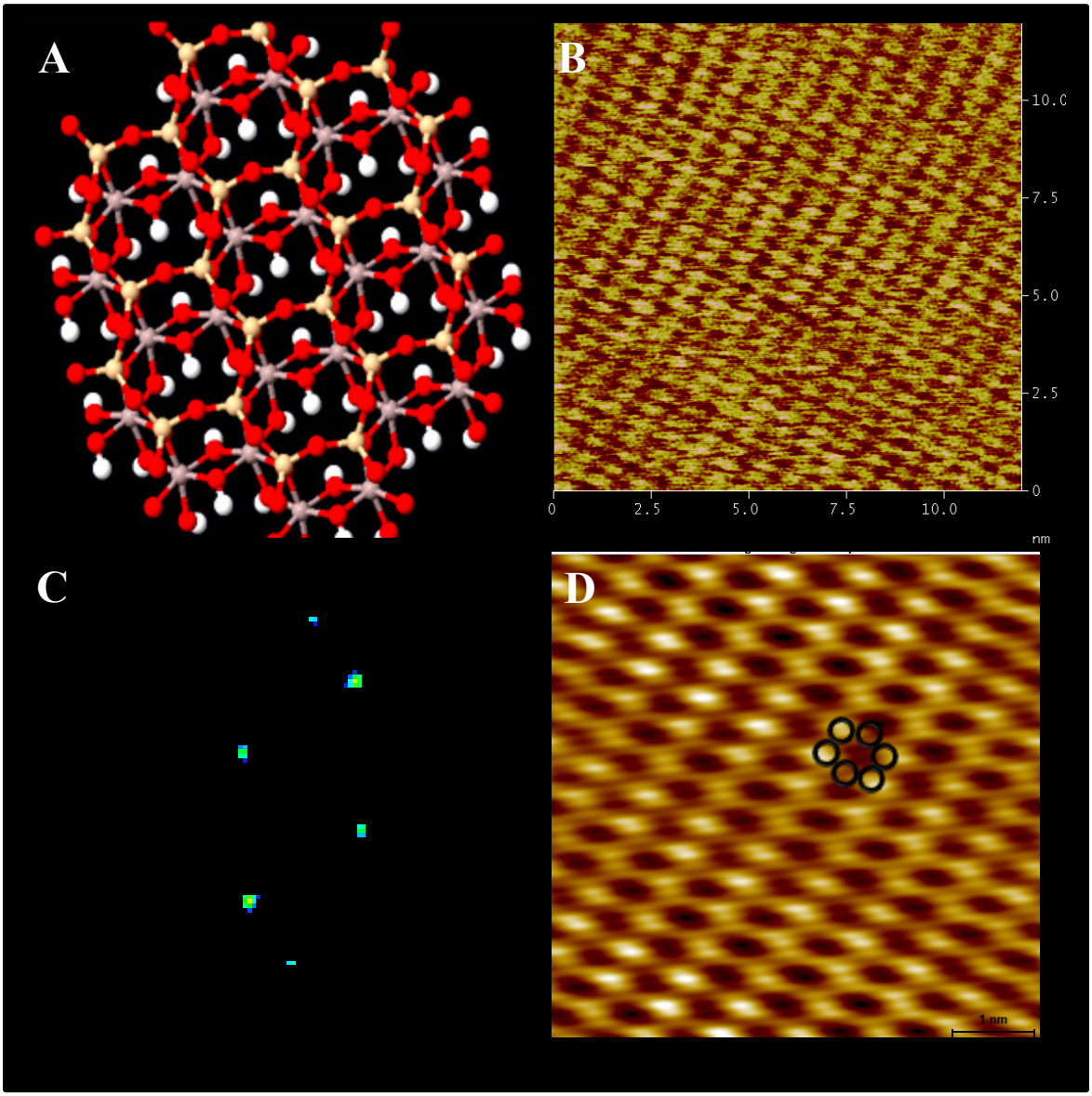

Figure 6.3- Crystal lattice imaging of the silica face of kaolinite showing (A) Theoretical atomic lattice structure (B) Flattened-low pass filtered height image, (C) FFT spectra, and (D) FFT transformed flattened-low pass filtered height image of scan size 36 nm2. The six black circles in (D) shows the hexagonal ring of oxygen atoms around the dark spots representing a hole.

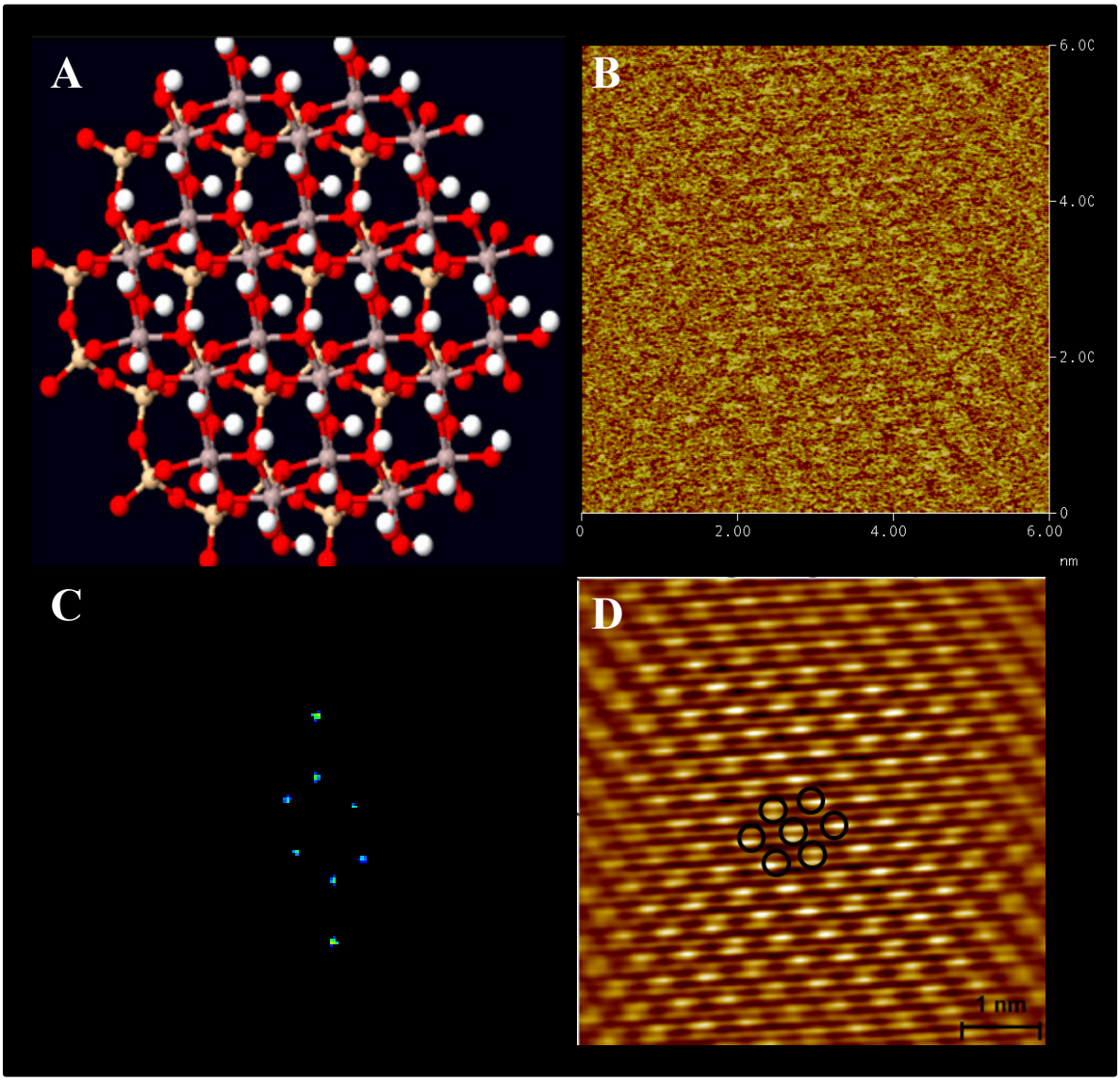

Figure 6.4- Crystal lattice imaging of alumina face of kaolinite showing (A) Theoretical atomic lattice structure (B) Flattened-low pass filtered height image, (C) FFT spectra, and (D) FFT transformed flattened-low pass filtered height image of (B). The seven black circles in (D) shows the hexagonal ring of hydroxyl atoms with a central inner hydroxyl atom.

image shown in Figure 6.4D is similar to the octahedral sheet of lizardite [190], the internal octahedral sheets of micas and chlorite [194], and the brucite-like layers of hydrotalcite [195]. The octahedral sheet of kaolinite consists of a plane of hydroxyls on the surface. The average hydroxyl-hydroxyl distance of the octahedral sheet is 0.36 ± 0.04 nm which is in reasonable agreement with the literature value of 0.29 nm [196]. For a kaolinite pellet, Kumai *et al.* [192] observed the distance between the hydroxyl atoms as 0.33 nm.

Recently, Gupta and Miller [72] indirectly identified the two kaolinite faces – silica face and alumina face – through surface force measurements between each of these two faces and a silicon nitride cantilever. These authors demonstrated that the silica face of kaolinite is negatively charged at pH > 4, whereas the alumina face is positively charged at pH < 6 and negatively charged at pH > 8. These results are in excellent agreement with the lattice images of the silica face and the alumina face of kaolinite showing the distinct feature of these faces (the hexagonal ring of oxygen atoms on the silica face, and the hexagonal ring of hydroxyls surrounding a central hydroxyl on the alumina face).

More importantly, the experimental technique developed by Gupta and Miller [72] to order kaolinite particles with the desired face exposed is validated. This procedure using two different appropriate substrates is unique, and could be applied for AFM interrogation of any bilayer system with different characteristics to better understand their surface properties and crystal structure.

6.4 Summary

Crystal lattice images were obtained on the silica tetrahedral and alumina octahedral faces of kaolinite using atomic force microscopy. The images showed the repeated tetrahedral oxygen atoms on the silica face forming a closed hexagonal ring-like network with a hole in the center. On the other hand, as expected, the alumina face of kaolinite showed the hexagonal ring of hydroxyls surrounding a central hydroxyl. These results validate the procedure to order kaolinite particles with the desired face exposed [72]. It is clear that atomic force microscopy can be used effectively in the investigation of mineral surfaces, even for particles of nanometer size.

CHAPTER 7

HIGH RESOLUTION TRANSMISSION ELECTRON MICROSCOPY OF KAOLINITE

Results from a high resolution transmission electron microscopy investigation of kaolinite has indicated that kaolinite (1:1 type of clay) is indeed composed of bilayers of a silica tetrahedral sheet bonded to an alumina octahedral sheet, with a c-spacing between the bilayers of 7.2 Å. Occasionally, defects in the form of bended bilayers was observed in selected kaolinite particles. HRTEM has also indicated that a trilayer structure (2:1 type clay) with increased c-spacing of 10 Å was occasionally present in the kaolinite structure lying between the kaolinite bilayers. In addition, occasionally, a single trilayer particle was found in the kaolinite population but this was a rare occasion. Of course, the presence of such defects in the kaolinite particles and the presence of trace amounts of 2:1 layer clay minerals particles will influence the surface chemistry, including the surface charge properties of kaolinite.

7.1 Introduction

The understanding of the structure of the kaolinite is important as it influences its surface chemistry, particularly the electrokinetics properties. The existence of defects in

the bilayer of a kaolinite particle and the presence of other 2:1 clay mineral particles in the kaolinite population will affect its surface charge properties. Frequently, X-ray diffraction (XRD) is used to characterize the defects and other clay minerals in a kaolinite sample. The existence of layer defects and/or a small amount of other clay mineral particles does not always correlate with the XRD results. In some instances, high crystallinity, as estimated by XRD, corresponds to fewer defects and dislocations in kaolinite [197]. XRD powder patterns are not sensitive enough to identify the small amount of mixed clay minerals that may be present in the kaolinite samples.

High resolution transmission electron microscopy (HRTEM) has been a powerful tool in studying the layering structure of kaolinite and other clay minerals [60, 197-202]. HRTEM has contributed to the investigation of stacking structures in phyllosilicates as established in the literature [203]. HRTEM imaging with the electron beam parallel to layers enables direct determination of the stacking sequence for individual layers, which is necessary to analyze nonperiodic structures, i.e., stacking disorders or faults, as well as other mixed-layer silicates. Yada [204, 205] first studied the structure of chrysotile and antigorite using HRTEM. They reported that the chrysotile has a fibrous structure with a c-spacing of 7.3 Å, whereas antigorite consist of a wavy structure where the tetrahedral sheet exchanges polarity with the octahedral sheet every few tetrahedra. Amouric and Olives [199] used HRTEM to investigate the transformation of smectite into kaolinite and kaolinite-smectite interstratifications. Mixed-layer silicates such as illite and smectite have also been studied with HRTEM [206].

Despite the good success with HRTEM, few studies have analyzed the stacking and crystal organization of kaolin minerals [197, 200]. Ma and Eggleton [197] examine

the kaolinite surface using HRTEM and indicated that three types of face surfaces may exist in natural kaolinite crystals. Type 1 kaolinite structure is the ideal structure and has the expected 7 Å surface layer as the terminal layer exposed (i.e., TOTOTOTO…where T stands for silica tetrahedral layer and O stands for alumina octahedral layer). Type 2 kaolinite structure has one 10 Å pyrophyllite-like layer as the surface layer on one side of the kaolinite particle (TOTOTOTO….TOTO(TOT)). Type 3 kaolinite structure has one or several 10 Å collapsed smectite-like layers at one or both sides of a stack ((TOT)TOTOTOTO….TOTO(TOT)). Kogure and Inoue [200] investigated the stacking defects in kaolinite and dickite. The authors observed a high density of stacking defects in kaolinite which are formed by a mixture of two kinds of lateral interlayer shifts between adjacent layers. With this information, Kogure and Inoue [200] also explained the kaolinite-to-dickite transformation mechanism. Different stacking sequence and/or defects may exist in kaolinite of particular origin.

Therefore, the objective of the research reported in this chapter is to investigate whether the 1:1 bilayer structure of kaolinite is consistent with the ideal crystal structure (Type 1) or is the Cornwall kaolinite used in this dissertation research described by termination with a 2:1 structure which defines the face surfaces. The surface chemistry, particularly the electrokinetic considerations of kaolinite particles and their face surfaces, would be affected by these terminations of 1:1 (kaolinite) or 2:1 (smectite) type layers.

7.2 Sample Preparation

Kaolinite powder was ground for 10 minutes using an agate pestle mortar and then embedded into a molded resin block. Thin sections with a thickness from 50 nm to

100nm were cut from an intact resin block using a Leica UltraCut microtome (Leica Microsystems) and collected onto formvar-coated copper mesh grids. After being transferred onto the grids, the thin sections were also lightly coated with carbon to minimize the charging effect during the TEM imaging.

7.3 Electron Microscopy

Tecnai F20 (FEI Co., Oregon, USA), a twin-lens system, operated at 200kV was used for the investigation of the thin sections of kaolinite particles. The images (4096×4096) were digitally acquired by an UltraScan^{TM} 4000 (USC4000, Model 895; Gatan Inc.) using a charge-coupled device (CCD) imaging. The images were processed and analyzed using DigitalMicrograph (version 3.9.1, powered by the Gatan Software Team).

7.4 Results and Discussion

The layered structure of kaolinite is shown in Figure 7.1 at low magnification showing the stacking of kaolinite particles viewed along their edge surface. Single particles of kaolinite were found to be 100-150 nm thick. A bilayer in a kaolinite particle is about 0.72 nm thick. These results indicate that a kaolinite particle structure consists of 138-208 bilayers.

The lattice fringe pattern of the kaolinite particles with the electron beam parallel to 001 basal plane was obtained, as shown in Figure 7.2. The dark and light fringe pattern shows a c-spacing of 7.2 Å. This c-spacing is very consistent as reported in the literature,

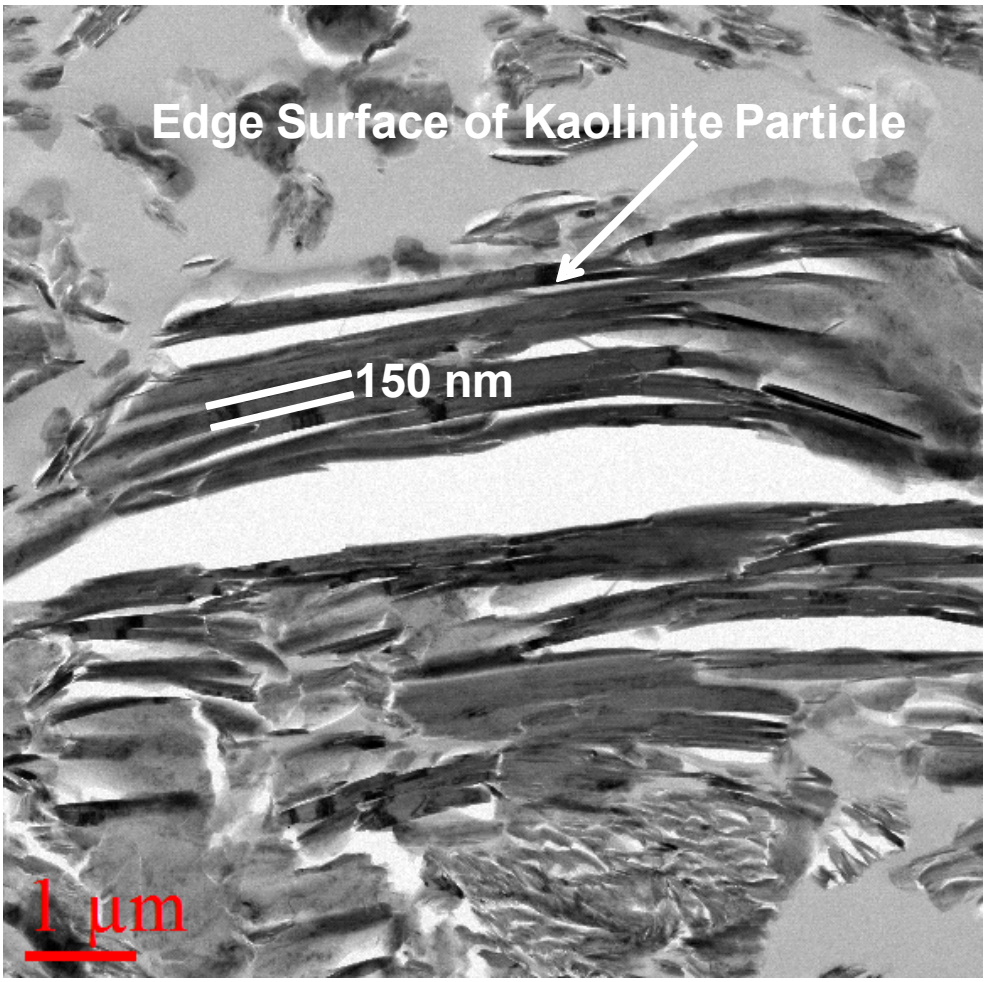

Figure 7.1- Low magnification TEM image showing the edges of kaolinite particles.

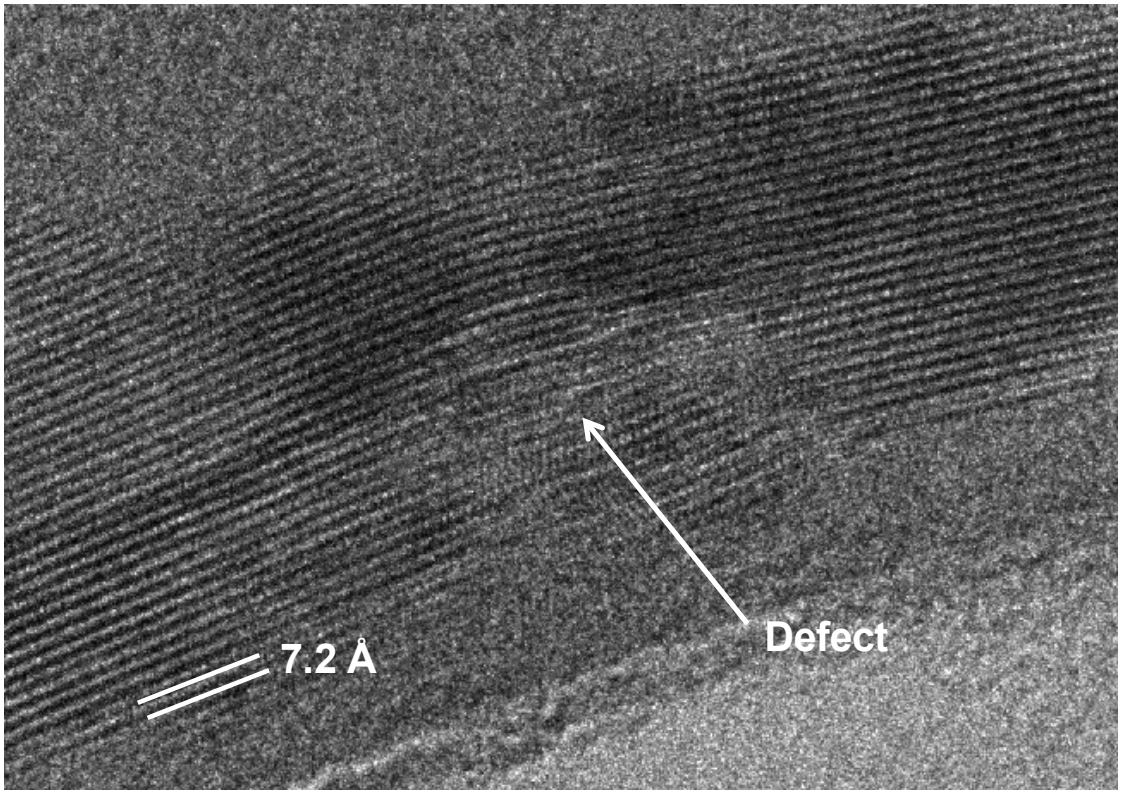

Figure 7.2- Lattice fringe images of kaolinite showing c-spacing of 0.72 nm.

indicating that the kaolinite is indeed 1:1 bilayer structure consisting of the silica tetrahedral and the alumina octahedral sheets [22, 197, 199, 207]. Figure 7.2 also shows the stacking defect (bending of several layers) in the kaolinite particle. Out of fourteen particles examined, only one showed this stacking fault. Plancon *et al.* [208] also observed similar defects during their investigation of kaolinite samples. Ma and Eggleton [197] also observed defects in lattice fringes of kaolinite stacks, such as dislocations and layer terminations in primary kaolinites and deformations at the nanoscale (i.e., bending of several layers) are common in transported kaolinites. These defect structures are not only important to crystal chemistry, but also suggestive of the stability relationships between the kaolinite layers.

Figure 7.3 shows the lattice fringe image of another kaolinite particle showing two different c-spacings of 7.2 Å and 10 Å. The c-spacing of 7.2 Å for the kaolinite particle was consistent with the previous image of kaolinite particle, as shown in Figure 7.2. The increased c-spacing of 10 Å in stacks of kaolinite particles was also reported in the literature [197, 199], and has been attributed to 2:1 type layer structures such as smectite. These mixed layer silicates – kaolinite (1:1) and smectite (2:1), affect the electrokinetic properties of these particles when suspended in water. Not only is the surface charge of the kaolinite particles influenced by the presence of these 2:1 layer particles, these 2:1 layer structures may also correspond to a weak zone where the particles will cleave, and expose a 2:1 type layer structure at both faces of the kaolinite particle, as explained in Figure 7.4. This defect may have a significant effect on the electrokinetic properties of kaolinite particles dominated by the silica tetrahedral sheet at

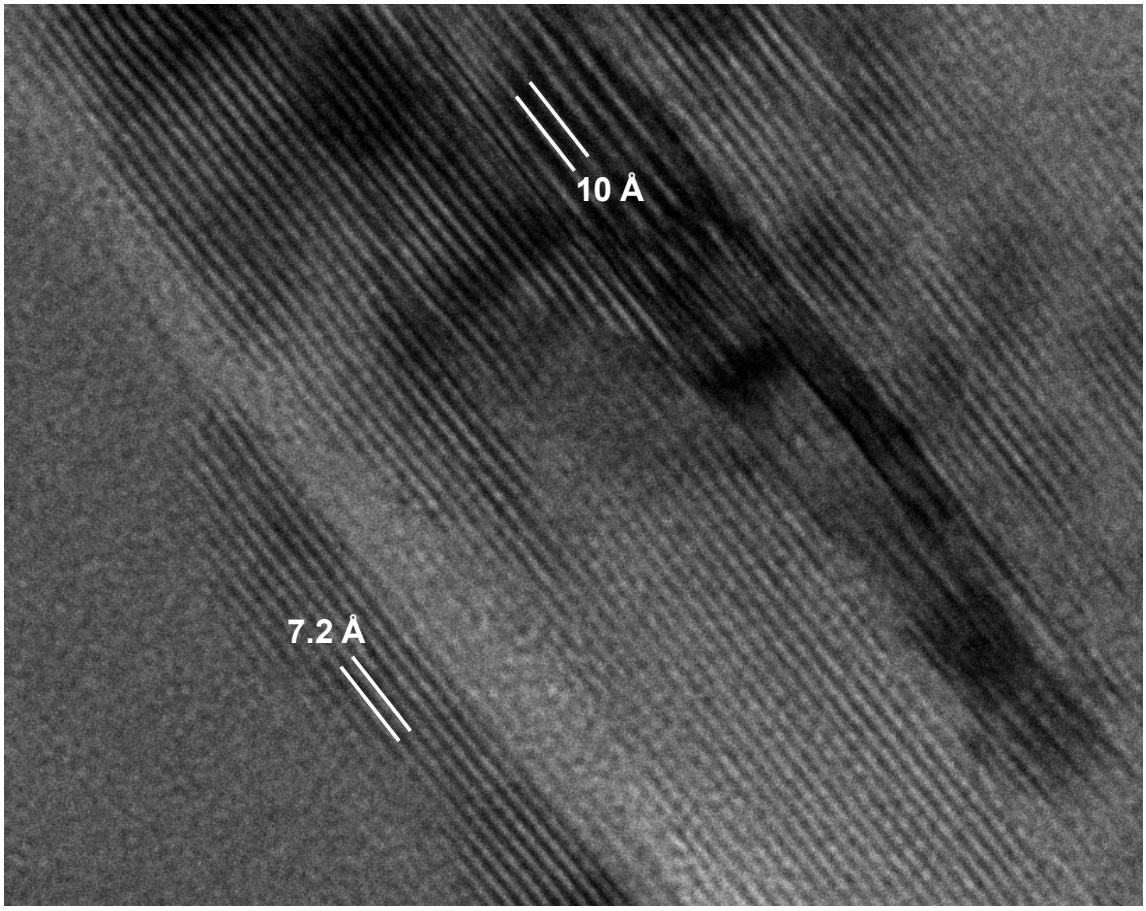

Figure 7.3- Lattice fringe pattern of kaolinite along 001 basal plane.

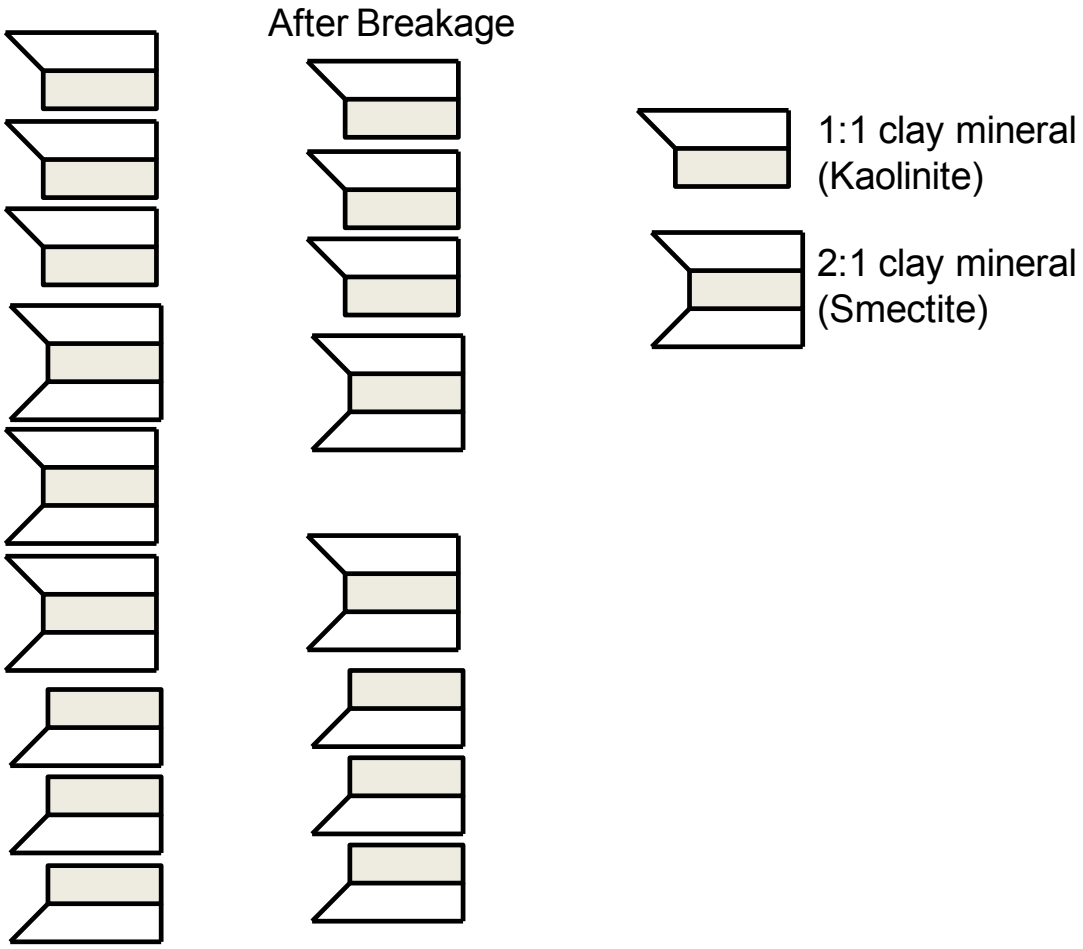

Figure 7.4- Schematic diagram of kaolinite with mixed-layer silicate showing that after cleavage the kaolinite particle may consist of silica a tetrahedral sheet at both faces.

both faces. Out of 14 particles examined with HRTEM, two particles showed this mixed layer silicates of 2:1 type intercalated between the stacks of kaolinite bilayers.

A third type of stacking was also observed with HRTEM imaging which shows a c-spacing of 10 Å, as shown in Figure 7.5. This increased c-spacing of 10 Å corresponds to 2:1 type clay minerals such as smectite [197, 199]. There was another lattice fringe observed at 3.7 Å, which may arise from the octahedral sheet of 2:1 type clay minerals. The co-existence of single smectite-type clay minerals with kaolinite particles will affect its surface properties, particularly its electrokinetic and rheological properties when the particles are prepared in suspension. Examination of the literature has revealed different values of cation exchange capacity (CEC) for kaolinite from 36 to100 μ-mole/g, depending on the source of kaolinite and type of counterions [30-32]. This wide variation in CEC among different samples of kaolinite may exist when the 2:1 type clay minerals such as pyrophyllite with low CEC or smectite with high CEC are intermixed with kaolinite particles [197]. Ferris and Jepson [29] analyzed the same kaolinite sample as was used in this dissertation research and found a very low or no definite cation exchange capacity. The implication is that the kaolinite used in this research may be intermixed with traces of 2:1 pyrophyllite-like clay minerals with low CEC. Despite the variation in CEC for kaolinite, there is a common consensus among researchers that kaolinite has very small cation exchange capacity in contrast to some other clay minerals such as smectite.

The electrokinetic characterization of silica and gibbsite particles has revealed a point of zero charge (PZC) at pH 2-3 and 8-9, respectively [15, 209]. It is expected that

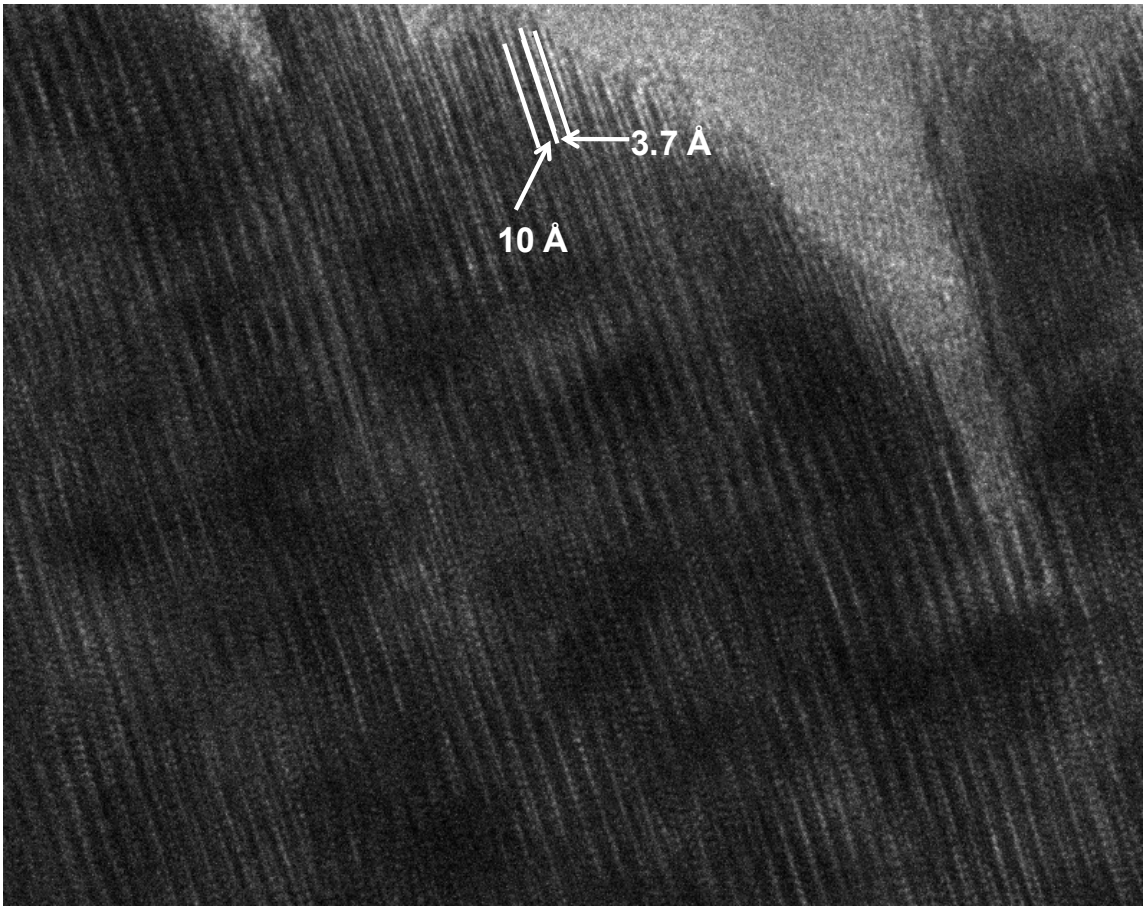

Figure 7.5- HRTEM image showing a smectite layer.

particles composed of bilayers of one silica sheet (silica tetrahedral sheet) and another alumina sheet (alumina octahedral sheet) such as ideal particles having one silica face and one alumina face, kaolinite will have a PZC which would be the average of pure silica particles and pure alumina particles,. i.e., about pH 5-6. However, many researchers have reported a lower PZC at pH < 3 for kaolinite as determined by electrophoresis [29, 39-45, 52]. It is evident that the electrophoresis technique for surface charge characterization is compromised by the heterogeneous charge character and platy shape of kaolinite particles, and does not reveal the true surface charge characteristics of kaolinite. In addition to the above, the surface charge properties of kaolinite particles will also be compromised by the presence of 2:1 clay layer defects which may be present in the kaolinite structure (Figure 7.3) or by 2:1 clay particles (Figure 7.5) present as trace impurities, as revealed from the HRTEM results. Ma and Eggleton [197] have observed kaolinite stacks ended on one side or both sides by a 2:1 type structure. The presence of these 2:1 structures in the kaolinite sample will increase the silica dominance in kaolinite, and thereby may shift the PZC towards a lower pH value. The surface charge properties of kaolinite will therefore be affected by the presence of these 2:1 layer clay minerals.

The potentiometric titration is another technique to measure surface charge of particles which gave relatively higher PZC for kaolinite as pH 4.72. These results are in good agreement with the PZC values reported in the literature as pH 4.3 [34], pH 4.5 [38] and pH 4.6 [161]. Though a bit higher PZC is obtained by potentiometric titration, this value is still lower than the expected PZC of pH 5-6. These results indicate the presence of other 2:1 layer clay minerals which may be present with kaolinite, affecting its surface charge properties and lowering its PZC.

It is clear from this study and other published studies that the surface charge properties of kaolinite might be complicated by the presence of small amounts of 2:1 layer clay minerals. HRTEM seems to be a reliable method to identify the surface layer types of kaolinite. In order to better understand the surface chemistry of kaolinite, it is highly important to quantify the presence of 2:1 layer clay minerals using HRTEM.

7.5 Summary

HRTEM is an appropriate and reliable technique to describe defect structures and impurities in kaolinite samples. The lattice fringe images of Cornwall kaolinite from HRTEM always showed that the kaolinite occurs as a bilayer structure with c-spacing of 7.2 Å. Occasionally, there were defects such as bending of layers observed in the stacks of kaolinite. The 2:1 type clay minerals were also revealed in this study with increased c-spacing of 10 Å. These 2:1 type clay minerals, trilayer structure, seem to exist in between bilayers of kaolinite or as single particles. The surface chemistry of kaolinite particularly may be affected by the presence of even a small amount of 2:1 type clay minerals and may shift the PZC of kaolinite towards lower pH. Further investigation should be conducted in order to quantify the effect of trilayer clay minerals in primary kaolinite particles.

CHAPTER 8

CONCLUSIONS AND FUTURE RESEARCH

The major objective of this dissertation research was to investigate the surface chemistry of kaolinite particles, in regards to composition, morphology, surface charge properties of its faces, rheological properties and particle interactions. Last, but not least was the identification of the silica face, the alumina face and the edge surface of kaolinite particles. In this regard, all objectives have been achieved using a high purity kaolinite sample from Cornwall, UK. In particular, the following summaries describe the accomplishments and contributions.

A pool of advanced analytical techniques utilized in this dissertation research such as XRF, XRD, SEM, AFM, FTIR and ISS has explored the detailed morphological and surface chemistry features of kaolinite. X-ray fluorescence (XRF) spectrometry determined the chemical composition of kaolinite, and thereby predict the structural formula as $(Si_{3.94}Al_{0.06})^{IV}(Al_{3.99}Fe_{0.01})^{VI}O_{10}(OH)_8.Fe_{0.01}Ca_{0.01}Mg_{0.01}K_{0.02}Na_{0.005}$. X-ray diffraction study (XRD) showed that kaolinite was the dominant mineral phase with some minor impurities of quartz and anatase. Scanning electron microscopy (SEM) and atomic force microscopy (AFM) confirmed the platy nature and hexagonal to subhedral shape of kaolinite. The median diameter and thickness of kaolinite from Cornwall, UK were

determined as 600 nm and 11 nm, respectively. The surface chemistry features as revealed by Fourier transform infrared spectroscopy (FTIR) determined the OH group vibrations of the kaolinite surface from the inner OH group stretching vibrations at 3620 cm^{-1}, and inner-surface OH group vibrations at 3691 cm^{-1}, 3668 cm^{-1} and 3651 cm^{-1}. Low energy ion scanning spectroscopy (ISS) revealed an overlapping band of Si/Al elements detected from both the silica and alumina faces of kaolinite.

AFM surface force measurements revealed that the silica tetrahedral face of kaolinite is negatively charged at pH > 4, whereas the alumina octahedral face of kaolinite is positively charged at pH < 6, and negatively charged at pH > 8. The results suggest that the iso-electric point of the silica tetrahedral face is at pH < 4, and that the iso-electric point of the alumina octahedral face lies between pH 6 and 8. These results contradict the generally accepted view that basal plane surfaces of kaolinite carry a permanent negative charge due to minor substitution of Al^{3+} for Si^{4+} in the silica tetrahedral layer, and suggest some surface charge dependency of the two faces with respect to solution pH.

The electrokinetic properties of kaolinite are complicated by its anisotropic features – nonuniform surface charge densities on the faces (the silica face, the alumina face and the edge surfaces) and its platy-shaped. Using Smoluchowski's classical model, the iso-electric point for kaolinite was determined at less than pH 3. The surface charge properties of kaolinite were also determined experimentally using traditional titration techniques such as M-R titration and potentiometric titration, and using a new technique by surface force measurements with atomic force microscopy. The point of zero charge was determined as pH 4.5 by titration techniques, which is in good agreement with the

iso-electric point in between pH 4 and 5 determined by surface force measurements. It was found that the surface charge densities of kaolinite particles are better characterized by titration and surface force measurements.

Results from kaolinite particle interactions indicate that the silica face–alumina face interaction is dominant for kaolinite particle aggregation at low pH, pH4. This face–face association increases the stacking of kaolinite layers, and thereby promotes the edge–face (edge–silica face and edge–alumina face) and face–face (silica face–alumina face) associations with increasing pH and hence, the maximum shear yield stress at pH 5-5.5. The face–face association at low pH has been confirmed from cryo-SEM images of kaolinite aggregates taken from suspension which show that the particles are mostly organized in a face–face and edge–face manner. At higher pH conditions, the cryo-SEM images of the kaolinite aggregates reveal a lower degree of consolidation and the edge–edge association is evident.

Crystal lattice resolution images reveal the hexagonal surface lattice for both the silica and alumina faces of kaolinite. Analysis of the silica face of kaolinite showed that the hexagonal surface lattice ring of oxygen atoms had a periodicity of 0.50 ± 0.04 nm between neighboring oxygen atoms, which is in good agreement with the surface lattice structure of the mica basal plane. The center of the hexagonal ring of oxygen atoms is vacant. Analysis of the alumina face of kaolinite showed that the hexagonal surface lattice ring of hydroxyls surround a hydroxyl in the center of the ring. The atomic spacing between neighboring hydroxyls was determined as 0.36 ± 0.04 nm.

High resolution transmission electron microscopy investigation of kaolinite has indicated that kaolinite is indeed composed of bilayers of silica tetrahedral sheet

covalently bonded to an alumina octahedral sheet. The stacked bilayers have a c-spacing of 7.2 Å. Occasionally, defects in the form of bending of bilayers was observed in the stack of bilayers composing a kaolinite particle. HRTEM has also indicated that some particles have a 2:1 type clay mineral in the stack of bilayers with an increased c-spacing of 10 Å under these circumstances.

As noted in previous paragraphs, a number of important contributions have been made, but perhaps most important has been the protocol of surface force measurements for kaolinite particles. It is expected that this protocol can be used to good advantage for the surface clay study of other clay minerals in future research.

During this dissertation research, we have found that direct measurement of the surface charge densities of the edge surface though highly desired is difficult at the moment due to their nanosize exposure. Preparation of such edge surface is difficult. It is our hope that future research will focus in this direction to develop new techniques for preparing edge surfaces of kaolinite with no contamination from basal plane surfaces. This would help researchers to better understand the surface chemistry of kaolinite, and to better control their surface properties.

Another aspect of this dissertation research was to investigate the electrophoretic motion of kaolinite particles. This objective was met with the design of appropriate experimental techniques such as potentiometric titration and surface force measurements. An appropriate theoretical model to describe the electrophoretic mobilities of such anisotropic particles is highly desired, and a good review of ongoing work is already discussed in this dissertation. The review should provide a framework for the

development of such a procedure to study the electrokinetic properties of kaolinite and other clay minerals in the future.

Finally with regard to future research, in addition to the surface charge characteristics of clay surfaces, the hydrophobic properties of clay faces should be considered. For many engineered systems such as flotation, the surface wetting characteristics along with surface charge properties will be equally important in order to understand and control the behavior of these particles in a flotation system. The fundamental wetting characteristics of different clay faces − the silica face, the alumina face, and the edge surface, would help us understand and better control the behavior of clay particles in flotation separations as well as in other applications where suspensions and pastes of clay particles are used.

REFERENCES

[1] H.H. Murray, Applied Clay Science 5 (1991) 379.

[2] L.E. Taylor, J.A. Hillier, A.J. Benham, A.C. MacKenzie, S. British Geological, World Mineral Production 1999-2003. British Geological Survey, Nottingham, 2005.

[3] Y. Hu, X. Liu, Minerals Engineering 16 (2003) 1279.

[4] Y.-h. Hu, W. Sun, X.-w. Liu, D.-z. Wang, Transactions of Nonferrous Metals Society of China 13 (2003) 1430.

[5] Y. Hu, H. Jiang, D. Wang, Minerals Engineering 16 (2003) 1221.

[6] Y. Hu, X. Liu, Z. Xu, Minerals Engineering 16 (2003) 219.

[7] Y. Hu, S. Wei, J. Hao, J.D. Miller, K. Fa, International Journal of Mineral Processing 76 (2005) 163.

[8] W.-q. Qin, G.-z. Qiu, Y.-h. Hu, Transactions of Nonferrous Metals Society of China 13 (2003) 679.

[9] L.-y. Xia, H. Zhong, G.-y. Liu, Z.-q. Huang, Q.-w. Chang, X.-g. Li, Transactions of Nonferrous Metals Society of China 19 (2009) 446.

[10] R.J. Chalaturnyk, J.D. Scott, B. Ozum, Pet. Sci. Technol. 20 (2002) 1025.

[11] Fine Tailings Fundamentals Consortium, Advances in Oil Sands Tailings Research. Alberta Dept. of Energy, Oil Sands and Research Division, Alberta, Canada, 1995.

[12] M.E. Schrader, G.I. Loeb, Editors, Modern Approaches to Wettability: Theory and Applications. Plenum, 1992.

[13] K. Ma, A.C. Pierre, Clays and Clay Minerals 47 (1999) 522.

[14] E. Wieland, W. Stumm, Geochim. Cosmochim. Acta 56 (1992) 3339.

[15] J.D. Miller, J. Nalaskowski, B. Abdul, H. Du, Canadian Journal of Chemical Engineering 85 (2007) 617.

[16] H.V. Olphen, An Introduction to Clay Colloid Chemistry : For Clay Technologists, Geologists and Soil Scientists. Interscience, New York, 1963.

[17] W.A. Deer, R.A. Howie, J. Zussman, An Introduction to the Rock-Forming Minerals. Wiley, New York, 1966.

[18] G.H. Bolt, M.G.M. Bruggenwert, Editors, Developments in Soil Science, Vol. 5A: Soil Chemistry, Pt. A: Basic Elements. Elsevier, 1976.

[19] G.H. Bolt, Editor, Developments in Soil Science, Vol. 5B: Soil Chemistry, B. Physicochemical Models. Elsevier Scientific Publishing Company, 1979.

[20] J.B. Dixon, S.B. Weed, Editors, Minerals in Soil Environments. Soil Sci. Soc. Am., 1977.

[21] D.J. Greenland, M.H.B. Hayes, Editors, The Chemistry of Soil Constituents. Wiley, 1978.

[22] G.W. Brindley, G. Brown, Editors, Mineralogical Society Monograph, No. 5: Crystal Structures of Clay Minerals and Their X-ray Identification. Mineralogical Society, 1980.

[23] R.K. Schofield, H.R. Samson, Discussions of the Faraday Society 18 (1954) 135.

[24] J. Lyklema, Fundamentals of Interface and Colloid Science, Volume II: Solid-Liquid Interfaces. Academic Press, 1995.

[25] J.A. Kittrick, Am. Mineral. 51 (1966) 1457.

[26] B. Rand, I.E. Melton, Journal of Colloid and Interface Science 60 (1977) 308.

[27] R.K. Schofield, Br. Clayworker 47 (1938) 208.

[28] A.W. Flegmann, J.W. Goodwin, R.H. Ottewill, Proceedings of the British Ceramic Society (1969) 31.

[29] A.P. Ferris, W.B. Jepson, Journal of Colloid and Interface Science 51 (1975) 245.

[30] N.C. Brady, The Nature and Properties of Soils. 9th Ed. Macmillan, 1984.

[31] F. Adams, Editor, Agronomy, No. 12: Soil Acidity and Liming. 2nd Ed. American Society of Agronomy, Inc., Crop Science Society of America, Inc., Soil Science Society of America, Inc., 1984.

[32] R.K. Schofield, J. Soil Sci. 1 (1949) 1.

[33] P.W. Schindler, P. Liechti, J.C. Westall, Neth. J. Agric. Sci. 35 (1987) 219.

[34] P.V. Brady, R.T. Cygan, K.L. Nagy, Journal of Colloid and Interface Science 183 (1996) 356.

[35] P.V. Brady, R.T. Cygan, K.L. Nagy, in: A.J. Everett, (Ed.) Adsorption of Metals by Geomedia; Academic Press, San Diego, 1998, p. 371.

[36] B.K. Schroth, G. Sposito, Clays and Clay Minerals 45 (1997) 85.

[37] F. Huertas, L. Chou, R. Wollast, Geochimica et Cosmochimica Acta (1999) 3261.

[38] M.M. Motta, C.F. Miranda, Soil Science Society of America Journal 53 (1989) 380.

[39] R.W. Smith, Y. Narimatsu, Miner. Eng. 6 (1993) 753.

[40] J.M. Cases, C. Touret-Poinsignon, D. Vestier, C. R. Acad. Sci., Ser. C 272 (1971) 728.

[41] D.J.A. Williams, K.P. Williams, Journal of Colloid and Interface Science 65 (1978) 79.

[42] S.B. Johnson, D.R. Dixon, P.J. Scales, Colloids and Surfaces, A: Physicochemical and Engineering Aspects 146 (1999) 281.

[43] S.K. Nicol, R.J. Hunter, Australian Journal of Chemistry 23 (1970) 2177.

[44] A.C. Pierre, K. Ma, J. Mater. Sci. 32 (1997) 2937.

[45] J. Yuan, R.J. Pruett, Minerals and Metallurgical Processing 15 (1998) 50.

[46] M.S. Çelik, in: S. Fernando Wypych and Kestur Gundappa, (Eds.) Interface Science and Technology; Elsevier, 2004, p. 57.

[47] P.F. Luckham, S. Rossi, Advances in Colloid and Interface Science 82 (1999) 43.

[48] N. Street, Australian Journal of Chemistry 9 (1956) 467.

[49] S.B. Johnson, A.S. Russell, P.J. Scales, Colloids and Surfaces A: Physicochemical and Engineering Aspects 141 (1998) 119.

[50] S.B. Johnson, G.V. Franks, P.J. Scales, D.V. Boger, T.W. Healy, International Journal of Mineral Processing 58 (2000) 267.

[51] I. Sondi, O. Milat, V. Pravdic, Journal of Colloid and Interface Science 189 (1997) 66.

[52] C. Chassagne, F. Mietta, J.C. Winterwerp, Journal of Colloid and Interface Science 336 (2009) 352.

[53] F. Franco, L.A. Perez-Maqueda, J.L. Perez-Rodriguez, Journal of Colloid and Interface Science 274 (2004) 107.

[54] J. Cuadros, T. Dudek, Clays and Clay Minerals 54 (2006) 1.

[55] E. Balan, A.M. Saitta, F. Mauri, G. Calas, American Mineralogist 86 (2001) 1321.

[56] E. Burdukova, G.C. Van Leerdam, F.E. Prins, R.G. Smeink, D.J. Bradshaw, J.S. Laskowski, Miner. Eng. 21 (2008) 1020.

[57] C.T. Johnston, Clay Miner. 45 (2010) 245.

[58] M. Zbik, R.S.C. Smart, Minerals Engineering 15 (2002) 277.

[59] M. Zbik, R.S.C. Smart, Clays Clay Miner. 46 (1998) 153.

[60] D.W. Thompson, J.J. MacMillan, D.A. Wyatt, Journal of Colloid and Interface Science 82 (1981) 362.

[61] M. Zbik, R.S.C. Smart, Clays for Our Future, Proceedings of the International Clay Conference, 11th, Ottawa, Ont., June 15-21, 1997 (1997) 361.

[62] B.R. Bickmore, K.L. Nagy, P.E. Sandlin, T.S. Crater, American Mineralogist 87 (2002) 780.

[63] C.C. Harvey, H.H. Murray, Appl. Clay Sci. 11 (1997) 285.

[64] C.B. Maxwell, Z. Zhang, H.H. Murray, Thiele Kaolin Company, USA. Patent Application: 6379452 US, 2002, p. 5.

[65] H.H. Murray, Clays Clay Minerals 10 (1963) 291.

[66] H.H. Murray, International Journal of Mineral Processing 7 (1980) 263.

[67] H.H. Murray, Kirk-Othmer, Encyclopedia of Chemical Technology. 5th Ed. 6 (2004) 685.

[68] M.S. Prasad, K.J. Reid, H.H. Murray, Applied Clay Science 6 (1991) 87.

[69] T.M. Herrington, A.Q. Clarke, J.C. Watts, Colloids and Surfaces 68 (1992) 161.

[70] B. Rand, I.E. Melton, Nature (London, United Kingdom) 257 (1975) 214.

[71] A.E. James, D.J.A. Williams, Advances in Colloid and Interface Science 17 (1982) 219.

[72] V. Gupta, J.D. Miller, Journal of Colloid and Interface Science 344 (2010) 362.

[73] V.C. Farmer, Science (Washington, DC, U. S.) 145 (1964) 1189.

[74] J.M. Cases, P. Cunin, Y. Grillet, C. Poinsignon, J. Yvon, Clay Miner. 21 (1986) 55.

[75] M.S. Zbik, R.L. Frost, Y.-F. Song, Journal of Colloid and Interface Science 319 (2008) 169.

[76] C. Liu, X. Li, F. Xu, P.M. Huang, Soil Science and Plant Nutrition (Tokyo, Japan) 49 (2003) 17.

[77] J.I. Bidwell, W.B. Jepson, G.L. Toms, Clay Minerals 8 (1970) 445.

[78] L.S. Birks, X-Ray Spectrochemical Analysis (Chemical Analysis, Vol. 11). 2nd Ed. Wiley-Interscience, 1969.

[79] R. Jenkins, Introduction to X-Ray Spectrometry. Heyden, 1977.

[80] R. Jenkins, X-Ray Fluorescence Spectrometry. ACS, 1978.

[81] R. Jenkins, Chemical Analysis, Vol. 99: X-Ray Fluorescence Spectrometry. John Wiley and Sons, 1988.

[82] R. Jenkins, X-Ray Fluorescence Spectrometry, 2nd Ed. In: Chem. Anal. (N. Y.), 1999; 152. Wiley, 1999.

[83] R. Tertian, F. Claisse, Principles of Quantitative X-Ray Fluorescence Analysis. Heyden, 1982.

[84] H.P. Klug, L.E. Alexander, X-Ray Diffraction Procedures for Polycrystalline and Amorphous Materials. 2nd Ed. Wiley-Interscience, 1974.

[85] B.D. Cullity, S.R. Stock, Elements of X-Ray Diffraction, 3rd Ed. Prentice Hall, 2001.

[86] D.L. Bish, J.E. Post, Am. Mineral. 78 (1993) 932.

[87] D.L. Bish, Soil Sci. Soc. Am. Proc., 1994, p 267.

[88] D.M. Moore, R.C. Reynolds, X-ray Diffraction and the Identification and Analysis of Clay Minerals, 2nd Ed. Oxford Univ Press, 1997.

[89] O.C. Wells, A. Boyde, E. Lifshin, A. Rezanowich, Scanning Electron Microscopy. McGraw-Hill, 1974.

[90] G. Binnig, C.F. Quate, C. Gerber, Physical Review Letters 56 (1986) 930.

[91] M.F. Hochella, Jr., Reviews in Mineralogy 23 (1990) 87.

[92] S.M. Clark, J.D. Baldeschwieler, Rev. Sci. Instrum. 64 (1993) 904.

[93] P.K. Hansma, B. Drake, D. Grigg, C.B. Prater, F. Yashar, G. Gurley, V. Elings, S. Feinstein, R. Lal, Journal of Applied Physics 76 (1994) 796.

[94] N. Kato, I. Suzuki, H. Kikuta, K. Iwata, Rev. Sci. Instrum. 66 (1995) 5532.

[95] G.M. Bancroft, J.R. Brown, W.S. Fyfe, Anal. Chem. 49 (1977) 1044.

[96] A.R. Gonzalez-Elipe, J.P. Espinos, G. Munuera, J. Sanz, J.M. Serratosa, J. Phys. Chem. 92 (1988) 3471.

[97] H. Seyama, M. Soma, Kokuritsu Kogai Kenkyusho Kenkyu Hokoku 111 (1988) p. 125.

[98] J.W. Stucki, C.B. Roth, W.E. Baitinger, Clays Clay Miner. 24 (1976) 289.

[99] M.F. Hochella, Jr., Rev. Mineral. 18 (1988) 573.

[100] W.P. Inskeep, E.A. Nater, P.R. Bloom, D.S. Vandervoort, M.S. Erich, Geochim. Cosmochim. Acta 55 (1991) 787.

[101] R.B. Borade, A. Adnot, S. Kaliaguine, J. Catal. 126 (1990) 26.

[102] M.H. Koppelman, A.B. Emerson, J.G. Dillard, Clays Clay Miner. 28 (1980) 119.

[103] R.K. Vempati, R.H. Loeppert, D.L. Cocke, Solid State Ionics 38 (1990) 53.

[104] R.K. Vempati, R.H. Loeppert, D.C. Dufner, D.L. Cocke, Soil Sci. Soc. Am. J. 54 (1990) 695.

[105] A.W. Czanderna, Editor, Methods and Phenomena, Their Applications in Science and Technology, Vol. 1: Methods of Surface Analysis. Elsevier, 1975.

[106] E.G. Brame, Jr., J.G. Grasselli, Editors, Practical Spectroscopy Series, Vol. 1, Pt. A: Infrared and Raman Spectroscopy. Marcel Dekker, 1977.

[107] R.G. Messerschmidt, M.A. Harthcock, Editors, Practical Spectroscopy Series, Vol. 6: Infrared Microspectroscopy: Theory and Applications. Marcel Dekker, Inc., 1988.

[108] N.J. Everall, J.M. Chalmers, A. Local, S. Allen, Vib. Spectrosc. 10 (1996) 253.

[109] E.G. Brame, Jr., J.G. Grasselli, Editors, Practical Spectroscopy Series, Vol. 1, Pt. B: Infrared and Raman Spectroscopy. Dekker, 1977.

[110] E.G. Brame, Jr., J.G. Grasselli, Editors, Practical Spectroscopy Series, Vol. 1, Pt. C: Infrared and Raman Spectroscopy. Dekker, 1977.

[111] N.J. Harrick, Am. Lab. (Fairfield, Conn.) 20 (1988) 98.

[112] L. Hupka. Particle-Surface Interactions in Post-Lap Cleaning of Alumina/Titanium Carbide Wafers. The University of Utah, Salt Lake City, 2006.

[113] A.D. Karathanasis, Soil Science Society of America Book Series 5 (2008) 465.

[114] C. Ma, R.A. Eggleton, Clays and Clay Minerals 47 (1999) 174.

[115] V.C. Farmer, Clay Miner. 33 (1998) 601.

[116] H.H. Murray, Appl. Clay Sci. 17 (2000) 207.

[117] K.L. Konan, C. Peyratout, J.-P. Bonnet, A. Smith, A. Jacquet, P. Magnoux, P. Ayrault, Journal of Colloid and Interface Science 307 (2007) 101.

[118] J. Drelich, J. Long, Z. Xu, J. Masliyah, C.L. White, J. Colloid Interface Sci. 303 (2006) 627.

[119] S. Veeramasuneni, M.R. Yalamanchili, J.D. Miller, J. Colloid Interface Sci. 184 (1996) 594.

[120] I. Larson, C.J. Drummond, D.Y.C. Chan, F. Grieser, Langmuir 13 (1997) 2109.

[121] M.R. Yalamanchili, S. Veeramasuneni, M.A.D. Azevedo, J.D. Miller, Colloids Surf., A 133 (1998) 77.

[122] G.V. Franks, L. Meagher, Colloids Surf., A 214 (2003) 99.

[123] S. Assemi, J. Nalaskowski, J.D. Miller, W.P. Johnson, Langmuir 22 (2006) 1403.

[124] J.I. Bidwell, W.B. Jepson, G.L. Toms, Clay Minerals 8 (1970) 445.

[125] J. Nalaskowski, J. Drelich, J. Hupka, J.D. Miller, Langmuir 19 (2003) 5311.

[126] W.A. Ducker, T.J. Senden, R.M. Pashley, Nature (London) 353 (1991) 239.

[127] J. Drelich, J. Long, A. Yeung, Can. J. Chem. Eng. 85 (2007) 625.

[128] X. Yin, J. Drelich, Langmuir 24 (2008) 8013.

[129] V. Médout-Marère, Journal of Colloid and Interface Science 228 (2000) 434.

[130] L. Bergstrom, Advances in Colloid and Interface Science 70 (1997) 125.

[131] T. Arai, D. Aoki, Y. Okabe, M. Fujihira, Thin Solid Films 273 (1996) 322.

[132] B.V. Zhmud, J. Sonnefeld, L. Bergstrom, Colloids Surf., A 158 (1999) 327.

[133] I. Sokolov, Q.K. Ong, H. Shodiev, N. Chechik, D. James, M. Oliver, J. Colloid Interface Sci. 300 (2006) 475.

[134] M. Kosmulski, Chemical Properties of Material Surfaces. In: Surfactant Sci. Ser., 2001; 102. Marcel Dekker, Inc., 2001.

[135] R. Raiteri, B. Margesin, M. Grattarola, Sensors and Actuators B: Chemical 46 (1998) 126.

[136] Z. Zhou, W.D. Gunter, Clays and Clay Minerals 40 (1992) 365.

[137] Z. Fu, M.M. Santore, Langmuir 14 (1998) 4300.

[138] C.C. Harvey, G. Lagaly, in: B.K.G. Theng, Faïza Bergaya, L. Gerhard, (Eds.) Developments in Clay Science; Elsevier, 2006, p. 501.

[139] H. H. Murray, J.E. Kogel, Applied Clay Science 29 (2005) 199.

[140] H.H. Murray, Applied Clay Science (1977) 29.

[141] H.H. Murray, J.E. Kogel, Applied Clay Science 29 (2005) 199.

[142] N. Street, A.S. Buchanan, Australian Journal of Chemistry 9 (1956) 450.

[143] E. Tombácz, M. Szekeres, Applied Clay Science 34 (2006) 105.

[144] C. Galassi, A.L. Costa, P. Pozzi, Clays and Clay Minerals 49 (2001) 263.

[145] G. Sposito, Environ. Sci. Technol. 32 (1998) 2815.

[146] W. Stumm, Chemistry of the Solid-Water Interface: Processes at the Mineral-Water and Particle-Water Interface in Natural Systems. Wiley, New York, 1992.

[147] A.L. Mular, R.B. Roberts, Transactions of the Canadian Institute of Mining and Metallurgy 69 (1966) 438.

[148] R.J. Hunter, Editor, Colloid Science: Zeta Potential in Colloid Science: Principles and Applications. Academic Press, 1981.

[149] H.J. Butt, K. Graf, M. Kappl, Physics and Chemistry of Interfaces. Wiley-VCH, 2003.

[150] J.H. Masliyah, S. Bhattacharjee, Electrokinetic and Colloid Transport Phenomena. John Wiley & Sons, Inc., 2006.

[151] S.L. Carnie, G.M. Torrie, in: S.A. Rice, I. Prigogine, (Eds.) Advances in Chemical Physics, 2007, p. 141.

[152] L. Blum, in: S.A. Rice, I. Prigogine, (Eds.) Advances in Chemical Physics, 2007, p. 171.

[153] M. Quesada-Pérez, E. González-Tovar, A. Martín-Molina, M. Lozada-Cassou, R. Hidalgo-Álvarez, ChemPhysChem 4 (2003) 234.

[154] D.C. Henry, Proc. R. Soc. London, Ser. A 133 (1931) 106.

[155] J.L. Anderson, Journal of Colloid and Interface Science 105 (1985) 45.

[156] M.C. Fair, J.L. Anderson, Journal of Colloid and Interface Science 127 (1989) 388.

[157] J.D. Sherwood, H.A. Stone, Phys. Fluids 7 (1995) 697.

[158] B. Braggs, D. Fornasiero, J. Ralston, R. St. Smart, Clays and Clay Minerals 42 (1994) 123.

[159] G.K. Korpi. Electrokinetic and Ion Exchange Properties of Aluminum Oxide and Hydroxides. 1965.

[160] M. Alvarez-Silva, A. Uribe-Salas, M. Mirnezami, J.A. Finch, Minerals Engineering 23 (2010) 383.

[161] A.C. Riese. Adsorption of Radium and Thorium onto Quartz and Kaolinite: A Comparison of Solution/Surface Equilibria Models. Colorado School of Mines, Golden, 1982.

[162] Z. Xie, J.V. Walther, Geochim. Cosmochim. Acta 56 (1992) 3357.

[163] V. Gupta, J.D. Miller, A.V. Nguyen, Conference of Metallurgists Proceedings; MetSoc, Vancouver, BC, 2010.

[164] N.R. O'Brien, Clays and Clay Minerals, Proceedings of the Conference 19 (1971) 353.

[165] A. Casagrande, Boston Society of Civil Engineers Proceedings, 1940, p. 72.

[166] T.W. Lambe, American Society of Civil Engineers Proceedings, 1953, p. 1.

[167] T.K. Tan, 4th International Conference on Soil Mechanics and Foundation Engineering Proceedings, 1958, p. 87.

[168] I.T. Rosenqvist, Norwegian Geotechnical Institute Proceedings, 1963, p. 1.

[169] I.T. Rosenqvist, American Society of Civil Engineers Proceedings, 1959, p. 31.

[170] M.S. Zbik, R.S.C. Smart, G.E. Morris, Journal of Colloid and Interface Science 328 (2008) 73.

[171] M.S. Zbik, R.L. Frost, Journal of Colloid and Interface Science 339 (2009) 110.

[172] A.V. Nguyen, H.J. Schulze, Colloidal Science of Flotation. Marcel Dekker, Inc., 2004.

[173] R.B. Secor, C.J. Radke, Journal of Colloid and Interface Science 103 (1985) 237.

[174] F.R.C. Chang, G. Sposito, Journal of Colloid and Interface Science 163 (1994) 19.

[175] M. Zbik, R.G. Horn, Colloids and Surfaces A: Physicochemical and Engineering Aspects 222 (2003) 323.

[176] T.R. Albrecht, C.F. Quate, Journal of Vacuum Science & Technology, A: Vacuum, Surfaces, and Films 6 (1988) 271.

[177] Y. Sugawara, T. Ishizaka, S. Morita, Journal of Vacuum Science & Technology, B: Microelectronics and Nanometer Structures 9 (1991) 1092.

[178] T.R. Albrecht, C.F. Quate, Journal of Applied Physics 62 (1987) 2599.

[179] S.A.C. Gould, B. Drake, C.B. Prater, A.L. Weisenhorn, S. Manne, H.G. Hansma, P.K. Hansma, J. Massie, M. Longmire, et al., Journal of Vacuum Science & Technology, A: Vacuum, Surfaces, and Films 8 (1990) 369.

[180] Y. Gan, E.J. Wanless, G.V. Franks, Surface Science 601 (2007) 1064.

[181] B. Drake, R. Hellmann, American Mineralogist 76 (1991) 1773.

[182] F. Ohnesorge, G. Binnig, Science (Washington, DC, United States) 260 (1993) 1451.

[183] G. Meyer, N.M. Amer, Applied Physics Letters 56 (1990) 2100.

[184] B. Drake, C.B. Prater, A.L. Weisenhorn, S.A. Gould, T.R. Albrecht, C.F. Quate, D.S. Cannell, H.G. Hansma, P.K. Hansma, Science (New York, N.Y.) 243 (1989) 1586.

[185] H. Hartman, G. Sposito, A. Yang, S. Manne, S.A.C. Gould, P.K. Hansma, Clays Clay Miner. 38 (1990) 337.

[186] H. Lindgreen, J. Garnaes, F. Besenbacher, E. Laegsgaard, I. Stensgaard, Clay Minerals 27 (1992) 331.

[187] A.L. Weisenhorn, J.E. Mac Dougall, S.A.C. Gould, S.D. Cox, W.S. Wise, J. Massie, P. Maivald, V.B. Elings, G.D. Stucky, P.K. Hansma, Science (Washington, DC, United States) 247 (1990) 1330.

[188] P.A. Johnsson, C.M. Eggleston, M.F. Hochella, American Mineralogist 76 (1991) 1442.

[189] Y. Gan, Surface Science Reports 64 (2009) 99.

[190] F.J. Wicks, K. Kjoller, G.S. Henderson, Canadian Mineralogist 30 (1992) 83.

[191] G.A. Vrdoljak, G.S. Henderson, J.J. Fawcett, F.J. Wicks, American Mineralogist 79 (1994) 107.

[192] K. Kumai, K. Tsuchiya, T. Nakato, Y. Sugahara, K. Kuroda, Clay Sci. 9 (1995) 311.

[193] T.G. Sharp, P.I. Oden, P.R. Buseck, Surf. Sci. 284 (1993) L405.

[194] F.J. Wicks, K. Kjoller, R.K. Eby, F.C. Hawthorne, G.S. Henderson, G.A. Vrdoljak, Can Mineral 31 (1993) 541.

[195] H. Cai, A.C. Hillier, K.R. Franklin, C.C. Nunn, M.D. Ward, Science (Washington, D. C.) 266 (1994) 1551.

[196] R.W.G. Wyckoff, Crystal Structures. John Wiley & Sons, New York, 1968.

[197] C. Ma, R.A. Eggleton, Clays and Clay Minerals 47 (1999) 181.

[198] T.F. Bates, Electron-Opt. Invest. Clays (1971) 109.

[199] M. Amouric, J. Olives, Clays and Clay Minerals 46 (1998) 521.

[200] T. Kogure, A. Inoue, Am. Mineral. 90 (2005) 85.

[201] G.D. Guthrie, Jr., D.R. Veblen, ACS Symposium Series 415 (1989) 75.

[202] J.G. Thompson, R.L. Withers, Clays and Clay Minerals 35 (1987) 237.

[203] M. Amouric, C. Parron, L. Casalini, Electron Microsc. 1994, Proc. Int. Congr. Electron Microsc., 13th 2B (1994) 1285.

[204] K. Yada, K. Iishi, Resumes Commun. - Conf. Int. Phys. Chim. Miner. Amiante, 3rd (1975) 3 9.

[205] K. Yada, Can. Mineral. 17 (1979) 679.

[206] J. Olives, M. Amouric, R. Perbost, Clays and Clay Minerals 48 (2000) 282.

[207] J.H. Anh, D.R. Peacor, Am. Mineral. 72 (1987) 353.

[208] A. Plancon, Clay Miner. 36 (2001) 1.

[209] M. Kosmulski, Journal of Colloid and Interface Science 337 (2009) 439.